Migration of Liquid Drops through Narrow Passages and Flow Dynamics of Cancer Cells through Constricted Microchannels

A thesis submitted
in partial fulfillment of the requirements
for the award of the degree of

Doctor of Philosophy

by

Binita Nath

DEPARTMENT OF MECHANICAL ENGINEERING
INDIAN INSTITUTE OF TECHNOLOGY GUWAHATI
Guwahati - 781039

May 2019

Certificate

It is certified that the work contained in the thesis entitled **"Migration of Liquid Drops through Narrow Passages and Flow Dynamics of Cancer Cells through Constricted Microchannels"**, by Binita Nath (Registration no. 146103024) has been carried out under our supervision and that this work has not been submitted elsewhere for a degree.

(Gautam Biswas)
Professor
Department of Mechanical Engineering
Indian Institute of Technology Guwahati

(Amaresh Dalal)
Asscociate Professor
Department of Mechanical Engineering
Indian Institute of Technology Guwahati

May 2019

Dedicated to the loving memory of my mentor, guide and best-friend.....my 'Babu'.

Acknowledgements

The journey towards accomplishment of this thesis has been wonderful because of the presence of the people around me.

I am grateful to my supervisors, Prof. Gautam Biswas and Dr. Amaresh Dalal for their unwavering faith in me. I shall forever be indebted to them for their constant support and guidance in molding me up as a researcher. They not only guided me to address interesting fluid mechanics problems but also taught me to walk out of the comfort zone and work in an interdisciplinary field of research. In every meeting with Prof. Gautam Biswas, I felt motivated. His positivity and vision influenced me to work harder each and everyday. Dr. Amaresh Dalal's methodical guidance taught me how to develop an inquisitive bent of mind and grow as a researcher. In spite of their busy schedule, both my supervisors gave top priority in helping me out whenever I needed.

I am also very fortunate to work under the guidance of Prof. Siddhartha Sankar Ghosh of Bio-Science and Bio-Engineering Department. Despite my limited knowledge in the field of biological sciences, he always encouraged me. The regular discussions with him helped me in gaining an in-depth knowledge about the research topic.

Besides my advisors, I would like to thank my Doctoral Committee members, namely- Prof. Ujjwal Kumar Saha, Prof. Tapas Kumar Mandal and Dr. Dipankar Narayan Basu, not only for their insightful comments and encouragement, but also for the difficult questions which intrigued me to widen my research work from various perspectives.

The interactions and constructive inputs from Prof. Dipankar Bandyopadhyay, Dr. Pranab Mondal and Dr. Kirti Sahu of IIT Hyderabad further helped me to grow intellectually and develop as an ardent researcher. I feel fortunate enough to have obtained the opportunity to learn the basics of microfluidics from Prof. Suman Chakraborty of IIT Kharagpur and Prof. Sushanta Mitra of University of Waterloo.

The work in cancer cells would not have been possible at all without availing the fabrication facility of IISc Bangalore. I cannot thank enough Prof. Rudra Pratap and Dr. Prosenjit Sen of CeNSe department for giving me the opportunity to work independently in their laboratory and get the channels fabricated. Besides the faculties, I had to interact and work with many students, time and again for this part of my PhD work. I must mention that I really enjoyed working as a team member with my fellow mates, namely- Dhrubajyoti, Asif, Vishal, Anil, Vikas and Neeraj in IIT Guwahati. Also, Rahul from IISc Bangalore had extended his help whenever possible.

I express my sincere gratitude to all the non-teaching staffs of Department of Mechanical Engineering, IIT Guwahati. I would also like to thank the Computer and Communication Center of IIT Guwahati for providing access to PARAM-ISHAN supercomputing facility that undeniably proved invaluable for many of the simulations carried out during the course of this research work.

I have indeed been blessed with a number of good friends who helped me to survive so well through all the highs and lows of PhD years. The time spent with Satarupa, Tamanna, Siddharth, Joydip, Pritam, Mitradip, Surjendu, Nayan Da, Saptak Da, Seim Da and Nilanjan Da of M&A lab will forever be cherished. Snehasish, Harshad, Vinod, Gorthiji, Hiranya and Bhaskrajyoti of Mechanical Department deserve a special mention. Srirupa, Neha, Hirok, Rajib and Upashi of BSBE Department made me feel very comfortable in their lab.

I am thankful to Prof. Anjan Dutta and Mrs. Mousumi Dutta for offering me a 'home away from home' here in IIT Guwahati. The love and support I received from Soumita Madam and Amarabati Madam can never be forgotten. The presence of my JEC friends Firdausa, Needhi, Mayuri, Debolina and Nabanita here in IIT gave me a comfort zone.

Though miles apart, the continuous love and encouragement extended by my close friends Shakira, Debahuti, Sumita, Serolin, Subhasis, Bishal and Iswar truly worked wonders. Besides, the incredible support extended by Vinod HV Sir of Mahindra Engineering, Prof. Rajat Gupta of NIT Mizoram and Prof. R.D Misra of NIT Silchar at different phases of PhD life is really commendable.

It is a matter of coincidence that I got a chance to do PhD here with my husband Manash Pratim Borthakur as my colleague. In fact, it has been a great learning experience for both of us confronting the good and bad phases of PhD journey together.

None of this would have been possible without my family's support and love. My deepest gratitude goes to the tireless efforts put in by my mother, my elder sister for her indisputable confidence in me and my brother for the little bundle of joy he is. Both my mother-in-law and sister-in-law have been extremely kind and considerate.

And lastly, I would like to say about the person for whom I could reach here. Like every guardian, my Father too saw a dream for me. Right from childhood, he wanted me to follow his trait and be a Doctorate in Mechanical Engineering, as he himself could not be. Right from introducing me to the huge machines of Mechanical workshop (REC Silchar) when I was a kid to showing me what a journal paper is, when I was a B.E student, he did that all continuously. Gradually his 'big dream' turned out to be my 'aim' in life. His constant support and motivation have always been the guiding force that helped me to secure a seat here after leaving jobs and preparing earnestly for entrances. I am grateful to get a Dad, who not only taught me to see the world through his eyes but also to learn the skill of targeting towards a goal with utmost dedication. Whatever I am today, is all because of him.

Binita Nath

Abstract

The aims of the present dissertation is to understand the flow dynamics of deformable drops as well as cancer cells in microchannels. In this regard, we study the motion and deformation of a neutrally buoyant drop in a microchannel both in the absence and presence of electric fields, tuning the various hydrodynamic and electrical properties in the first part of the thesis. The problems in the first part have been extensively investigated using numerical analysis. In the other part, we extend our understanding of motion of deformable drops in microchannels to investigate the flow behaviour of cancer cells through constricted microchannels. Different biological assays are performed to analyze the metastatic potency of the cells after passing through the constriction. The study on this latter part opens up a horizon for further investigations; this class of flows is becoming increasingly relevant with advances in medical engineering and nanofluidics.

The prime focus of the first problem of interest is to investigate the migration and break up of a neutrally buoyant droplet in a tube containing another immiscible liquid in the creeping flow. The interface between the two immiscible fluids has been captured using a coupled level-set and volume-of-fluid (CLSVOF) approach. The deformation and breakup dynamics of the droplet have been investigated in terms of three dimensionless parameters, namely, the ratio between the radius of the undeformed droplet and the radius of the capillary tube, the viscosity ratio between the dispersed and the continuous phases, and the capillary number that measures the relative importance of the viscous force over the surface tension force. A thorough computational study has been conducted to find the critical capillary number for a range of droplets of varied sizes suspended in flows having different viscosity ratios.

Next, the cross-stream migration phenomenon exhibited by a two-dimensional drop is studied. The multiphase modeling is done adopting the volume-of-fluid(VOF) interface capturing method. In the absence of electric field the important non-dimensional parameters pertaining to such two-phase flows are viscosity ratio between the drop fluid and the surrounding medium, the ratio of drop diameter to channel height and the capillary number. The influence of all these parameters in drop migration has been studied by varying the parameters in a wide range along with varied initial off-center positions. The presence of electric field introduces additional stresses at the drop interface and its effect on drop migration has been

investigated by solving the electro-hydrodynamic Navier-Stokes equations. Extensive computations have been performed to analyze the combined effect of electric field and shear flow in the cross stream migration of the drop. The results obtained for perfect dielectric fluids indicate that the droplet migration enhances in the presence of electric field. The permittivity ratio and the electric field strength play a major role in drop migration and deformation. Computations using the leaky dielectric model also show that for certain combination of electrical properties, the drop undergoes immense elongation along the direction of electric field. The conductivity ratio is a vital parameter in such system of fluids. It has been observed that the leaky dielectric drops (subjected to certain set of conditions) along with translation also exhibit rotational behavior.

Next, the dynamics of a droplet in shear flow under the influence of an external electric field has been investigated by performing extensive numerical simulations. The study has been again carried out by solving two-dimensional electrohydrodynamic equations and the interface has been captured using a VOF approach. For the case of dielectric fluids, the deformation of the drops can be either enhanced or reduced by varying the permittivity ratio and electric field strength. The nature of the polarization forces acting at the interface can be either compressive or tensile depending on the magnitude of the permittivity ratio. The local electric field intensity inside the drop is significantly altered by varying the permittivity contrast between the fluids. The computations for leaky dielectric fluids reveal that the deformation of the drop can be effectively tuned by altering the permittivity as well as the conductivity ratios. The electric forces acting at the interface are critically dependent on the relative contrast between the electric properties of both the phases. The conductivity ratio decides the magnitude and nature of charge at the upper and lower portions of the droplet interface thereby fundamentally maneuvering the droplet dynamics under the applied electric field.

Finally, to understand the burgeoning challenges of metastasis, a 3 mm long microchannel constricted to 7 μm width is designed and fabricated to mimic *in-vivo* capillaries of a human body. The motion of single or aggregated malignant HeLa cells (size 17 - 30 μm) have been observed microscopically through the constricted microchannel at a constant flow rate of 30 μl/h. Quantitative deconvolution of high-speed videographs of a single cell of 30 μm reveals cellular deformation while passing through constriction, having elongation index, average transit velocity and entry time of 2.67, 18 mm/s and 5.1 ms, respectively. Morphological analysis of live and apoptotic cells by dual staining with Acridine Orange/Ethidium Bromide demonstrated retention of a significant viable cell population after exit through the constriction and a viability index of 50% is quantified by dye exclusion assay. The cumulative data for microfluidic parameters, morphology and relevant metastatic MMP2 gene expression efficiency measured by real-time polymerase chain reaction reveal retention of virulence potency that could possibly cause metastasis. These findings related to motion and viability of HeLa cells would be beneficial in developing futuristic MEMS device for cancer theranostics.

Contents

List of Figures

List of Tables

Nomenclature

English Symbols

a	Aspect ratio of the drop in the capillary tube
a^*	Aspect ratio of the drop in the channel
Ca	Capillary number
Ca_{cr}	Critical capillary number
Ca_E	Electric capillary number
d	Shortest distance of the interface from any point
d	Original diameter of the cell
$\mathbf{D}$	Electric displacement vector
$\mathbf{D}_v$	Rate of deformation tensor
E	Magnitude of electric field
$\mathbf{e}$	Electrostatic force
$\mathbf{g}$	Acceleration due to gravity
H_δ	Heaviside function
H	Width of the channel
i, j	Cell numbers in x and y direction, respectively
l	Maximum length of the cell in the microchannel
L	Computational domain length
L_i	Total interfacial length of the deformed drop
L_{max}	Maximum length of the drop in the channel
L_{min}	Minimum width of the drop in the channel
D_i	Deformation index of the drop
$\mathbf{M}$	Maxwell's stress tensor
$\mathbf{n}$	Normal vector
N_z	Number of grids in the z of the computational domain
N_r	Number of grids in the r of the computational domain
p	Pressure
q_v	Volume density of free charges
r^*	Ratio of the initial droplet diameter to the height of the channel
R	Conductivity ratio
Re	Reynolds number
Re_E	Electrical Reynolds number
S	Permittivity ratio
t	Time
t_E	Electric time scale
t_f	Flow time scale

u	X-direction velocity component
U_w	Imposed velocity at the walls
v	Y-direction velocity component
V_d	Drop Velocity
x, y	Cartesian coordinates
y_c	Lateral position of the droplet in the channel

Greek Symbols

α	Void fraction
γ	Surface tension coefficient
σ	Electrical conductivity
ϵ	Absolute permittivity
ϵ_o	Permittivity of free space
ϵ_r	Dielectric constant
κ	Mean curvature of the interface
μ	Dynamic viscosity
ϕ	Level set function
ψ	Electric potential
ρ	Density of medium
λ	Viscosity ratio
η	Density ratio

Acronyms

AO	Acridine Orange
AMR	Adaptive Mesh Refinement
BI-CGSTAB	Biconjugate Gradient Stabilised Method
BIM	Boundary-Integral Method
cDNA	complementary DNA
CFL	Courant-Friedrichs-Lewy
CLSVOF	Combined Level Set and Volume of Fluid
CSF	Continuum Surface Force
CTC	Circulating Tumor Cell
DMEM	Dulbecco's Modified Eagle's Medium

DNA	Deoxyribonucleic Acid
ECM	Extracellular Matrix
EHD	Electrohydrodynamics
ENO	Essentially Non-Oscillatory
EtBr	Ethidium Bromide
FESEM	Field Emission Scanning Electron Microscopy
GAPDH	Glyceraldehyde 3-Phosphate Dehydrogenase
LVIRA	Least square Volume of fluid Interface Reconstruction Algorithm
MAC	Marker and Cell
MEMS	Micro-Electro-Mechanical Systems
MMP	Matrix Metalloproteinase
NOA	Norland Adhesive 81
NCCS	National Centre for Cell Science
PCR	Polymerase Chain Reaction
PDMS	Poly-dimethylsiloxane
PLIC	Piecewise Linear Interface Calculation
PMMA	Poly-methylmethacrylate
PROST	Parabolic Reconstruction of Surface Tension
qPCR	Quantitative real-time PCR
QUICK	Quadratic Upstream Interpolation for Convective Kinetics
RNA	Ribonucleic Acid
SLIC	Simple Line Interface Calculation
VOF	Volume Of Fluid

Subscripts

l	Liquid
g	Gas
s	Suspending medium
d	Drop medium

Superscripts

$n, n+1$	time levels

Chapter 1

Introduction

Microfluidics is an interesting and evolving area of science. Microfluidics has been widely recognized for its high potential in various biochemical, clinical and industrial applications [9]. Interfacial morphologies of multi component fluid flows in microfluidic devices have been studied extensively in recent times because of their diverse applications and in that, the motion of deformable drops in two-dimensional channels or in circular tubes is of great interest owing to its applications in the arena of bio-analysis [10], multiphase extraction [11], emulsification [12], Micro-Electro-Mechanical Systems (MEMS) devices [13], and microreactors [14]. Additionally, for some microfluidics related applications, the study of drop dynamics in confined shear flows is relevant. In such confined channels, the wall effects act to stabilize elongated drop shapes and this feature stands very relevant for the production of elongated micro-structures utilized in several industrial applications, such as food processing, where the particle shape can be frozen by gelation [15]. Much of the early interest in manipulating droplets in microchannels was motivated by the well suggested analogy between the droplet motion and the motion of blood cells in capillary tubes. Of late, many investigations have been conducted on motion and deformation of cancer cells through narrow passages, mimicking microcapillaries in human body. Microfluidic devices are considered superior to their macroscopic analogues primarily because of the availability of higher surface-to-volume ratio, smaller throughput leading to easier control of the operating parameters, and reduction in operating cost in the processes where costly chemicals are deployed [16].

1.1 Drop deformation and migration in channels or tubes

The interest in manipulating droplets in micro channels has emerged from a few distinct motivations. Microfluidic system having micro channels can be utilised to control networks of chemical reactions at the millisecond scale [17]. In such systems, the reagents are mixed in droplets that flow along a microchannel. The chemical kinetics related measurements become easy with the knowledge of the droplet velocity and calculation of reaction time inside the droplet, that grows linearly with the length of channel. However all these advantages come at the price of raising a few complex situations that appear due to the deformable interface of the droplets. The interfacial tension and its variations, the complexity brought about by the singular events like merging or splitting of drops and many other crucial phenomena have to be well captured and accounted. In physical words, the motion of the drops introduce nonlinear laws into the otherwise linear Stokes flows [18].

The theoretical development of the study on drop dynamics in microchannels depends on various parameters that are responsible for bringing topological changes on the interface. Some of the dictating parameters are the buoyancy and the surface tension. Buoyancy acts as a destabilizing force at the interface and is directly proportional to acceleration due to gravity, as it is a force that opposes the weight of an immersed object. The condition in which the averaged density of the physical body is equal to the density of the fluid in which it is immersed is termed as neutral buoyancy. An object having neutral buoyancy will neither rise nor sink. Surface tension effect balances the pressure difference acting on the interface and acts as a stabilizing force [19].

The interfacial tension and viscosity compete with each other, as both these properties tend to govern the motions at such small scales. The relative strength of the two is expressed by the capillary number Ca. Low values of Ca indicates that the stresses due to interfacial tension are stronger than the viscous stresses. Under such a condition the flowing drops tend to minimize their surface area by producing spherical ends [18]. In the reverse situation, when Ca is higher, it is the viscous effects that dominate and large deformations of the drops as well as asymmetric shapes are observed.

1.2 The paradigm of flows involving electrohydrodynamics

The denomination 'electrohydrodynamics' (EHD) refers to the studies involving hydrodynamics coupled with electrostatics. In the context of interfacial flows, EHD describes the motion of liquids separated by an interface subjected to an electric field. In the presence of an electric field, the behavior of the fluid medium changes, which depends on the electrical properties, like electrical permittivity and conductivity of the fluids [20, 21]. The molecules of the fluid medium gets polarized under the influence of the electric field. The charges that appear due to the polarization phenomenon are termed as bound charges. In addition, free ions/charge carriers may be present in the fluid which migrate under the influence of the applied electric field. A perfect dielectric is a fluid without any ions or free-electrons, thereby leading to only polarization effects being present. Many apolar liquids, such as benzene, are considered to be perfect dielectric fluids [22]. However, most liquids are known for their ability to dissolve impurities, which makes them slightly conducting in nature. On the other hand, perfect conductors are those where the conductivity is high enough to consider the ohmic conduction of the free ions as the only agent causing charge transport. The application of the external electric field results in a force being generated on the bound as well the free charges, which effectively alters the hydrodynamics of the flow. This has been realized as an effective tool in controlling the flow characteristics in myriad applications, such as EHD inkjet printing, spraying and atomisation, breakup of bubbles and drops, among others [21, 23, 24].

1.3 Drop deformation and migration in the presence of an electric field

With the addition of an external force supplied by any energy field, be it electric, magnetic, gravitational, thermal, or acoustic, the morphology of droplet deformation and migration is significantly affected if the force is strong enough. With the enormous growth of applications involving microliter and nanoliter sized liquid droplet emulsions, the application of electric field to microfluidic devices has infact become a topic of great interest to the scientific community [25]. Electric field provides

additional control on the flow physics of the droplets in microchannels. Researchers have found that it is worth studying the affects of electric field as it does have a crucial impact on the drop dynamics [26–29]. One of the unique aspects of using an electric field to manipulate droplets is that these methods are physically unobtrusive to the flow field. The electric field need not be in physical contact with a liquid droplet in order to change its direction or shape [30]. Another remarkable benefit of using an electric field is the availability of low cost electrical control devices. With the recent advances in technology microfluidic devices with imprinted electrodes are available [31]. Drop deformation and migration in the presence of electric field are becoming increasingly relevant with advances in medical engineering and nanofluidics [32, 33].

1.4 Introduction to cancer biology

The term cancer refers to a malignant growth or tumor resulting from an uncontrolled division of cells. In human body normal cells undergo controlled growth whereas the cancer cells grow in an uncontrolled way. These cancer cells invade the nearby parts of the body and spread to other organs, which is known as metastasis. Metastasis is the spread of cancer from one organ or part of the body to another without being directly connected with it. Metastasis is a Greek word meaning "displacement", from meta, "next", and statis, "placement".

The transformation of normal cells to cancer cells is a gradual process caused due to mutation in genes. Deoxyribonucleic acid (DNA) carries genes which contains information for protein production in the body. Some of these proteins support cells to divide and grow whereas, other proteins suppresses growth. Mutations caused by tobacco smoke, radiation, ultraviolet radiation, and other carcinogens result in the abnormal production of these proteins. When these proteins are produced in more or less than the normal quantity, the cell deviates from the its normal metabolism and forms cancer cell [34]. Normal cells grow in a controlled way such that every time a cell divides, the end of its chromosomes become shorter. After the chromosomes worn down, the cell dies and is replaced by a new cell. But in cancer cells the chromosomes retain their length by continuously adding bits back on it. That is why cancer cells grow in unrestrained fashion to form tumor [35]. Body mechanism has many checkpoints which ensures that the cells formed are near perfect replica of the

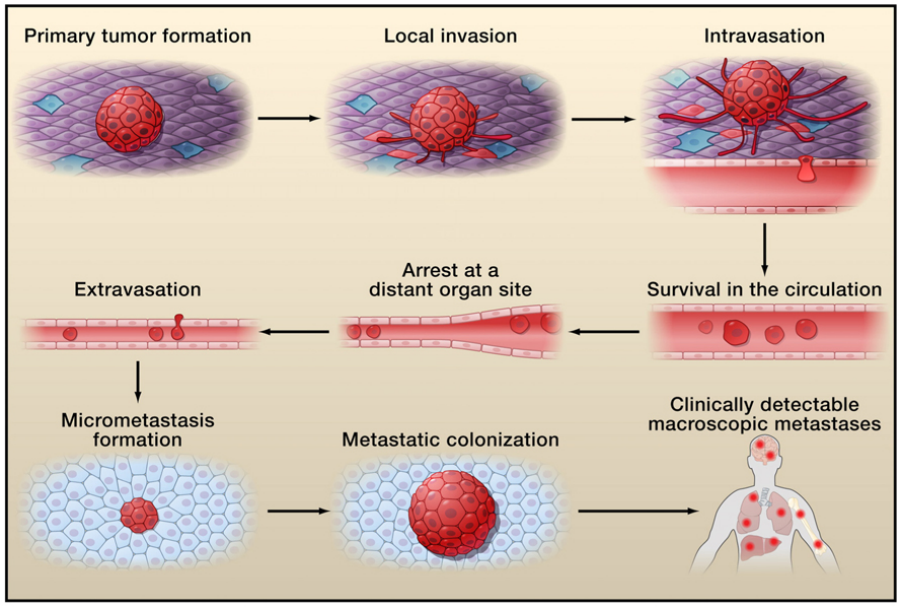

Figure 1.1: Schematic representation of the motion of cancer cells to seed distant metastasis [1].

parent cells and Elledge [36] pointed out that cancer cells bypass many checkpoints to become cancerous. However, the transformation of normal cell to cancerous cell is a very rare and difficult process and in human body, roughly 3 billion normal cells divide everyday. Accidents in the reproduction of the cells caused by heredity or carcinogens during any of those divisions can create a cell that follow further mutations and develop into a cancer cell. The main reason for most of the cancer deaths are not the primary tumors but the secondary tumors that are formed due to spreading of the original tumor to adjacent or non-adjacent organs. During the growth of cancer, some cancer cells attain the ability to penetrate the walls of blood or lymphatic vessels, after which they can circulate through the bloodstream to other sites and tissues in the body. A typical cancerous tumor contains millions of cells. As the cells proliferate, they do not all stay in the neighborhood. Some cells leave the edges of the tumor and are swept away by the bloodstream. These are called circulating tumor cells (CTCs) which can remain loose in circulation, group together as they travel, or penetrate themselves into new tissues. CTCs contain information about a tumor, information that researchers think might be key to cancer treatment. Once the tumor cells come to rest at another location, they re-penetrate the walls of vessels

and continue to proliferate, eventually forming another clinically detectable tumor. Metastasis is one of the hallmarks of the malignancy of cancer [37–39]. While entering (intravasation) and exiting (extravasation) the vascular vessel, cancer cells have to migrate through the extracellular matrix (ECM) and the basement membranes of the vessel walls. The stiffness and geometric limitation of the cellular barriers bring many challenges to the cancer cells, which require them to withstand severe deformations during the transmigration process. In the process of metastasis, the cancer cells sometimes need to extensively deform and flow through microcapillaries (5 to 10 μm) of sizes much smaller compared to their own. Figure 1.1 [1] shows in detail the process of invasion of cancer cells into the circulatory system through the basement membrane from a primary tumor and its circulation [40–44] in the capillaries to seed metastasis at a distant site.

1.5 Objectives

From a detailed literature survey, it is learnt that a neutrally buoyant drop in a fully-developed channel flow is capable of crossing streamlines as a consequence of drop deformation and formation of a variety of transient non-spherical shapes, in contrast to non-deformable drops and particles. The complex mechanism of droplet break up and merging of daughter droplets enriches this area of research. Furthermore, the dynamics of migration and deformation of a drop during the course of its travel from an initial off center position needs deeper understanding. For the drops placed in a confined channel and subjected to shear, the wall effects act to stabilize elongated shapes and this leads the drop to take several interesting shapes which need to be investigated. The presence of an electric field further modifies the interfacial stresses and hence a marked influence on the drop dynamics is discerned. On the other hand, even in this modern era of cancer therapeutics, scientists and oncologists have not been able to resolve all the mysteries of metastatic cancer, which causes high mortality worldwide. The motion of cancer cells through micro-capillaries of diameter much smaller then their own size is intriguing.

In view of the above context, the objectives of the present investigation have been formulated as follows:

1. **Migration of a droplet in a cylindrical tube in the creeping flow regime :** The deformation and breakup dynamics of the droplet are investi-

gated in terms of three dimensionless parameters, namely, the ratio between the radius of the undeformed droplet and the radius of the capillary tube, the viscosity ratio between the dispersed and the continuous phases, and the capillary number that measures the relative importance of the viscous over the surface tension force.

2. **Cross stream migration of drops suspended in Poiseuille flow in the presence of an electric field :** The presence of electric field introduces additional interfacial stresses at the drop interface and extensive compuations are performed to analyse the combined effect of electric field and shear flow in the cross stream migration of the drop.

3. **Influence of electric field in the deformation of a drop in shear flow:** The shear is produced by moving the parallel walls of the channel at equal speeds but in reverse directions and electric field is induced in the system by employing a constant voltage difference across the channel width. The deformation and orientation of a stationary drop are studied inside the microchannel.

4. **Understanding flow dynamics, viability and metastatic potency of cervical cancer (HeLa) cells through constricted channel:** Under experimental conditions, the cells have to deform in order to pass through the constricted channel, allowing quantification of several physical parameters such as entry time, transit velocity and elongation index together with many other biological parameters.

1.6 Layout of the report

A part of the thesis focuses on the phenomena of deformation and migration of drops in a microchannel, both in the absence and presence of an external electric field. In the other part, the flow of cancer cells through microchannels was investigated taking HeLa cells as model to study the metastasis. The thesis is divided into a few chapters to approach towards the solution of the complex problems in a systematic and methodical way.

- Chapter 1 provides a preliminary introduction to the problems. It includes

justification for the research and background information on the motivation behind the study.

- Chapter 2 highlights the numerical methodology adopted for interface tracking and provides a stepwise solution procedure of the governing equations involved in the flow physics of droplet dynamics in microchannels .
- Chapter 3 emphasises on the procedure adopted for the experimental work with cancer cells.
- Chapter 4 demonstrates an extensive study of the migration of a droplet in a cylindrical tube in the creeping flow regime.
- Chapter 5 documents a detailed study of the cross stream migration of a droplet in a microchannel subjected to Poiseuille flow and also an external electric field.
- Chapter 6 describes a thorough study of a shear deformed drop in a microchannel in the presence of electric field.
- Chapter 7 covers an experimental study of flow dynamics of HeLa cells in microchannels.
- Chapter 8 discusses the conclusions and highlights the scope for future work.

Chapter 2

Numerical Modelling of Two Phase Flows

2.1 Introduction

The numerical modeling of two-phase flows has become a popular choice in recent decades, owing to their ability to provide deep insight into the physical mechanisms associated with such flows. A variety of methods have been developed to simulate the transient nature of the interface separating the two fluids. The numerical methods can be broadly divided into two groups, viz., Eulerian and Lagrangian methods. In the Eulerian approach, the interface is embedded in the computational cells of the discretized domain. The location of the interface is identified using a scalar function. The grid remains stationary during the simulation and the cells containing both the fluids are termed as 'two-phase' cells. In contrast to the Eulerian approach, the Lagrangian method treats the interface as a sharp boundary. At every timestep, a grid conformal with the evolving interface is generated to solve the governing equations pertaining to the flow. Additionally, hybrid Lagrangian-Eulerian methods are available, wherein the nodes of the mesh can be moved in Lagrangian fashion, or can be held fixed in Eulerian manner.

In the present thesis, the Eulerian approach has been adopted for solving a variety of two-fluid flow problems. An inhouse solver developed using coupled level-set and volume-of-fluid (CLSVOF) method is employed for simulating the dynamics of drops in a capillary tube in chapter 4. Subsequently, an open source solver *Gerris*,

which is based on the volume-of-fluid methodology, has been adopted for simulating the cross stream migration phenomenon and effect of shear in the deformation of drop presented in chapters 5 and 6, respectively.

2.2 CLSVOF method

The volume-of-fluid method, first suggested by Hirt and Nichols [45], has been extensively used for computations involving two fluids separated by a interface. It employs an Eulerian approach, wherein the interface is approximated within each cell through which it passes. The initial method for representing the interface was known as 'simple line interface calculation'(SLIC), where the interface was identified by piecewise-constant line segments in each cell containing the interface. Subsequently, the interface representation was significantly improved by the piecewise-linear interface calculation (PLIC) of Youngs [46] and the least square volume interface reconstruction (LVIRA) method of Puckett *et al.* [47]. The VOF method satisfies the compliance of mass conservation extremely well. However, due to the inherent discontinuity of the VOF function across the interface, accurate computation of the geometric properties remains a challenging task. An efficient interface capturing method, known as the level-set method was introduced by Osher and Sethian [48]. The level set method allows accurate computation of the geometric properties of the interface. However, the violation of mass conservation may occur if the level set method is improperly implemented. The CLSVOF method combines the benefits of both the volume-of-fluid and the level set method. In the CLSVOF method of Sussman and Puckett [49], the level set function is used only to compute the geometric properties at the interface while the void fraction is advected using the VOF approach. A few variants of the CLSVOF method are available in literature [50,51]. In the present thesis, the CLSVOF method has been used for solving a variety of interfacial flow problems. The methodology implemented is described in detail in the forthcoming subsections.

2.2.1 Governing equations

The governing equations for mass and momentum conservation for the incompressible Newtonian two fluid system can be expressed by a single fluid continuum as

follows:

$$\nabla \cdot \mathbf{v} = 0, \tag{2.1}$$

$$\rho \left[\frac{\partial \mathbf{v}}{\partial t} + (\mathbf{v} \cdot \nabla)\mathbf{v} \right] = -\nabla p + \nabla \cdot [\mu(\nabla \mathbf{v} + \nabla \mathbf{v}^{\mathbf{T}})] + \rho \mathbf{g} + \mathbf{f_{sv}}. \tag{2.2}$$

where $\mathbf{v} = (u, v)$ is the velocity field, t is the time, p is the pressure, $\mathbf{g}$ is the gravitational acceleration, ρ and μ are the density and viscosity respectively, and $\mathbf{f_{sv}}$ is the surface tension force. The surface tension term $\mathbf{f_{sv}}$ is defined by the continuum surface model of Brackbill *et al.* [52] and is detailed in Section 2.2.8. The marker-and-cell algorithm (MAC) is employed to solve the single set of governing equations on a staggered grid arrangement of Harlow and Welch [53]. A uniform grid is used where the grid size in both the directions is considered to be the same, i.e. $\Delta x = \Delta y$. The scalar variables are defined at the cell centers and the vector quantities are located at the center of the cell faces.

2.2.2 Indicator functions

The indicator function identifies the fluid, i.e. liquid or gas inside the computational domain. For the VOF method, the scalar function α, denoted as the void fraction, is used to locate the fluid interface. The value of α is assigned as,

$$\alpha = \begin{cases} 1 & \text{if it is a liquid cell,} \\ 0 & \text{if it is a gaseous cell,} \\ 0 < \alpha < 1 & \text{if it is a two-phase cell,} \end{cases} \tag{2.3}$$

where, liquid and gas are the two immiscible fluids separated by a sharp interface. 'Gas' represent the dispersed phase (fluid inside the drop) and 'liquid' represents the suspending medium (fluid surrounding the drop in the channel.)

In the level set method, the fluid type is identified based on the sign of the level set function. Hence, the level set function, ϕ, is defined as the signed distance from the interface,

$$\phi(\mathbf{r}, t) = \begin{cases} +d & \text{in the liquid region,} \\ 0 & \text{at the interface,} \\ -d & \text{in the gas region} \end{cases} \tag{2.4}$$

where $d = d\,(t)$ is the shortest distance of the interface from point $\mathbf{r}$. Figure 2.1 shows the typical distribution of void fraction and level set function around the interface.

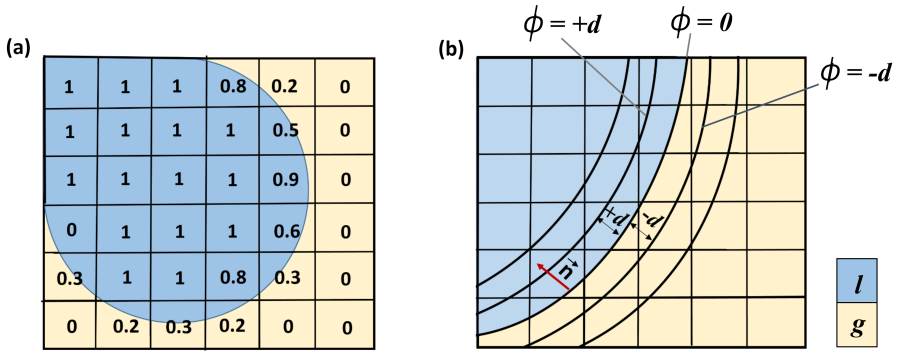

Figure 2.1: Typical distribution of (a) void fraction and (b) level set function around the interface.

2.2.3 Volume-of-fluid advection

The void fraction, α, defined in each computational cell, is advected with the fluid velocity using the advection equation,

$$\frac{\partial \alpha}{\partial t} + \mathbf{v} \cdot \nabla \alpha = 0. \tag{2.5}$$

Using the continuity equation (Eq. 2.1), it can be written as

$$\frac{\partial \alpha}{\partial t} + \nabla \cdot (\mathbf{v}\alpha) = 0. \tag{2.6}$$

By using finite difference scheme, Eq. 2.6 can be discretised as

$$\alpha_{i,j}^{n+1} = \alpha_{i,j}^{n} + \frac{\Delta t}{\Delta x}(\delta V_{i-1/2,j} - \delta V_{i+1/2,j}) + \frac{\Delta t}{\Delta y}(\delta V_{i,j-1/2} - \delta V_{i,j+1/2}), \tag{2.7}$$

where $\delta V_{i+1/2,j} = (u\alpha)_{i+1/2,j}$ is the amount of liquid volume fraction fluxed through the right cell face. The superscripts n and $(n+1)$ denote the values at the current and next time step and $\Delta t, \Delta x$ and Δy are the time step and grid spacing in x- and y-direction, respectively. Equation 2.7 is solved by applying operator split approach resulting in two equations:

$$\alpha_{i,j}^{*} = \alpha_{i,j}^{n} + \frac{\Delta t}{\Delta x}(\delta V_{i-1/2,j} - \delta V_{i+1/2,j}) + \frac{\Delta t}{\Delta x}\alpha_{i,j}^{*}(u_{i+1/2,j} - u_{i-1/2,j}), \tag{2.8}$$

$$\alpha_{i,j}^{n+1} = \alpha_{i,j}^{*} + \frac{\Delta t}{\Delta y}(\delta V_{i,j-1/2}^{*} - \delta V_{i,j+1/2}^{*}) + \frac{\Delta t}{\Delta y}\alpha_{i,j}^{*}(v_{i,j+1/2} - u_{i,j-1/2}). \tag{2.9}$$

The star (*) terms represent the intermediate values after sweep in first direction. The modified equation, $\partial\alpha/\partial t + \mathbf{v}\nabla\cdot\alpha = \alpha\nabla\cdot\mathbf{v}$, is solved instead of Eq. 2.6 by adding "divergence correction" terms on the right-hand side of Eqs. 2.8 and 2.9, resulting in higher accuracy.

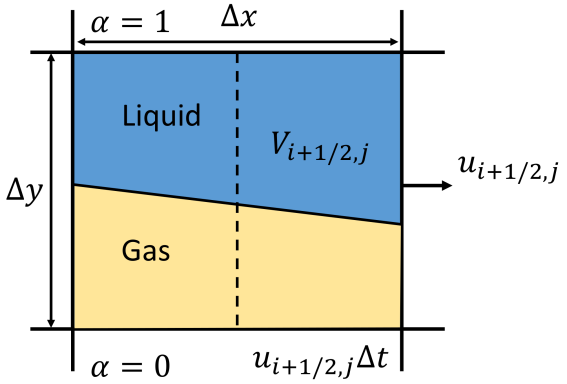

Figure 2.2: Physical domain with a single two-phase cell.

The volume flux δV, in the discretized form, can be obtained using a geometrically based calculation as shown in Fig. 2.2. Hence, the solution of the advection equation conserves the void fraction exactly, i.e. no numerical diffusion is introduced. Considering the right face of the two phase cell, a portion $(u_{i+1/2,j}\Delta t\ \Delta y)$ can be calculated whose fluids will be fluxed into the neighboring cell, supposing $(u_{i+1/2,j}\Delta t\ \Delta y)$ is positive. Knowing the interface position and the velocity, the fluxed volume from this face to the neighboring cell can be calculated as,

$$\delta V_{i+1/2,j} = \frac{u_{i+1/2,j}V_{i+1/2,j}}{u_{i+1/2,j}\Delta t\Delta y} = \frac{V_{i+1/2,j}}{\Delta t\Delta y} \tag{2.10}$$

Equation 2.8 can be solved after calculating δV from Eq. 2.10 and the interface is reconstructed based on $\alpha^*_{i,j}$. The vertical fluxes are then determined using a geometric calculation analogous to the horizontal fluxes and the updated volume fractions $\alpha^{n+1}_{i,j}$ are finally obtained from Eq. 2.9. To obtain second order accuracy, the sweep directions are swapped at each time step and the first sweep is differenced implicitly whereas the second sweep is differenced explicitly [54].

2.2.4 Level set advection

In the CLSVOF method, the advection equation for level set function is solved in addition to the void fraction advection (Eq. 2.6). Using the initially known position

of the interface, the advection of the level set function is given by,

$$\frac{\partial \phi}{\partial t} + \mathbf{v} \cdot \nabla \phi = 0. \tag{2.11}$$

The convective term of Eq. 2.11 is discretized using the essentially non-oscillatory (ENO) scheme [55]. The level set function is reinitialized to the exact signed normal distance after each time step. The reinitialization of the level set function is done from the reconstructed interface by coupling level set function with the void fraction.

2.2.5 Interface reconstruction

The interface separating the fluids, in the Eulerian approach, passes through the grid cells of the computational domain. The geometrical approximation of the interface can be based on either piecewise constant segments, piecewise linear segments or parabolic fit, as in 'parabolic reconstruction of surface tension' (PROST) [56]. The commonly employed interface reconstruction algorithms are (i) least-squares volume-of-fluid interface reconstruction algorithm (LVIRA) and (ii) coupled level-set and volume-of-fluid approach (CLSVOF). In both the aforesaid methodologies, the interface is represented by piecewise linear segments. The position of the interface is uniquely defined by the interface normal vector $\hat{\mathbf{n}}$ and the offset distance l from the cell center in each two phase cell, as shown in Fig. 2.3. The aim of the reconstruction algorithm is to determine $\hat{\mathbf{n}}_{i,j}$ and $l_{i,j}$ for each two-phase cell (i, j) such that the approximation of the interface reproduces the updated void fraction $\alpha_{i,j}$ in each cell exactly. The algorithms to construct the interface by computing $\hat{\mathbf{n}}_{i,j}$ and $l_{i,j}$ are discussed below.

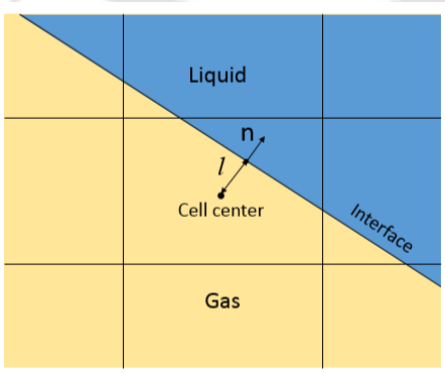

Figure 2.3: Interface normal n and length l.

2.2.5.1 LVIRA interface reconstruction

The 'least- squares volume-of-fluid interface reconstruction algorithm' is used for constructing an approximation to the interface at each time cycle, given the values of void fraction. This algorithm generates a linear approximation of the interface which are also continuous across the cell boundaries, in each two-phase cell. The approximate interface is determined by minimization of the following function in the 3×3 block of cells centered on the (i, j) cell,

$$G_{i,j}(\mathbf{n}_{i,j}) = \sum_{k,l=-1}^{1} \left[\alpha_{i+k,j+l} - \hat{\alpha}_{i+k,j+l}(\mathbf{n}_{i,j})\right]^2, \tag{2.12}$$

subject to the constraint that the void fraction is exactly reproduced at the center cell of the 3×3 block, i.e. $\hat{\alpha}_{i,j} = \alpha_{i,j}$. Here, $\alpha_{i,j}$ is the actual void fraction of the cell (i, j) and $\hat{\alpha}_{i,j}$ is the approximation due to the linear interface constructed through the block based on $\mathbf{n}_{i,j}$ and $l_{i,j}$. The function $G_{i,j}$ is the squared deviation of the actual void fraction from the void fraction given by the mapping using the same line for the entire 3×3 block centered at (i, j). The minimization of the function (Eq. 2.12) rotates and translates the line in such a way to ensure that the mapping is exact for the center cell. The straight line associated with this mapping is the best fit to the void fraction field for the neighboring cells. The aforementioned optimization algorithm requires an initial estimate of $\mathbf{n}$, which can be obtained from the Youngs' method as $\mathbf{n} = \frac{\nabla\alpha}{|\nabla\alpha|}$. The LVIRA algorithm is a second order method and reproduces linear interfaces exactly.

2.2.5.2 CLSVOF interface reconstruction

In the CLSVOF algorithm, the normal $\mathbf{n}_{i,j}$ at the interface is computed from the level set function. Due to the smoothness of level set function across the interface, the normal vector $\mathbf{n}_{i,j}$ can be simply obtained by taking the gradient of the level set function as given by,

$$\mathbf{n} = \frac{\nabla\phi}{|\nabla\phi|}. \tag{2.13}$$

Once the interface normal is calculated, the value of $l_{i,j}$ is obtained by means of a standard root-finding method (like secant method) such that the approximation of the interface reproduces the updated void fraction $\alpha_{i,j}$ in each cell exactly.

2.2.6 Smoothening technique

The distribution of the void fraction is discontinuous and physical properties undergo sharp jump across the interface. This may lead to unwanted numerical diffusion in normal finite difference schemes. To alleviate these problems, the interface is given a fixed thickness that is proportional to the spatial mesh size. The smoothness of the level set function allows in defining a smoothed void fraction field using a Heaviside function $H(\phi)$ as,

$$\tilde{\alpha} = H(\phi) = \begin{cases} 0 & \text{if } \phi < -\epsilon, \\ \frac{1}{2} + \frac{\phi}{2\epsilon} + \frac{1}{2\pi}\left[\sin\left(\frac{\pi\phi}{\epsilon}\right)\right] & \text{if } |\phi| \leq \epsilon, \\ 1 & \text{if } \phi > \epsilon, \end{cases} \tag{2.14}$$

where, the thickness of the interface is taken as 2ϵ which generally varies from $2\epsilon = 3\Delta r$ to $7\Delta r$, Δr is the size of the computational cell. The normal vector can be calculated following Sussman *et al.* [56] as,

$$\mathbf{n} = \nabla H(\phi). \tag{2.15}$$

The curvature κ is then given by,

$$\kappa = -\nabla \cdot \mathbf{n}. \tag{2.16}$$

In order to allow the fluid properties to change smoothly from the value on one side of the interface to the value on the other side, the smoothed void fraction field is used for calculation of density and void fraction as

$$\rho\left(\tilde{\alpha}\right) = \rho_l \tilde{\alpha} + \rho_g\left(1 - \tilde{\alpha}\right), \tag{2.17}$$

$$\mu\left(\tilde{\alpha}\right) = \mu_l \tilde{\alpha} + \mu_g\left(1 - \tilde{\alpha}\right), \tag{2.18}$$

where, the subscripts l and g denote the properties of liquid and gas, respectively.

2.2.7 CLSVOF advection algorithm

The algorithm for the interface advection in the CLSVOF method is described below.

1. The intermediate void fraction $\alpha^*_{i,j}$ is calculated by solving the Eq. (2.8) in the first sweep direction (say x-direction).

2. After $\alpha^*_{i,j}$ is obtained, ϕ is advected in the same sweeping direction by solving the split form of Eq. (2.11). Hence, for the x-direction sweep, the equation is,

$$\frac{\partial \phi}{\partial t} + u\frac{\partial \phi}{\partial x} = 0. \tag{2.19}$$

The discretisation of the convective term in Eq. (2.19) is done by employing a second order ENO scheme [55, 57].

3. The interface normal can be easily calculating by using a central differencing scheme for the discretization of Eq. 2.13 in every two-phase cell [57]. The length l (perpendicular distance between cell centre and interface) is adjusted to match the given volume fraction with that of the reconstructed interface to locate the interface.

4. The next sweep in the y-direction (Eq. 2.9) is performed leading to the final distribution of volume fraction field $\alpha^{n+1}_{i,j}$. Also, the intermediate level set function is advanced in the y-direction by solving,

$$\frac{\partial \phi}{\partial t} + v\frac{\partial \phi}{\partial y} = 0. \tag{2.20}$$

The scheme is the same as mentioned in step 2.

5. The interface is again reconstructed based on the newly obtained values of void fraction and level set function as described in step 3.

6. With the advancement in time, ϕ loses the signed normal distance property. Therefore, the level set function is reinitialized after each time step based on the reconstructed interface by following the algorithm of Sussman *et al.* [49].

The solution methodology can be made second order accurate by alternating the sweep direction in each time step [54].

2.2.8 Surface tension model

The complex topological changes of the fluid interface require an efficient modeling of the surface tension. The continuum surface force model (CSF) of Brackbill *et al.* [52] has been incorporated for the present study. The interfacial surface area force $\mathbf{f}_{sa}$, in general, is defined as,

$$\mathbf{f}_{sa} = \mathbf{f}^{\mathrm{n}}_{sa} + \mathbf{f}^{\mathrm{t}}_{sa}, \tag{2.21}$$

where subscript n and t denote the normal and tangential components. These components are defined as $\mathbf{f}_{sa}^{\mathrm{n}} = \sigma\kappa\hat{\mathbf{n}}$ and $\mathbf{f}_{sa}^{\mathrm{t}} = \nabla_s\sigma$, where σ is the surface tension coefficient, κ is the curvature and ∇_s is the surface gradient. Hence,

$$\mathbf{f}_{sa} = \sigma\kappa\hat{\mathbf{n}} + \nabla_s\sigma \tag{2.22}$$

Due to the absence of temperature and concentration gradient along the surface, $\nabla_s\sigma$ can be neglected. The surface tension force per unit volume can be defined as

$$\mathbf{f}_{sv} = \mathbf{f}_{sa}\delta_s \tag{2.23}$$

where δ_s is the Dirac delta function which is zero everywhere except at the interface. Hence, the surface tension term (Eq. 2.2) has the form,

$$\mathbf{f}_{sv} = \sigma\kappa\hat{\mathbf{n}}\delta_s, \tag{2.24}$$

where the calculation of κ and $\mathbf{n}$ has been described in Section 2.2.6.

2.2.9 Discretisation scheme

The continuity and momentum equations are discretized in time as,

$$\nabla \cdot \mathbf{v}^{n+1} = 0 \tag{2.25}$$

$$\begin{aligned}\mathbf{v}^{n+1} &= \mathbf{v}^{n} + \left(-\nabla\cdot\left(\mathbf{v}^{n}\mathbf{v}^{n}\right)\right)\Delta t + \left(\mathbf{g}\right)\Delta t \\ &+ \left(\frac{\left[-\nabla p^{n+1} + \nabla\cdot 2\mu\left(\phi^{n}\right)\mathbf{D}_{v}^{n}\right] + \sigma\kappa\left(\phi^{n}\right)\nabla H\left(\phi^{n}\right)}{\rho\left(\phi^{n}\right)}\right)\Delta t,\end{aligned} \tag{2.26}$$

where $\mathbf{D}_v = \frac{1}{2}\left\{(\nabla\mathbf{v}) + (\nabla\mathbf{v})^T\right\}$ is the rate of deformation tensor and Δt is the time step.

The staggered grid arrangement of the Marker-in-Cell (MAC) algorithm is used for the spatial discretization of the governing equations. The convective terms in the momentum equation are discretized using a second order essentially non-oscillatory (ENO) scheme as described by Chang *et al.* [55] and the remaining space derivatives are discretized using central differencing. The discretized momentum equations are solved explicitly for known values of void fraction α and level set function ϕ at time t^n, which gives rise to an intermediate velocity field $\tilde{\mathbf{v}}$. In order to enforce continuity,

a pressure Poisson equation is solved using the preconditioned biconjugate gradient (BI-CGSTAB) method to obtain the pressure corrections p'. After obtaining the pressure correction values, the intermediate velocity field is corrected to obtain the final updated values at t^{n+1}. By using the updated velocity field, the updated void fraction α^{n+1} and level set ϕ^{n+1} values are obtained followed by reconstruction of the interface.

2.2.10 Time step restriction

The employed solution procedure has accuracy of second order in space and first order in time. The explicit updation of convective, viscous, surface tension and gravity terms places restrictions on the maximum allowable time step size in order to ensure stability of the solution.

The convection time step restriction is given by,

$$\Delta t_{conv}\left(\frac{|u|_{max}}{\Delta x}+\frac{|v|_{max}}{\Delta y}\right)\leq 1. \tag{2.27}$$

The viscous time step restriction is given by,

$$\Delta t_{visc}\left\{\frac{\mu_l}{\rho_l}\right\}\left(\frac{2}{\Delta x^2}+\frac{2}{\Delta y^2}\right)\leq 1. \tag{2.28}$$

The restriction on timestep due to surface tension terms is given by

$$\frac{C_\phi \Delta t_s}{\Delta x}<\frac{1}{2}, \tag{2.29}$$

where C_ϕ is the capillary wave phase velocity given by,

$$C_\phi=\left[\frac{\sigma\pi}{\Delta x(\rho_l+\rho_v)}\right]^{1/2}. \tag{2.30}$$

Thus, the capillary time step limit can be given by,

$$\Delta t_s<\left[\frac{(\rho_l+\rho_v)\Delta x^3}{4\pi\sigma}\right]^{1/2}. \tag{2.31}$$

Finally, the stability restriction due to gravity can be expressed as,

$$\frac{v_g \Delta t_g}{\Delta x}\leq 1, \tag{2.32}$$

where v_g is the gravity induced velocity $v_g = g\Delta t_g$.

The minimum value of Δt_{conv}, Δt_{visc}, Δt_s and Δt_g is employed as the timestep for all the calculations.

2.3 Gerris solver

In addition to the inhouse CLSVOF solver used for the computations of chapter 4, the open source solver *Gerris* [58,59], developed by Popinet, has been employed for the results presented in chapters 5 and 6. *Gerris* is an open source software used for the solution of the partial differential equations describing fluid flow. Some salient features pertaining to *Gerris* solver are described in the following section.

A volume-of-fluid (VOF) method with capability of reduction in spurious currents at the interface makes it suitable and appropriate for simulating fluid flows with interface, and has been used by many researchers successfully in solving complex fluid flow problems [59–62]. The adopted parallelized finite volume code incorporates a quad/octree discretisation scheme, a projection method and a multilevel Poisson solver, for solution of the time-dependent incompressible Navier-Stokes equations. The advection terms are discretized using the robust second-order upwind scheme of Bell *et al.* [63]. All the variables are collocated at cell centers. The domain is spatially discretized using square finite volumes organized hierarchically as a quadtree. An approximate projection method is used for the spatial discretization of the pressure correction equation and the associated divergence in the Poisson equation. This helps in avoiding the classic problem of decoupling of the pressure and velocity field. A second order accuracy in both space and time is ensured by the implemented numerical schemes. The advection equation for volume fraction is solved by employing piecewise-linear geometrical VOF scheme. This scheme is generalized to work on the quad/octree, in order to allow variable spatial resolution along the interface. The accurate estimation of the surface tension terms is ensured by employing a combination of a balanced-force CSF approach [56,64], and a height-function based curvature estimation [65,66]. The comprehensive reports of Popinet [58,59,67] covers the detailed methodology and code validations.

Additionally, *Gerris* is equipped with dynamic adaptive mesh refinement (AMR) ability that allows more number of computational cells to be used near the desired regions dynamically [58]. A dynamic load balancing algorithm ensures that the computational load is efficiently distributed across the processors during a parallelized simulation. For the two phase electro hydrodynamic simulations, *Gerris* has been chosen because the electro-hydro module [22] of Gerris is capable of solving the incompressible Navier−Stokes equations coupled with an electric potential and electric charge density accurately [68,69]. In view of the aforementioned features, the

selected solver is considered to be an ideal choice for our computational requirements and have been accordingly employed for performing the simulations pertaining to chapters 5 and 6.

2.4 Electro-hydrodynamic model

The basic programming paradigm related to the electro-hydrodynamic simulations are discussed in this section. The governing equations pertaining to the hydrodynamics of the flow are,

$$\nabla \cdot \mathbf{v} = 0, \tag{2.33}$$

$$\begin{aligned} \rho\left[\partial \mathbf{v}/\partial t + (\mathbf{v}\cdot\nabla)\mathbf{v}\right] &= -\nabla P + \nabla\cdot[\mu(\nabla\mathbf{v} + \nabla\mathbf{v}^{\mathbf{T}})] \\ &+ \gamma\kappa\mathbf{n}\delta + \nabla\cdot\mathbf{M}, \end{aligned} \tag{2.34}$$

$$\partial\alpha/\partial t + \nabla\cdot(\mathbf{v}\alpha) = 0, \tag{2.35}$$

where $\mathbf{v}(u, v)$ is the velocity field with components u, v along x- and y-axis, respectively. The pressure field is represented by P and volume fraction is denoted by α. The effect of surface tension γ is considered by inserting the continuum surface force (CSF) model of Brackbill *et al.* [52] into the momentum equations.

The Maxwell's stress tensor for the electric field $\mathbf{M}$ is given by $\mathbf{M} = \epsilon_o\epsilon[\mathbf{E}\otimes\mathbf{E} - \frac{1}{2}(\mathbf{E}\cdot\mathbf{E})I]$. The Gauss Law can be written in terms of the electric displacement ($\mathbf{D} = \epsilon\mathbf{E}$) as $\nabla\cdot\mathbf{D} = \nabla\cdot(\epsilon\mathbf{E}) = q_v$ where, ϵ and q_v denote the absolute permittivity of the fluid and the volume density of free charges inside the domain, respectively. Furthermore, in the absence of a magnetic field, the irrotational ($\nabla\times\mathbf{E} = 0$) electric field $\mathbf{E}$ can be written in terms of the electric potential (ψ) as $\mathbf{E} = -\nabla\psi$.

For perfect dielectric fluids, no free charge carriers exist ($q_v = 0$) and hence, the electric field becomes

$$\nabla\cdot(\epsilon\mathbf{E}) = 0. \tag{2.36}$$

Equation (2.36) can be expressed in terms of electric potential as

$$\nabla\cdot(\epsilon\nabla\psi) = 0. \tag{2.37}$$

Thus, the electrostatic force acting on the dielectric fluids ($\mathbf{f_e}$) can be represented as

$$\mathbf{f_e} = \nabla\cdot\mathbf{M} = -\frac{1}{2}\epsilon_o\mathbf{E}\cdot\mathbf{E}\nabla\epsilon_r, \tag{2.38}$$

where ϵ_o is the permittivity of free space and $\nabla\epsilon_r$ is the gradient of dielectric constant acting along the interface.

For leaky dielectric fluids, Gauss law can be rewritten in terms of electric potential as $\nabla \cdot (\epsilon \nabla \psi) = -q_v$. The charge conservation equation for volumetric charge density is given as,

$$\frac{\partial q_v}{\partial t} + \nabla \cdot (q_v \mathbf{V}) \quad = -\nabla \cdot (\sigma \mathbf{E}). \tag{2.39}$$

Here, σ represents the electrical conductivity of the fluids. For leaky dielectric fluids, the electrical relaxation time scale is smaller than the time scale of fluid motion due to which charge accumulates at the interface almost instantaneously. Hence, Eq. 2.39 can be simplified with a quasi-static assumption and expressed as $\partial q_v/\partial t = -\nabla \cdot (\sigma \mathbf{E}) = \nabla \cdot (\sigma \nabla \psi)$. Hence, the electrostatic force ($\mathbf{f_e}$) acting on the fluids with the leaky dielectric assumption can be written as,

$$\mathbf{f_e} = \nabla \cdot \mathbf{M} \quad = -\tfrac{1}{2}\epsilon_o \mathbf{E} \cdot \mathbf{E} \nabla \epsilon_r + q_v \mathbf{E}. \tag{2.40}$$

The electrical properties of the fluids are volume averaged as

$$\epsilon = \epsilon_s \alpha + \epsilon_d (1 - \alpha), \tag{2.41}$$

$$\sigma = \sigma_s \alpha + \sigma_d (1 - \alpha). \tag{2.42}$$

The detailed and systematic derivation related to the evolution of electrical body force has been discussed in the Appendix. The derivation also clarifies as to how the divergence of the Maxwell stress tensor contributes as a body force.

Chapter 3

Experimental Methodology

3.1 Introduction

The mysteries related to cancer and metastasis still remain unresolved to a great extent. Since past few years, many researches and oncologists have been trying to implement their expertise in exploring the nature and behavior of cancer cells in human bodies. In the present work, we make an attempt to understand the flow dynamics and survival ability of cancer cells through constricted microchannels that mimic micro capillaries in human body. The results obtained are discussed in Chapter 7. In this chapter we discuss the methodology adopted in carrying out the experimental work.

3.2 Fabrication of microchannel

The aim of the present work is to observe the behavior of live cancer cells in capillary like micro-environment and to observe the phenomenon of metastasis. In this regard, a constricted micro channel of 7 μm as minimum width was designed as shown in Fig. 3.1. The length of the channel is 3 mm and length of the constricted portion is 200 μm. The width of the portions of the channel from entry to the constriction and from the constriction to the outlet is 35 μm. The materials generally used for fabrication of microchannels are Elastomers (e.g. Polydimethylsiloxane (PDMS), Polymethylmethacrylate (PMMA), Norland Adhesive 81 (NOA), etc.). Among the above mentioned materials, PDMS is widely used because it has following properties.

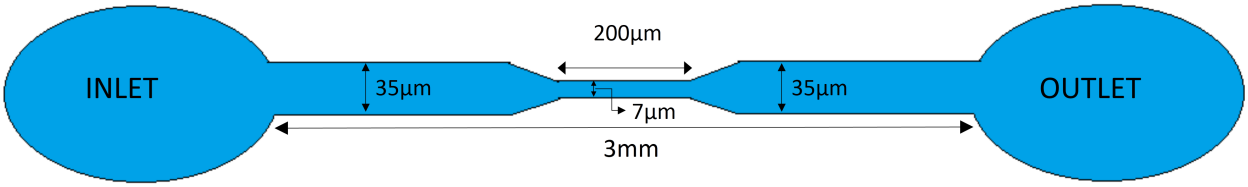

Figure 3.1: The basic design of the constricted microchannel (not to scale). The channel is 3 mm long with a cross section of 35 μm $\times$ 7 μm on either side of the constriction and 7 μm $\times$ 7 μm for the 200 μm constricted length in the middle.

1. Rapid prototyping
2. Low cost
3. Good optical properties

3.2.1 Equipment used for fabricating the microchannels

Following materials and instruments were mainly used for the fabrication of microchannel -

1. Silicon wafer (Su8 Master)
2. Glass plate
3. Glass rod
4. Disposable cup
5. Hot Air Oven/ Hot plate
6. Vacuum Pump
7. Acetone
8. Soap
9. IPA solution
10. Scotch tape

11. Master
12. PDMS
13. Oxygen Plasma chamber
14. Lint free Tissue paper
15. Aluminium foil
16. Nylon Ring

3.2.2 Procedure of fabricating channel

The following basic steps were adopted for making the microchannels.

1. **Preparation of Su8 Master (Silicon Wafer):** Based on our design, the master was provided to us by the Centre for Nano Science and Engineering (CeNSE) of Indian Institute of Science, Bangalore. An image of the Su8 master is shown in Fig. 3.2.

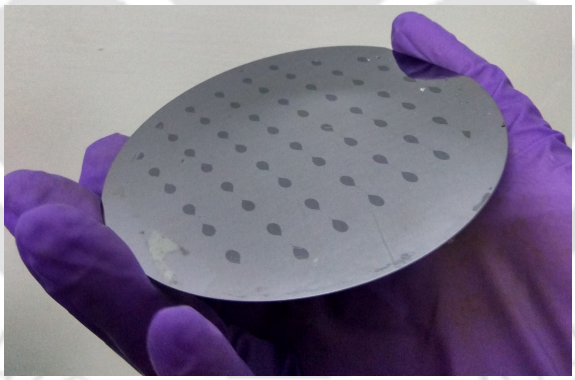

Figure 3.2: Su8 master for microchannel fabrication.

2. **Cleaning of SU8 Master (Silicon Wafer):** The master is washed with DI water and let to be dry.
3. **Preparing the base working plate:** A square sized glass plate serves as base over which all the fabrication work are done. At first, it was cleaned with soap, then acetone and after that it was kept in hot air oven to dry. Over the

plate a piece of aluminium foil was placed. The Master was placed upon the foil.

4. **Preparing the PDMS solution:** The SYLGARD 184 silicon elastomer was mixed with the cross linker in the ratio of 10:1 by weight. Mixture was stirred with glass rod for 1 min as shown in Fig. 3.3. After that the mixture was put in vacuum desiccator to be degassed until all the gas bubbles are removed as shown in Fig.3.4.

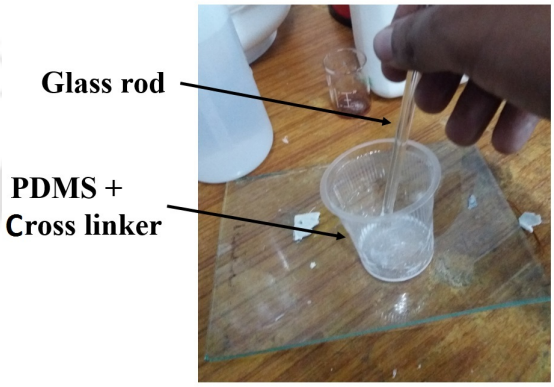

Figure 3.3: Mixing SYLGARD 184 silicon elastomer with the cross linker by stirring with glass rod.

Figure 3.4: Degassing the PDMS solution.

5. **Preparing the mould:** A nylon ring (refer Fig. 3.5) was placed carefully over the master kept on top of the aluminium foil. The prepared PDMS is slowly poured over the master bounded by Nylon ring and thus the mould is

prepared. Figure 3.6 shows an image of the mould. The mould is placed over the Hot-plate for 30 mins by keeping it over the aluminium foil. Once the PDMS solidifies, the mould is taken off from the Hot-plate and kept aside to be cooled at room temperature.

Figure 3.5: Nylon ring made to be placed upon the master.

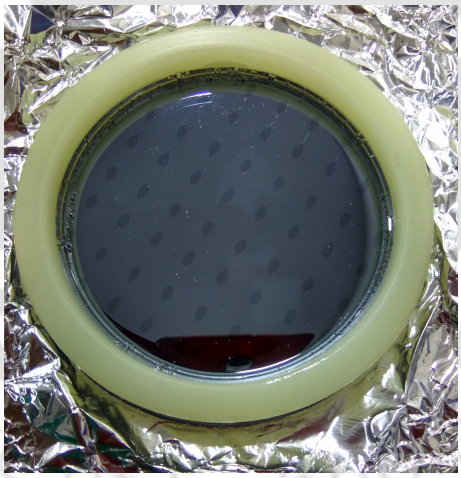

Figure 3.6: The PDMS poured over the master bounded by the nylon ring.

6. **Making the PDMS Channel:** The PDMS cake is then taken out of the Master. The PDMS cake contains many channels in it. By making use of surgical blade, individual channels are cut out as shown in Figs. 3.7 and 3.8. With the help of punching tool thorough holes are punched at the inlet and outlet (shown in Fig. 3.9). The open PDMS channels are kept free of

contamination by using scotch tape. Glass slides are cleaned with acetone. IPA solution is poured on the surface of glass slide that would be in contact with the open PDMS channel. Both the PDMS open channel and glass slides (as shown in the Fig. 3.10) are handled very carefully maintaining totally clean environment and treated in Oxygen plasma chamber (Fig. 3.11) for a minute. The PDMS open channel thus gets attached to the glass slide. Now a closed microchannel is ready for use (Fig. 3.12). All the channels are made this way one at a time and preserved carefully wrapping with scotch tape.

Figure 3.7: Cutting the solidified PDMS to make channels.

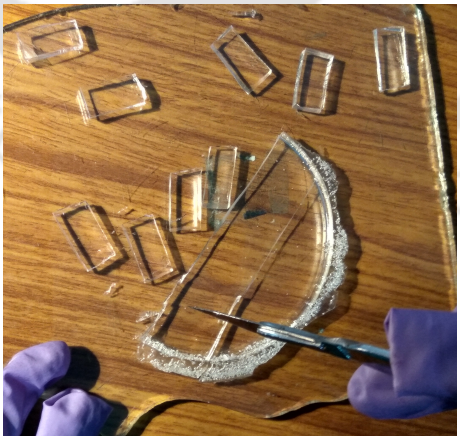

Figure 3.8: Surgical blade is used to cut out the individual channels from the solidified PDMS cake.

Figure 3.9: Thorough holes for inlet and outlet are punched with the help of punching tool.

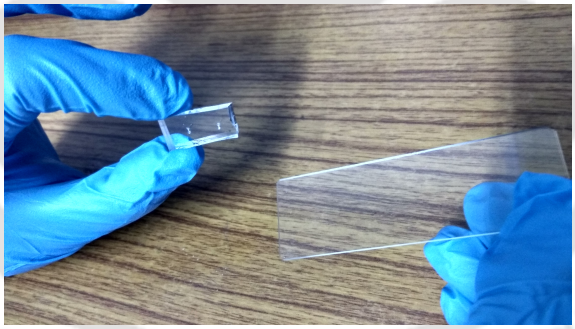

Figure 3.10: Cleaned glass slide and PDMS open channel.

3.3 Cultivation of HeLa cells

HeLa cells are cultured in laboratories around the world. They are all descended from cells removed from a cancer (of the cervix) of Henrietta Lacks who died of her disease in 1951. For the present study, these cells were obtained from the repository of the National Centre for Cell Science (NCCS), Pune, India, and cultured in BioScience and BioEngineering (BSBE) department of IIT Guwahati. The cells were cultured in Dulbecco's Modified Eagle's Medium (DMEM) high glucose, con-

Figure 3.11: An image of the oxygen plasma chamber.

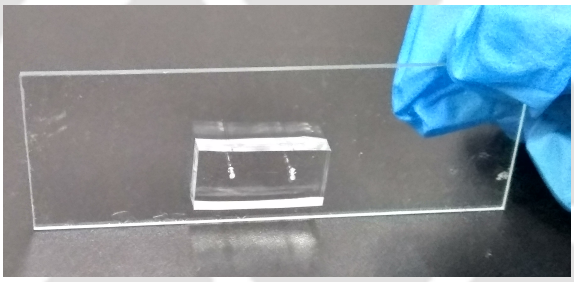

Figure 3.12: An image of the fabricated microchannel.

taining 10% fetal bovine serum (FBS) and 1% penicillin/streptomycin (100 U/ml; 0.1mg/ml), in humidified 5% CO_2 at 37°C.

3.3.1 Materials needed

The following materials and instruments are required for cell culture.

1. Pipette
2. Gloves
3. Eppendorf
4. Laminar Hood
5. DMEM

6. Cell culture dish
7. Tissue paper
8. Trypsin-EDTA
9. PBS
10. Acetone

3.3.2 Procedure of cell culture

The cells are cultured on the Laminar Hood table following the procedure narrated below.

1. HeLa cells were grown in a 60 mm cell culture dish to its confluency.
2. On the day of the experiment, cells were taken out from the plates.
3. After removing the culture medium from the dish, the cells were washed with phosphate-buffered saline (PBS) to remove the traces of the DMEM medium.
4. Further, 80 μl of trypsin-EDTA was added to the cells in the culture dish and incubated at 370 °C for 2-3 minutes to get the cells detached.
5. Having confirmed the detachment of the cells through microscopic visualization, 1ml of DMEM was added on the cells to deactivate the trypsin enzyme.
6. The detached cells were then taken in a 1.5 ml tube for further experimental procedures.

3.4 Experimental set up

In all the experiments, HeLa cells are used. The cells were grown and maintained in DMEM. In order to perform the experiments the following instruments and materials were required.

1. Image acquisition system
2. Sample injection system

Figure 3.13: Experimental setup.

3. Syringe
4. Polyethylene Tubing
5. High speed camera
6. Gloves
7. Tissue paper
8. Acetone

An image of the experimental set up is shown in Fig. 3.13. The microchannel was placed on the stage of the microscope and semi-rigid Polyethylene tubing of inner diameter 0.38 mm and outer diameter 1.09 mm (Prolab Marketing, India) was connected to the inlet and outlet. Figure 3.14 shows a magnified image of the channel placed on the stage of the microchannel with connecting tubes inserted at the inlet and the outlet. The concentration of cells used in the experiments was around 1×10^5 cells per ml of medium, in which approximately 95% of the cancer cells were live initially in all the experiments. The cells were transferred from the Eppendorf tube to a syringe as shown in Fig 3.15. The syringe was fixed securely in the syringe pump. The connections to the inlet and outlet of the channel were secured well with close observation. When the entire facility was ready, the microscope and pump were connected to a power source. As the syringe pump started to operate, the cells suspended in DMEM medium started to fill the connecting tube and flow

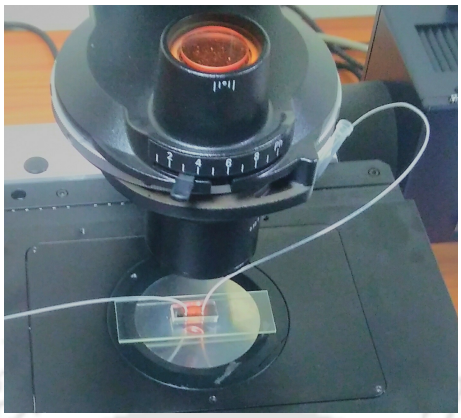

Figure 3.14: A magnified image of the channel placed on the stage of the microchannel with connecting tubes inserted at the inlet and the outlet.

Figure 3.15: Filling the syringe with HeLa cells suspended in DMEM medium.

through the microchannel. The average velocity of blood (usually measured in cm/s) generally varies from 0.03 to 40 cm/s as the blood flows through the vena cava, capillaries and aorta [70]. The cells suspended in media were allowed to flow passively at constant flow rate of 30 μl/h. As per the given flow rate, the average velocity of the external fluid in the constriction (7 μm width) was found to be 17 cm/s and in the rest of the channel (width 35 μm) the velocity was 3.4 cm/s. The flow gradually became steady and the motion of the cells were observed and recorded at a high frame rate of 50000-60000 fps using the video module of the Leica LAS software. The videos were then deconvoluted to obtain images at required time instants. After the experiment was over, Acetone was used to clean the microscope and other necessary equipment.

Chapter 4

Migration of a Droplet in a Cylindrical Tube in the Creeping Flow Regime

The motion of a neutrally buoyant droplet in a capillary tube is investigated in the creeping flow regime. A CLSVOF approach is employed to capture the deformable interface. The effect of drop size, capillary number and viscosity ratio on the dynamics of deformation and break up is thoroughly studied by varying these pertinent parameters in a wide range. A small drop tends to move with the centerline velocity of the external fluid, however a large drop experiences more drag due to its close proximity with the walls of the tube. The deformation at the interface is found to be stimulated by the subtle interplay between the capillary and viscous forces. It is observed that a traversing drop develops an indent at its trailing end which may further lead to penetration of outer fluid and disintegration of the drop into several daughter droplets. Based on the viscosity ratio, different modes of breakup of the droplet has been observed. The critical value of the capillary number, beyond which the drop first breaks, has been computed for drops of different sizes and viscosity ratios.

The contents in this chapter have been published as Nath, B., Biswas, G., Dalal, A., and Sahu, K.C. (2017) 'Migration of a droplet in a cylindrical tube in the creeping flow regime', *Physical Review E*, vol. **95**, pp. 033110 (available online, DOI: https://doi.org/10.1103/PhysRevE.95.033110).

4.1 Introduction

The study of droplet dynamics in microchannels or capillary tubes depends on various parameters which are responsible for the topological changes at the interface separating the fluids. Two of the dictating parameters are the viscous and surface tension forces, which are important at small scales. The relative strength of both the forces is expressed by the capillary number (Ca $\equiv \mu_s V/\gamma$, where μ_s is the viscosity of the continuous phase, V is the velocity scale and γ is the interfacial tension). Low values of Ca indicate that the stresses due to interfacial tension are stronger than the viscous stresses. Subjected to such conditions, a migrating drop tends to minimize its surface area by changing to a spherical shape. On the other hand, when Ca is higher, the viscous stresses dominate resulting in large droplet deformation, which in turn leads to evolution of asymmetrical droplet shapes.

The motion of a droplet inside a channel/pipe in the Stokes flow limit has been studied theoretically by many researchers in the past decades. Hetsroni *et al.* [71] studied the motion of a small undeformed droplet traversing along the axis of the tube and obtained an equation for the dimensionless droplet velocity. Brenner [72] and Bungay & Brenner [73] conducted a similar study and obtained an equation for the excess dimensionaless pressure drop. They also observed that depending on the viscosity ratio the overall pressure drop can be either positive or negative in the presence of the drops. Hyman & Skalak [74, 75] investigated the case of equally spaced train of neutrally buoyant concentrically located drops considering both deformed and undeformed droplet shapes. Chan & Leal [76], Nadim & Stone [77] studied the drop motion addressing the effect of the viscosity ratio, $\lambda(\equiv \mu_d/\mu_g)$ and the capillary number Ca, where viscosities of dispersed fluid and continuous fluid are μ_d and μ_s, respectively. Recently, Konda *et al.* [78] investigated the motion of an air bubble in a converging-diverging channel by conducting two-dimensional numerical simulations. It is found that the bubble undergoes oblate-prolate deformation periodically at the early times, which becomes chaotic at the later times in the inertial regime. This occurs due to path instability as well as the Segré-Silberberg effect [79].

Sutera and co-workers [80, 81] experimentally studied the motion of solid hemispheres and caps in Newtonian fluids assuming it as a model for motion of erythrocytes in capillaries. Prothero & Burton [82, 83] investigated the motion of a train of gas bubbles in a Newtonian fluid as a model for blood flow through capillaries. However, the experiments relevant to the present work are the studies conducted

by Karnis *et al.* [84], Olbricht [4], Ho & leal [5] and Olbricht & Kung [2]. They have investigated the dynamics of droplets migrating through channels or tubes at low Reynolds numbers. Ho & leal [5] also investigated the effects of the capillary number up to $O(10^2)$ and viscosity ratios on the shape of the drops migrating inside a capillary tube. Olbricht & Kung [2] experimentally studied the motion of drops in a capillary tube for a large range of the capillary numbers, drop sizes and viscosity ratios. They reported the effects of drop size and viscosity ratio on the critical capillary number, above which the drop breakup occurs.

Most numerical investigations on the migration of bubble/drop in Poiseuille flow at low Reynolds number (in the Stokes flow approximation) were carried out using boundary-integral method (see e,g. [3, 6, 85–89]). It is to be noted here that boundary-integral method does not solve the complete Navier-Stokes equations. A few others researchers, on the other hand, solved the Navier-Stokes equations and studied the motion of drops in channels using finite-difference/finite-volume/front tracking methods [78, 90] by conducting two-dimensional numerical simulations. A neutrally buoyant drop in a fully developed channel flow is capable of crossing streamlines as a consequence of drop deformation and formation of a variety of transient non-spherical shapes, in contrast to non-deformable drops and particles. Hence, such a complex situation demands dynamic simulation and high computational accuracy. Moreover, although several researchers numerically investigated the breakup of a droplet in capillary tubes, it has been observed that most of them terminate their computations as the thread of the outer fluid becomes thinner as the time progresses, and when the numerical method adopted becomes difficult to resolve the interface further in order to get the accurate physics. Thus, the exact physics of post breakup scenario of the drop is a relatively unexplored field.

In the present study, the dynamics of a single droplet migrating inside a tube is investigated in a creeping flow regime. A bespoke coupled level-set and volume-of-fluid approach is used. We thoroughly investigate the deformation and translational motion of an axisymmetric drop in a tube, and present its behaviour subject to varied parametric conditions. The influence of the relevant physical parameters, such as the ratio of droplet radius to tube radius, the capillary number and the viscosity ratio between the two phases are discussed in detail. Since the study of the droplet breakup phenomenon is very important from the practical applications point of view, the present work attempts to capture the critical conditions for the breakup of the droplet by studying the dynamics of single drop in a cylindrical tube.

The rest of the chapter is organised as follows. In Sec. 4.2, we outline the formulation and discuss the validation of the present numerical solver. The results are presented in Sec. 4.3, and a brief summary in Sec. 4.4.

4.2 Formulation

The motion of an initially spherical droplet of radius a_0 migrating through a cylindrical tube of radius R_0 due to an imposed flow at the inlet of a tube (of radius R_0 and length $L = 40R_0$, as shown in Fig. 4.1) is considered. The radius of the droplet in the present study lies in the range of $0.1R_0$ to $0.95R_0$. The droplet and the fluid inside the tube are immiscible. The fluids are also assumed to be incompressible and Newtonian. The viscosity and density of the dispersed phase (droplet) and continuous phase (fluid inside the cylinder) are (μ_d, ρ_d) and (μ_s, ρ_s), respectively. The flow is assumed to be axisymmetric. Thus, an axisymmetric cylindrical coordinate system (r, z) is used to model the flow dynamics, where r and z represent the radial and axial coordinates, respectively. Initially, the bubble is located at $z = z_0 = 2R_0$. In the present study, the effect of acceleration due to gravity, $\mathbf{g}$ is neglected.

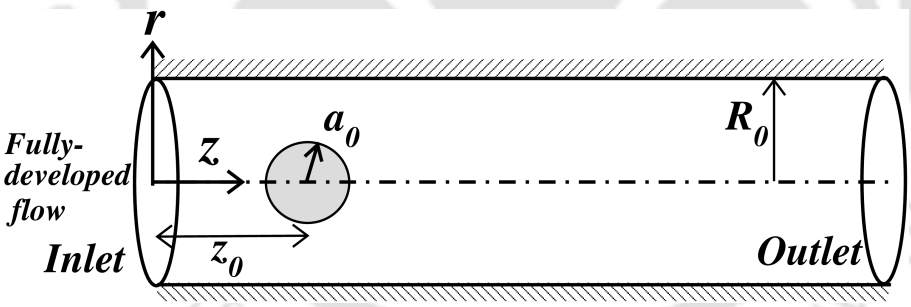

Figure 4.1: Schematic diagram (not to scale) showing the initial flow configuration of a droplet of radius a_0 located at (r_0, z_0) in a cylindrical tube of radius R_0. A fully-developed flow is imposed at the inlet of the tube. The length L of the tube is taken to be equal to $40R_0$.

4.2.1 Numerical methods

The problem is governed by the single set of continuity and Navier-Stokes equations for treating a single fluid continuum. The two-dimensional axisymmetric setup has

been considered by solving the same set of governing equations as described in Sec. 2.2.1. The inhouse CLSVOF solver, described extensively in Sec. 2.2, is employed for performing the numerical simulations. The aforementioned CLSVOF method has been used by many researchers successfully for solving a variety of interfacial flow problems of scientific interest [91–95].

4.2.2 Initial and boundary conditions

In order to solve the governing equations, the following initial and boundary conditions are implemented. The fluids are stationary at $t = 0$, i.e. at the starting of the computations. The fully-developed velocity profiles are imposed at the inlet of the tube ($z = 0$), which are given by

$$u(r) = 2V\left(1 - \frac{r^2}{R_0^2}\right), \quad \text{and} \quad v(r) = 0, \tag{4.1}$$

where V is the average velocity of the imposed flow. The no-slip and no penetration conditions ($u = v = 0$) are imposed at the tube wall, i.e. at $r = R_0$. The outlet boundary conditions, which are Neumann boundary conditions for the velocity components and fixed pressure condition are applied at the outlet of the tube. They are given by

$$\frac{\partial u}{\partial z} = \frac{\partial v}{\partial z} = 0, \quad \text{and} \quad p = p_0, \tag{4.2}$$

at $z = L$.

4.2.3 Non-dimensionalisation

The radius of the tube, R_0 and average imposed velocity, V at the inlet of the tube are used as the length and velocity scales, while μ_s and ρ_s are used as the viscosity and density scales, respectively. The results obtained from the numerical simulations are presented in terms of dimensionless parameters. The aspect ratio, a, which is given by a_0/R_0, i.e. the ratio of the initial droplet radius to the tube radius. The other dimensionless parameters are the Reynolds number, $Re \equiv \frac{\rho_s V R_0}{\mu_s}$, the capillary number, $\mathrm{Ca} \equiv \frac{\mu_s V}{\gamma}$, the density ratio, $\eta = \frac{\rho_d}{\rho_s}$ and the viscosity ratio, $\lambda = \frac{\mu_d}{\mu_s}$. In the present study, the Reynolds number is assumed to be small ($Re < 1$), i.e. the influence of inertia can be assumed to be very small compared to the viscous effect. Furthermore, as we study the migration of a neutrally buoyant droplet, we

set $\eta = 1$ in the simulations. Thus, the problem is essentially governed by three dimensionless parameters, namely, a, Ca and λ. The results are presented in terms of dimensionless time, $\tau \equiv tV/R_0$.

4.2.4 Fluid properties

The fluid properties are chosen based on the experimental work of Ho & Leal [5]. In their study, the suspending medium was 95.75% by weight glycerine in water at 25°C. The drops that were suspended comprised of a solution of silicone oil (dow corning 200 fluid, a dimethyl silioxane polymer) and carbon tetrachloride. The surface tension was measured to be 22×10^{-3} N/m for the interface between the glycerine and mixture of silicone oil and carbon tetrachloride. Four grades of silicone oil having different viscosities but almost equal densities (1251 kg/m^3) were used. In the present computational study, these fluid properties are deployed to validate the code. The ratio of the viscosity of the droplet fluid to that of the suspending fluid has been varied in the range of 0.001 to 2.04. The droplet size is varied from $a = 0.1$ to 0.95 and Ca is varied from 0.1 to 1.

4.2.5 Validation

The present numerical solver is validated by comparing the results obtained from the present study with the corresponding results reported by the previous experimental and numerical investigations [3, 5, 6, 96]. The qualitative and quantitative comparisons obtained are reported below. First, a grid convergence test is conducted based on which a suitable grid size is chosen for generating the rest of the results presented in this study.

4.2.5.1 Grid independence test

The grid convergence test is conducted by simulating the migration of a droplet in a cylindrical tube with aspect ratio, $a = 0.7$. The rest of the dimensionless parameters are Ca = 1.0 and $\lambda = 0.1$. In Fig. 4.2, the temporal variations of the dimensionless drop velocity, V_d for different grid-meshes (1000×25, 1600×40, 2000×50, 3200×80) are shown. We found that the steady velocity of the droplet obtained using 1000×25, 1600×40, 2000×40, 3200×80 are 2.029, 2.05, 2.057 and 2.07, respectively. The

percentage differences in the steady velocity of the droplet are 1.07%, 0.33% and 0.67%, when we compare V_d obtained using 2000×50 with that obtained using 1000×25, 1600×40 and 3200×80, respectively. In view of this, and optimising the computational time and cost without compromising the accuracy of the results, 2000×50 grid-meshes are used to generate the rest of the results presented in this study. The corresponding mesh size of 0.02 is employed in all the simulations. The time step was chosen such that the Courant-Friedrichs-Lewy (CFL) and capillary time step conditions are satisfied [91].

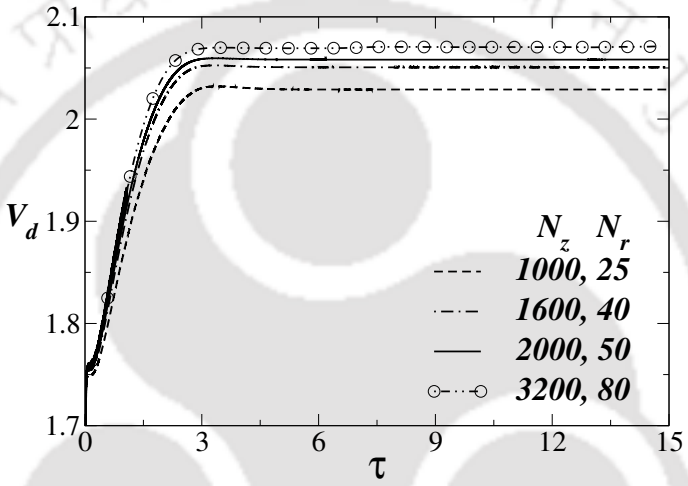

Figure 4.2: Comparison of the velocity of the drop, V_d for different grid-meshes (1000×25, 1600×40, 2000×40, 3200×80). The parameters are Ca = 1.0, $\lambda = 0.1$ and $a = 0.7$. N_z and N_r represent the number of grids in the z and r directions of the computational domain, respectively.

4.2.5.2 Qualitative comparisons

The experimental work of Olbritch & Kung [2] shows the steady shapes of a droplet migrating in a capillary tube for $a = 0.95$ and $\lambda = 0.99$. The droplet shapes for Ca = 0.05, 0.10 and 0.16 (from [2]) are shown in Fig. 4.3(a). The corresponding droplet shapes obtained from the present simulations are presented in Fig. 4.3(b), which agree with the experimentally obtained droplet shapes of Olbritch & Kung [2]. The present study focuses on capturing the droplet deformation and breakup while migrating in a tube. The droplet breakup phenomenon forming re-entrant jet was

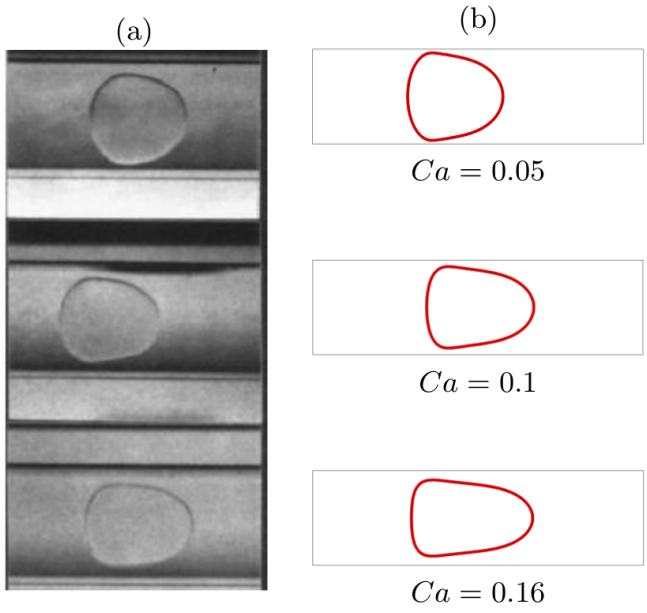

Figure 4.3: Comparison of the steady shapes of a droplet of size $a = 0.95$ migrating in a capillary tube for $\lambda = 0.99$ for Ca = 0.05, 0.10 and 0.16. (a) Experimental results [2], and (b) Present study.

investigated by Guido & Preziosi [96], who compared the numerical simulation results of Tsai & Miksis [3] with the experimental results of Olbritch [4]. We perform numerical simulation in the same configuration considered by these authors. The droplet shapes obtained from the present numerical simulations (panel a) are compared with those of Tsai & Miksis [3] (panel b). The experimentally obtained droplet shapes from Olbritch [4] are also shown in Fig. 4.4(c). It can be seen that our results show excellent agreement with those presented by Tsai & Miksis [3] for the time instants τ=0, 2, 4 and 6.

4.2.5.3 Quantitative comparisons

In order to gain more confidence on our numerical solver, we perform quantitative comparison with the previous investigations. In Figs. 4.5(a) and (b), we study the effect of viscosity ratio λ on the dimensionless droplet velocity, V_d for $a = 0.726$ and 0.914, respectively, and compare with the experimental results of Ho & Leal [5] and the numerical simulation results of Martinez & Udell [6]. It is observed that the present computational results agree well with the computational results of Martinez

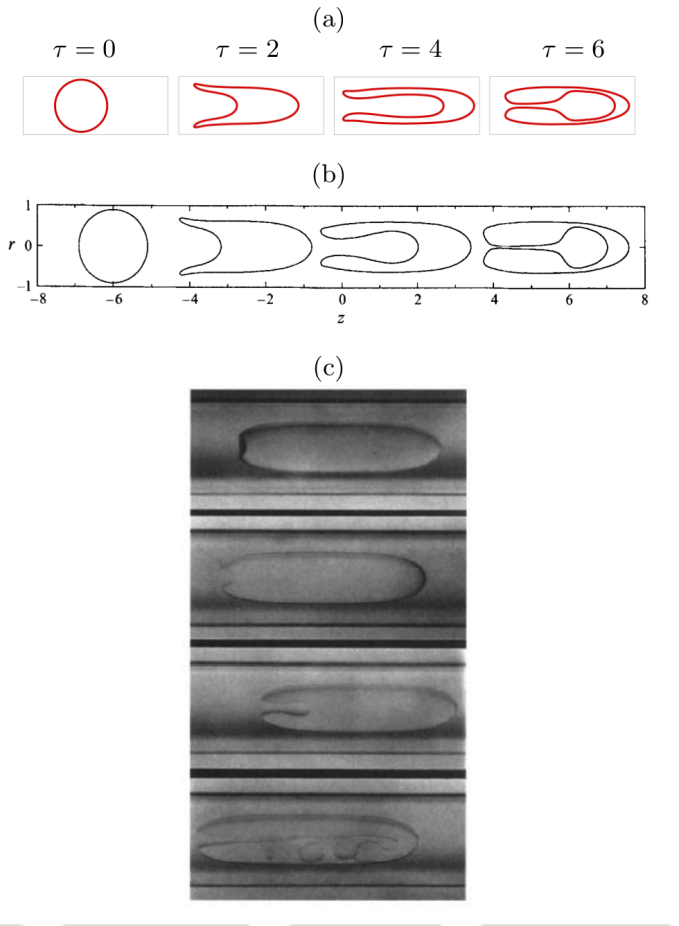

Figure 4.4: Comparison of the evolution of droplet shape: (a) Present study, (b) The results of Tsai & Miksis [3]. (c) The shapes of the droplet obtained by Olbritch [4] in the same configuration. The parameters used are Ca = 1, $\lambda = 0.1$ and $a = 0.9$.

& Udell [6], though it differs from the experimental results of Ho & Leal [5] slightly; however the trend remains same. These results also follow the same trend observed in the theoretical investigation of Hetsroni *et al.* [71] conducted for a small undeformed droplet. They found the dimensionless droplet velocity,

$$V_d = 2 - \frac{4\lambda}{3\lambda + 2} a^2 + O(a^2). \tag{4.3}$$

Note that the values of V_d obtained using Eq. 4.3 defer from the present results and the results of Martinez & Udell [6] and Ho & Leal [5], but the trend (V_d decreases with λ) remains the same. This is because Eq. 4.3 is strictly valid for small and undeformed droplets.

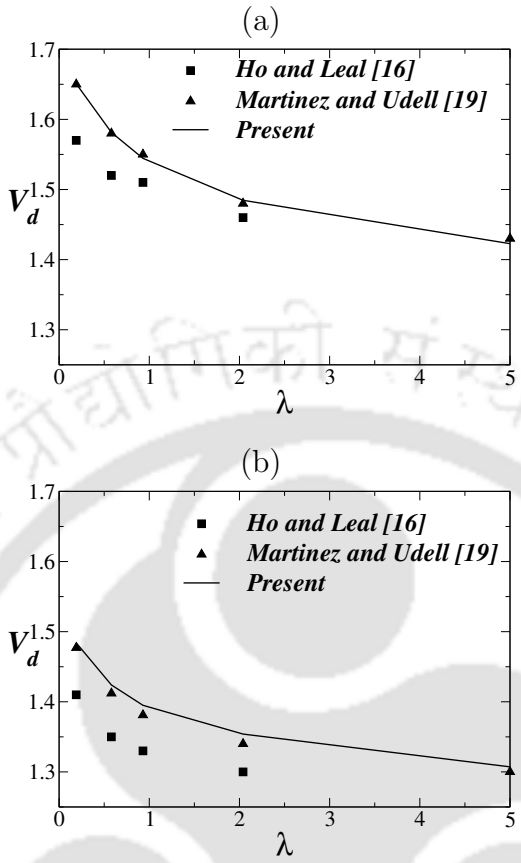

Figure 4.5: The effect of viscosity ratio on the droplet velocity, V_d for (a) a = 0.726 and (b) a = 0.914. Here, Ca = 0.1. The results obtained from the present computation are compared with those presented by Ho & Leal [5] and Martinez & Udell [6].

4.3 Results and discussion

After validating our numerical solver by comparing with the previously reported experimental and numerical results, in this section, we conduct an extensive parametric study by varying the aspect ratio ($a = 0.1 - 0.9$), the capillary number (Ca = 0.1 - 6.52) and the viscosity ratio ($\lambda = 0.001 - 2.5$). The study is carried out for small and big droplets, which undergo deformation without and with breakup at later times as they migrate inside the cylindrical tube.

4.3.1 Dynamics of unbroken droplets

First, we investigate the dynamic of small droplets migrating inside the tube. These droplets do not break, but deform into oblate shapes as they move in the axial direction. The degree of this deformation largely depends on Ca. The aspect ratios ranging from $a = 0.1$ to 0.9 are considered. In this study, we fix the radius of the cylinder and vary the initial droplet radius to vary the aspect ratio, a. Based on the previously reported experimental results, the capillary number is varied from 0.1 to 1, while the viscosity ratio is kept in the range 0.1 to 2.5.

4.3.1.1 Effect of initial droplet size

To understand the effects of droplet size on the dynamics, we consider droplet of different sizes migrating in the cylindrical tube of fixed radius, and thereby varying the aspect ratio, a. The rest of the parameters are Ca = 0.1 and $\lambda = 0.1$. For a droplet moving along the axis of the tube, the droplet velocity, V_d lies between the maximum (centerline) and the average velocities of the undisturbed flow. The maximum or the centerline velocity is twice that of the average velocity in the Hagen-Poiseuille flow. From our basic understanding, it is obvious that if the droplet (placed at the centerline of the tube) is very small in size, it moves almost with the centerline velocity of the tube. However, as the droplet size increases, the steady velocity attained by the droplet is much less than the centerline velocity, but higher than the average flow velocity in the tube. Figure 4.6 depicts these phenomena. We can see that for a droplet for $a = 0.1$ (small droplet), the steady dimensionless velocity of the droplet, V_d is almost equal to 2 and increasing the droplet size gradually decreases the droplet velocity, which reaches to a plateau for $a > 0.6$. This behaviour is also observed (not shown) for film thickness (the thickness between the droplet and wall) as well. The elongated drops are termed as "Taylor drops". Similar findings on droplet velocity and film thickness for long drops were reported in the classical studies of Taylor [97] (experimental) and Bretherton [98] (theoretical).

4.3.1.2 Effect of capillary number

The influence of the capillary number is investigated for a droplet with aspect ratio, $a = 0.7$ migrating inside the fluid stream in a tube. The viscosity ratio, λ is

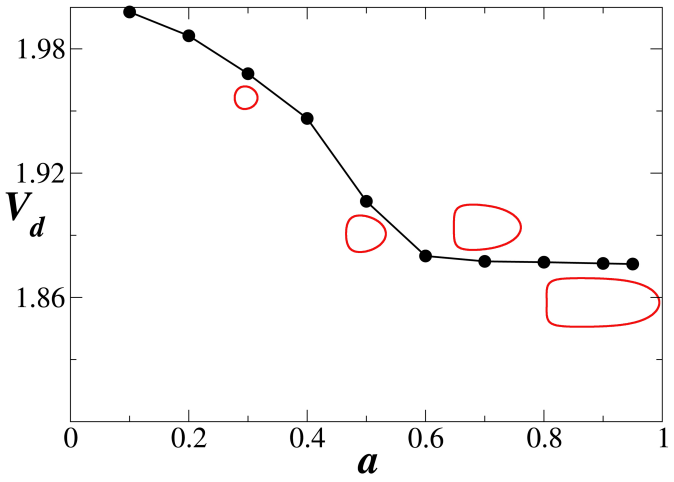

Figure 4.6: The effect of the variation of the aspect ratio, a (i.e initial droplet size) on the droplet velocity, V_d. The steady shapes of the droplet for $a = 0.3$, 0.5, 0.7 and 0.9 are inserted in the plot. The rest of the parameters are Ca $= 0.1$ and $\lambda = 0.1$.

considered to be 0.1. As discussed in the introduction, several researchers in the past have numerically computed the shapes of a droplet suspended in a creeping flow through a capillary tube. In the review of Guido & Preziosi [96], it is reported that with the increase in the value of Ca the droplet becomes elongated in the axial direction. Figure 4.7 depicts the steady shapes of a droplet for different Ca. It can be seen that the droplet elongates when the capillary number is increased. Close inspection of Fig. 4.7 also reveals that with increasing Ca, the front end of the drop becomes more tapered while the curvature at the trailing end decreases. This phenomenon was also observed in the past by Prothero & Burton [82, 83]. It was also reported [5, 81–84] that the onset of a re-entrant cavity appears for Ca ≈ 0.75 in case of $a = 0.726$. Recently, Cherukumudi *et al.* [99] also reported the formation on indentation at the back of a drop for Ca ~ 1. The phenomenon of formation of cavity or indentation can be clearly seen in Fig. 4.7. For Ca ≤ 0.7, we see that no such indentation is formed but when Ca is around unity, a prominent indentation is observed at the trailing edge due to the change of the sign of the curvature. We observe that for large values of the capillary number (Ca > 1, for this set of parameters), a droplet does not reach to a steady shape. For Ca > 1, the indentation grows and allows the continuous fluid to penetrate inside the droplet and beyond a critical value of the capillary number the droplet breaks. This will be discussed in

the next section, while discussing the dynamics of disintegrating droplets. Figure

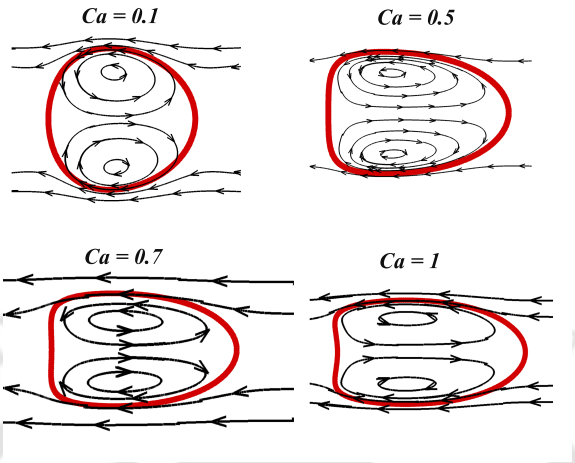

Figure 4.7: The steady shapes attain by a droplet for $a = 0.7$ migrating in a tube for different values of Ca. The streamlines (in the relative reference frames moving with the droplets) are also shown in this figure for different values of Ca. The viscosity ratio, $\lambda = 0.1$.

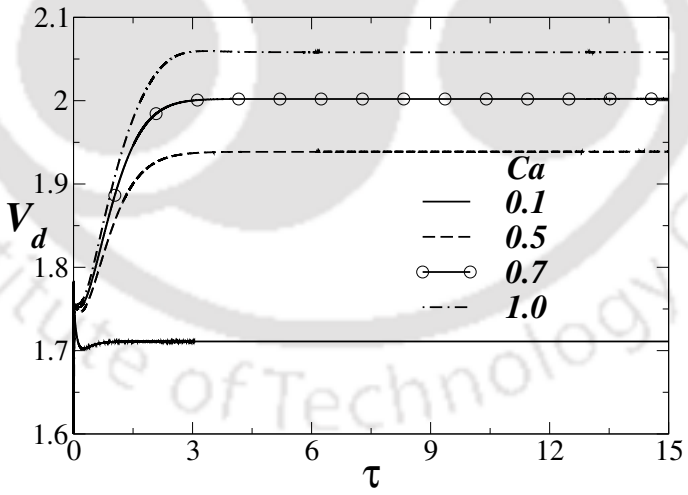

Figure 4.8: The temporal variation of droplet velocity, V_d as it is migrating inside the tube for different values of Ca. The other parameters are $a = 0.7$ and $\lambda = 0.1$.

4.7 also illustrates the streamlines inside the droplet signifying circulation within the droplet. The motion of the medium outside the droplet exists continuous with the

rotational motion inside the droplet. The liquid motion in the core of the droplet can be approximated by a Hill's spherical vortex [100]. If a Hill's vortex flow through a constricted passage, it experiences strain tending to make it oblate with major axis along the axis of symmetry.

The temporal variations of dimensionless velocity of the droplet, V_d are shown in Fig. 4.8 for Ca = 0.1, 0.5, 0.7 and 1. The parameter values considered are the same as those used to generate Fig. 4.7. It is seen that during the initial time ($\tau < 0.5$ approximately), a slight decrease in the droplet velocity is observed due to the onset of shape distortion, which increases the droplet resistance to the flow. After this initial phase, the droplet velocity, V_d gradually increases as the droplet attains a steady streamlined shape. Once a steady shape is obtained the drop continues to migrate in the axial direction with the same steady velocity (for $\tau > 3$ approximately, for this set of parameters). One interesting observation noted here is that at high Ca, the drop velocity exceeds the centerline velocity of the fluid, $2V$. This was also observed by Lac & Sherwood [101], where it was revealed that an elongated droplet with $\lambda < 0.5$ travels faster than $2V$, the maximum velocity of the imposed flow at the inlet of the tube.

4.3.1.3 Effect of viscosity ratio

In Figs. 4.9 (a), (b), (c) and (d), the effect of viscosity ratio is investigated on the dynamics of a droplet ($a = 0.7$) for different values of the capillary number. The variations of steady droplet velocity, V_d with λ in Fig. 4.9 (a) show that increasing viscosity ratio, λ decreases V_d for the range of the capillary numbers considered. It can also be observed that for a fixed value of λ, increasing Ca increases the steady droplet velocity, V_d. In Figs. 4.9 (b) and (c), the effect of λ and Ca is investigated on the droplet deformation by plotting the variations of dimensionless length l_d and width, w_d of the droplet with Ca for different values of λ. It can be seen that an increase in either Ca or λ (or both) causes the droplet to deform more in the axial direction, and hence its length (l_d) increases, while width (w_d) decreases. Fig. 4.9 (d) shows the effect of Ca and λ on the thickness of the continuous fluid film surrounding the drop. In accordance with the observation from Figs. 4.9 (b) and (c), it is obvious that the film thickness (f_t) would increase as the droplet gets elongated. Thus, as expected, we see in Fig. 4.9(d) that with the increase in either Ca or λ (or both) increases the film thickness f_t. The inspection of this figure also

reveals that the effect of viscosity ratio is independent of size of the droplet. Note that length and width of the droplet, and film thickness presented in Fig. 4.9 are non-dimensionalised with the radius, R_0 of the tube.

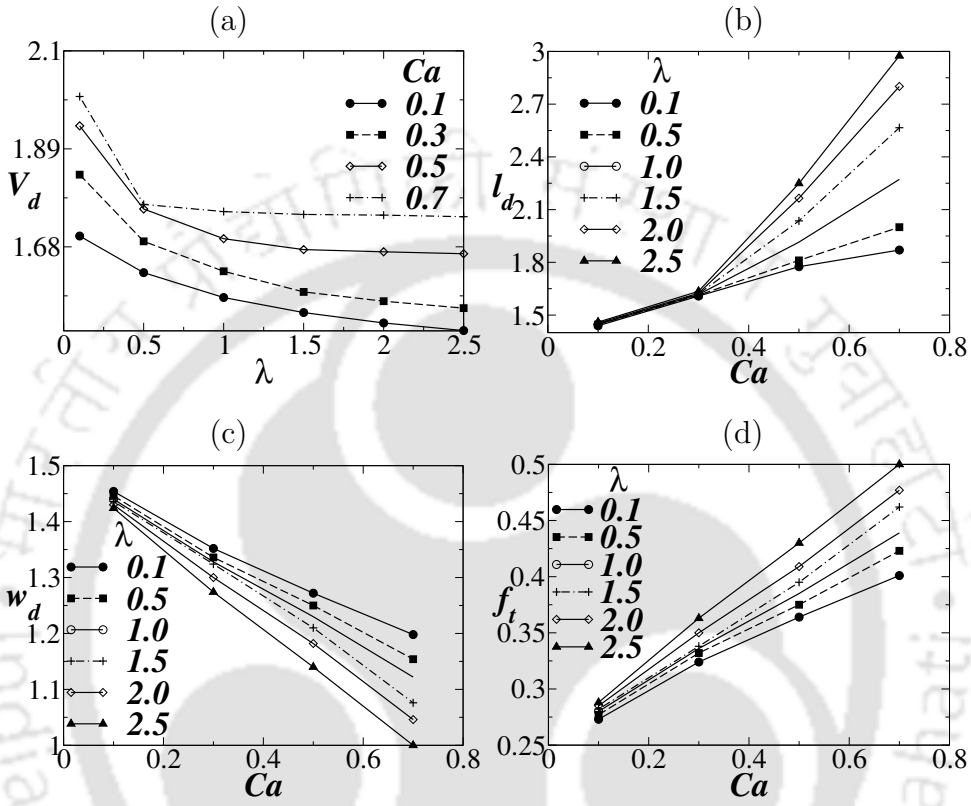

Figure 4.9: Variations of dimensionless (a) Droplet velocity, V_d with viscosity ratio, λ for different values of Ca, (b) Length of the droplet, l_d, (c) Width, w_d of the droplet, and (d) Film thickness, f_t with Ca for different values of the viscosity ratio, λ. The aspect ratio, a is fixed at 0.7.

4.3.2 Dynamics of disintegrating droplets

The breakup of a droplet into smaller droplets is brought about due to the instabilities. Unless a very high capillary number is considered, a small drop does not break into smaller droplets in a pressure-driven capillary tube. However, if the aspect ratio, a is large, the drop breaks into daughter droplets even at low capillary numbers. The particular the capillary number that causes a drop to break is termed here

as critical capillary number. The same terminology was also used in the previous studies [2, 96]. The value of the critical capillary number for a particular drop size is dependent on the viscosity ratio of the system. As observed in Fig. 4.7, for Ca = 1, a clearly visible indent is formed at the trailing edge of the droplet (for $a = 0.7$). Thus, we now study the effect of a on the splitting of the droplet for Ca = 1. Also we investigate on the effect of λ on drop breaking phenomenon for a fixed a and Ca.

4.3.2.1 Effect of droplet size for a system with $\lambda = 0.1$ and Ca = 1

The deformation of a droplet depends primarily on the size of the drop with respect to the tube radius, a. To understand the importance of the aspect ratio of a droplet on its deformation and breakup, we perform numerical simulations for $a = 0.7$, 0.8 and 0.9 in a flow system with $\lambda = 0.1$ and Ca = 1. These results are discussed next.

***Droplet dynamics for* a = 0.7**

For $a = 0.7$ (i.e for a relatively smaller droplet), the droplet shapes are plotted for different times in Fig. 4.10. It can be seen that the droplet undergoes large deformation during the initial phase ($\tau < 1$). It continues to deform till $\tau = 3$ for this set of parameter values. During this period, the shape of the droplet is adjusted due to the competition between the inertial and viscous forces, which are dominant at the leading and trailing edges, of the droplet respectively. In this case, as the droplet is small in size, the tube wall is sufficiently away from the edge of the drop and thus the viscous drag due to the wall effect is much smaller compared to the inertial force at the leading edge. At $\tau = 4$, we see that the drop attains a steady bullet like shape and there after it traverses in the tube maintaining the same steady shape.

***Droplet dynamics for* a = 0.8**

The dynamics of a droplet for $a = 0.8$ is investigated in Fig. 4.11 while keeping the rest of the parameters the same as those used for $a = 0.7$. The shape evolution of the droplet for $a = 0.8$ reveals some interesting phenomena. In this case, the droplet surface is closer to the pipe wall as compared to $a = 0.7$ case, which enhances the effect of the drag force. It is observed that the droplet continues its deformation (unsteady state) for a long time. At an early time ($\tau = 2$), the indent becomes very

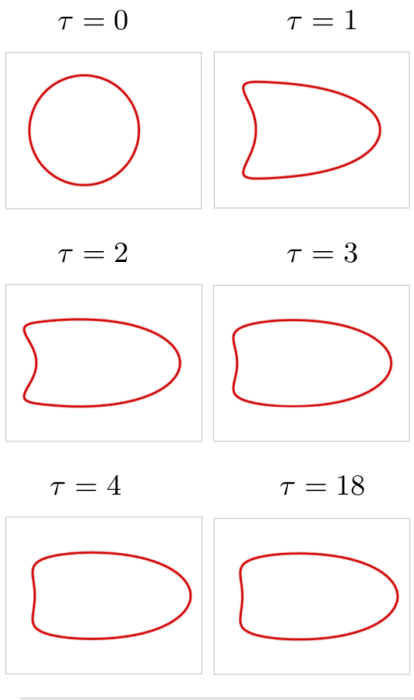

Figure 4.10: The shape evolution of a droplet for Ca = 1 and $\lambda = 0.1$. The aspect ratio $a = 0.7$.

prominent at the trailing edge of the droplet. At $t \geq 4$, it can be seen that the continuous fluid pushes its way through the drop forming a penetrating jet. Then, the droplet fluid forms a thin layer towards the leading edge and continues thinning while the tail part of the drop joins back, thus leaving a small part of the continuous fluid trapped in between them (see $\tau = 6$). The results at τ between 6 and 8 show how the leading part of the drop separates from the main droplet body. At $\tau = 7.25$, the position of the droplet is nicely captured showing the advancing front daughter droplet with two small satellite droplets followed by the large drop. At $\tau = 7.75$, an interesting phenomenon occurs, when the two small satellite droplets merge with the large drop. This merger happens due to the phenomenon of Ostwald ripening. From $\tau = 8$ to 10, the entire drop merges back and proceeds towards attaining a steady shape ($\tau = 15$). During the entire period ($\tau = 0 - 15$), the drop gradually tends to become more streamlined thus increasing the gap between the drop surface and the wall of the tube. Therefore, the drag force due to the tube wall effect decreases and inertial force at the leading edge increases gradually during this period.

***Droplet dynamics for* a = 0.9**

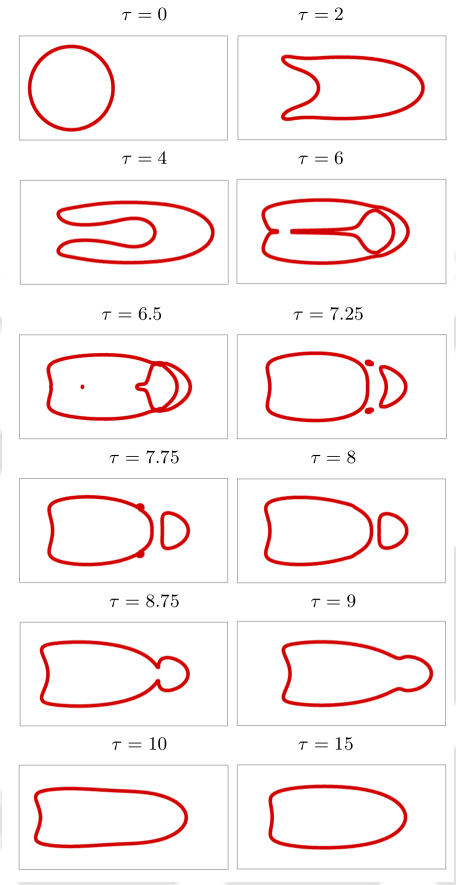

Figure 4.11: The shape evolution of a droplet for Ca = 1 and $\lambda = 0.1$. The aspect ratio $a = 0.8$.

The aspect ratio is increased to $a = 0.9$ and the dynamics of a droplet is investigated in Fig. 4.12 while keeping the rest of the parameters the same as those used for $a = 0.7$ and $a = 0.8$. This is an interesting case as the initial droplet radius is neither very small nor very large as compared to the radius of the tube. The main reason for the choice of this aspect ratio is that the asymptotic methods that yield results for very large or very small drops [2] cannot be applied for droplets whose size is comparable to the tube diameter. The shape evolution of a droplet for $a = 0.9$ is shown in Fig. 4.12. It can be seen that the deformation dynamics is different from that observed in the previous case ($a = 0.8$). In this case, the droplet is more elongated (see droplet shape at $\tau = 4$, 6 and 8). An obvious reason for this

elongation is the initial droplet size is bigger than the previous case. Another reason is that due to the close contact of the drop surface with the tube wall, the droplet experiences more drag. The trailing edge of the droplet is more elongated at the early times ($\tau = 1$ to 4) owing to the dominance of the drag force in the presence of the wall. After $t = 4$, the droplet undergoes thinning and then breaks up into daughter droplets and satellite drops ($\tau = 6$ to 8) in the same way as that in the earlier case ($a = 8$). From $\tau = 8$ to 11, the phenomenon of Ostwald ripening is very prominent. From $\tau = 11$ to 18, the drops eventually coalesce and merge back to form a single drop. It is observed that the situation at $\tau = 18$ (on the verge of leaving the domain) is quite similar to the situation at $\tau = 9$ in Fig. 4.11, hence it can be conjectured that for an extended domain the drop will gradually attain a steady shape.

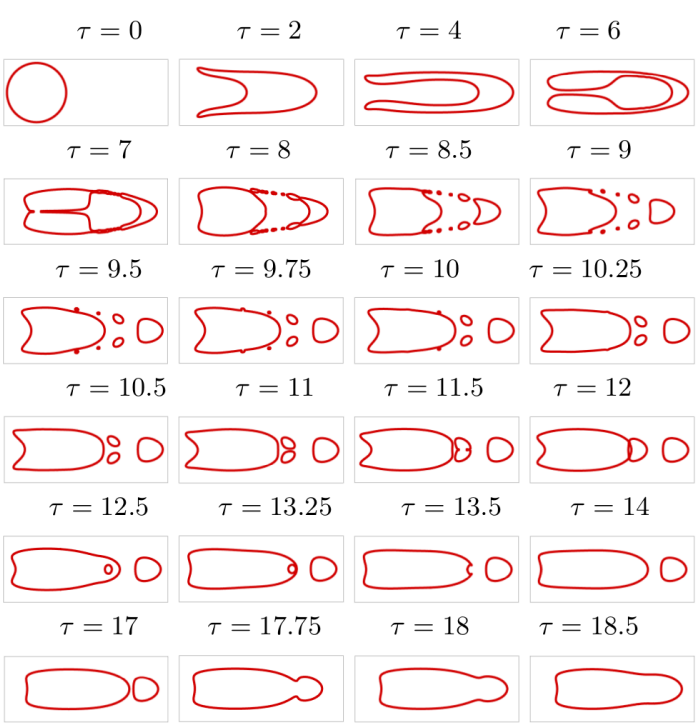

Figure 4.12: The shape evolution of a droplet for Ca = 1 and $\lambda = 0.1$. The aspect ratio $a = 0.9$.

4.3.2.2 Effect of viscosity ratio on the dynamics of breaking up droplets

From the results presented in Figs. 4.10, 4.11 and 4.12, we learnt that a drop with aspect ratio, $a = 0.9$ elongates more and forms several daughter droplets and satellite droplets at the intermediate times before merging back to a single drop. Thus, we consider a droplet of $a = 0.9$ and investigate the effect of viscosity ratio on droplet migration and breakup. We consider three viscosity ratios in this study, $\lambda = 10^{-3}$, 0.58 and 2.04 in Figs. 4.13, 4.14 and 4.15, respectively. Ca = 1 is taken for all the viscosity ratios. Inspection of Figs. 4.13, 4.14 and 4.15 reveals that increasing viscosity ratio, increases the tendency of droplet breakup into smaller droplets. The

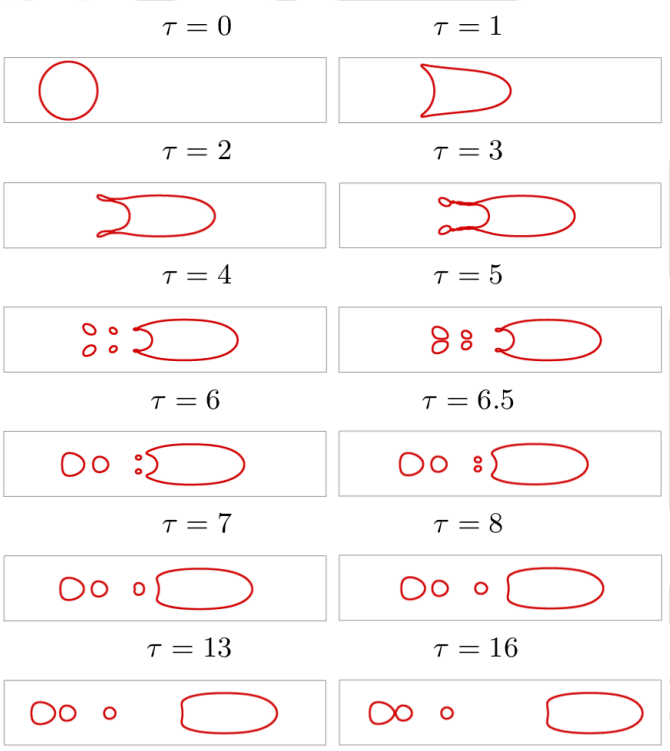

Figure 4.13: The shape evolution of a droplet for $\lambda = 10^{-3}$ and Ca = 1. The aspect ratio $a = 0.9$.

mechanisms of droplet break up and generation of smaller droplets are similar to the mechanisms of atomization that have been extensively researched. The mechanism of atomization typically consists of 3 steps: (1) formation of liquid sheets; (2) the liquid sheets undergo disintegration into drops and ligaments; (3) the ligaments further break up into finer droplets. Theoretical analyses of the atomization process

to predict droplet size have yielded models providing good agreements with the experimental data.

Fraser *et al.* [102] and Dombrowski and Johns [103] have described the process of liquid sheet atomization and the explanations have close resemblance to the processes that are observed in Figs. 4.13, 4.14 and 4.15. The difference is that, in our case, the liquid drop is being disintegrated in a liquid medium. Under this situation, the trailing edges of the deformed drop are gradually transformed into liquid sheets (clearly evident from Figs. 4.14 and 4.15). For the disturbances (sinuous or varicose), the sheets are assumed to fragment into pieces of lengths dictated by a dominant wave mode. These fragmented parts roll up under the influence of surface tension. The capillary force plays a major role and promotes the formation of cylindrical ligaments of various sizes. Subsequent breakup of these ligaments is brought about by the Rayleigh-Plateau instability mechanism culminating in the formation of droplets of smaller sizes.

The above mentioned explanation applies well to both low and high viscosity ratios. However, for higher viscosity ratios (say for $\lambda = 2.04$), the shear force on the ligament surfaces becomes relatively high in magnitude. In the face of counteracting interfacial tension, it elongates the ligaments more (τ =8) before the ligaments break-up into droplets (Fig. 4.15).

4.3.3 Critical capillary number, Ca_{cr}

Finally, in order to investigate the effects of viscosity ratio and the size of the drop on the critical value of Ca that leads to drop breakup, we run a number of computations for different systems by varying the viscosity ratio from 10^{-3} to 2.5. The critical capillary number (Ca) is calculated based on the drop size for each combination of the rest of the governing parameters. Table 4.1 depicts the value of the critical capillary number, Ca_{cr} obtained with respect to the aspect ratio (a) for different values of viscosity ratio, λ. From this study, we observe some physics related to drop breakup. When we focus column wise in Table 4.1, it is observed that for each value of λ, the critical capillary number decreases as the aspect ratio, a (which is equivalent to droplet size) increases. The reason for such behavior can be attributed to the fact that when the droplet is very small, its velocity is influenced more by the centerline velocity of the external flow, due to which it moves fast in the axial direction without experiencing much deformation. Also the drop being far from the

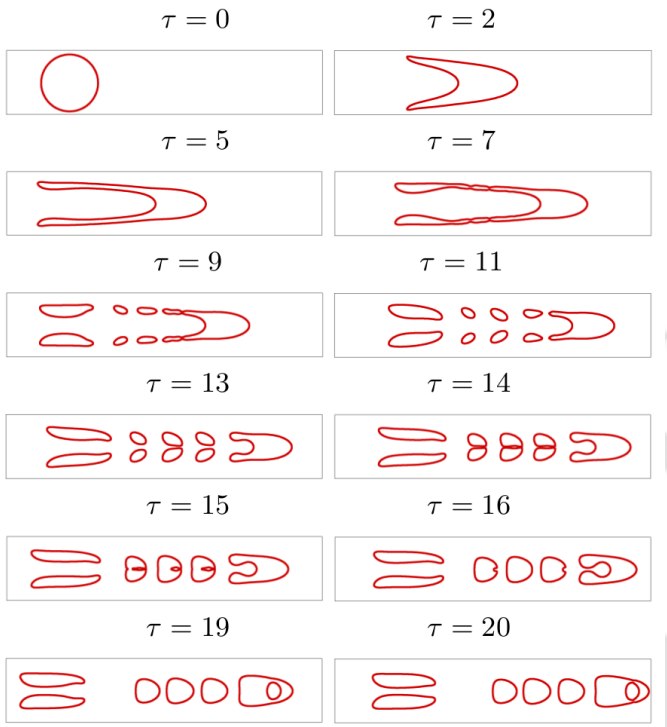

Figure 4.14: The shape evolution of a droplet for $\lambda = 0.58$ and Ca $= 1$. The aspect ratio $a = 0.9$.

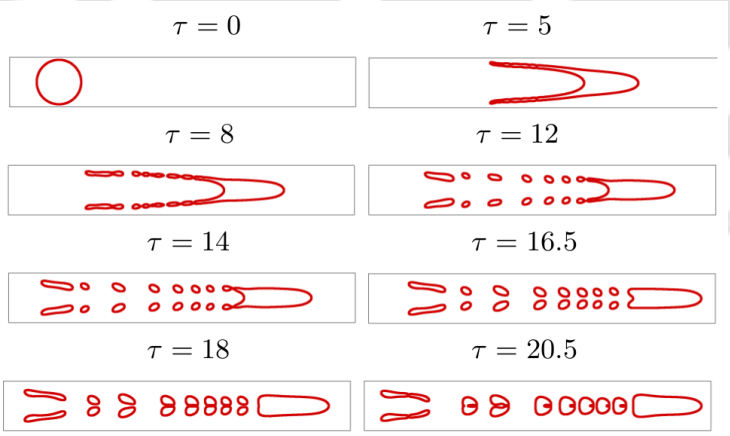

Figure 4.15: The shape evolution of a droplet for $\lambda = 2.04$ and Ca $= 1$. The aspect ratio $a = 0.9$.

wall, experiences a less resistance. Such small drops require high Ca (low surface tension) in order to undergo breakup. However, as the drop size keeps on increasing

Table 4.1: The critical capillary number for different values of aspect ratio, a and viscosity ratio λ.

λ / a	10^{-3}	10^{-2}	0.1	0.5	1	1.5	2	2.5
0.3	6.32	6.27	6.0	6.05	6.52	-	-	-
0.4	3.82	3.75	3.45	3.25	3.07	3.16	3.56	5.36
0.5	2.64	2.5	2.26	1.95	1.88	1.89	1.93	2.03
0.6	1.94	1.81	1.6	1.36	1.36	1.27	1.27	1.26
0.7	1.41	1.37	1.2	1.0	0.99	0.94	0.91	0.9
0.8	1.08	1.06	0.93	0.75	0.75	0.7	0.67	0.67
0.9	0.86	0.84	0.71	0.55	0.54	0.5	0.47	0.45

Ca_{cr} decreases, because the drop approaches the wall and the resistance to its flow increases. Row wise inspection of Table 4.1 (i.e. inspection of the variation of Ca_{cr}

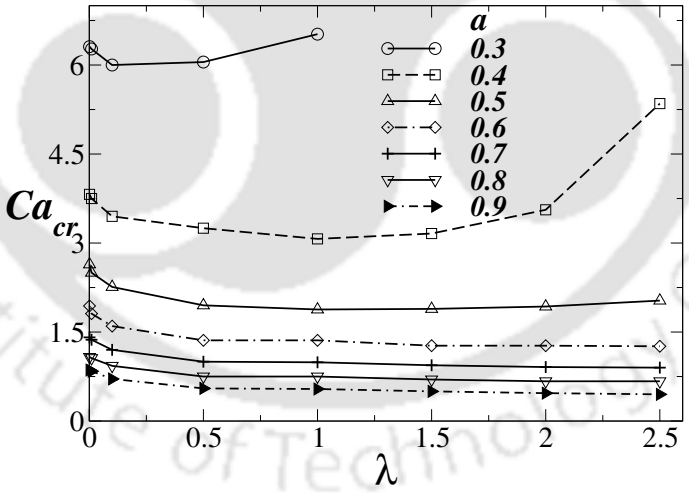

Figure 4.16: Variation of critical capillary number Ca_{cr} with viscosity ratio, λ for different values of a.

with λ for a fixed a) reveals that the value of critical capillary number, Ca_{cr} decreases (for most values of a considered) with the increase in viscosity ratio, λ for a fixed aspect ratio, a (i.e. drop size). This is because increasing λ increases the tendency of the droplet to deform more, and hence Ca_{cr} decreases. In Fig. 4.16. it can be

observed that while this phenomenon is true for droplets with $a > 0.5$, the same does not seem to be followed for smaller drops ($a < 0.5$). For smaller drops, an interesting phenomenon occurs. At first Ca_{cr} decreases as usual but this constant decrement pertains only to a certain range of λ. For $\lambda > 1$ (approximately), Ca_{cr} again increases. This behavior is very prominent for $a = 0.4$ as seen in the Table 4.1. This non-monotonic variation of Ca_{cr} is first noticed for $\lambda = 0.5$. It is to be noted here that, it is difficult to find Ca_{cr} for $\lambda > 1$, because under such a situation (of high capillary number and also high λ) the droplet continuously deforms and most portions of the drop behave as a thin film, which continuously tends to elongate without breaking up. In this study, we have restricted our computations upto $\mathrm{Ca} = 6.52$; thus the capillary number required for the breaking of a small drop ($a = 0.3$) beyond $\lambda = 1$ has not been computed.

4.4 Summary

Numerical simulations of a neutrally buoyant droplet migrating in a cylindrical tube in the creeping flow regime are conducted using an in-house code adopting CLSVOF method. The axisymmetric Navier-Stokes and continuity equations are solved to determine the dynamics of drop motion and deformation in a capillary tube with an imposed fully-developed flow at the inlet of the tube. Extensive validations of the numerical solver adapted are presented before proceeding with detailed investigation of the problem. Detailed parametric study is conducted by varying the ratio of droplet radius to the tube radius, capillary number and viscosity ratio between the droplet and the surrounding fluid injected at the inlet of the tube. Different modes of droplet breakup are observed depending on the prevailing dominance of viscous and surface tension forces. The critical value of the capillary number beyond which a drop breaks is determined for different drop sizes and viscosity ratios.

Chapter 5

Cross Stream Migration of Drops Suspended in Poiseuille Flow in the Presence of an Electric Field

The cross stream migration of a neutrally buoyant drop, suspended in another immiscible medium, has been studied. Both the dispersed phase (drop fluid) and the suspending medium are considered to be incompressible and a fully developed velocity profile of the external fluid is considered at the inlet of the two dimensional channel. In the absence of an electric field the important non dimensional parameters pertaining to such problems are; the viscosity ratio between the drop fluid and the suspending medium, the ratio of drop diameter to channel height and the capillary number. The presence of electric field introduces additional stresses at the drop interface and extensive computations are performed by solving electro-hydrodynamic equations coupled with VOF interface capturing technique. The effect of permittivity and conductivity ratio on drop migration reveal interesting phenomenon of oscillation and rotation along with translation in the channel.

The contents in this chapter have been published as Nath, B., Biswas, G., Dalal, A., and Sahu, K.C. (2018) 'Cross stream migration of drops suspended in Poiseuille flow in the presence of an electric field', *Physical Review E*, vol. **97**, pp. 063106 (available online, DOI: https://doi.org/10.1103/PhysRevE.97.063106).

5.1 Introduction

The motion of a liquid drop suspended in Poiseuille flow in another immiscible medium inside a microchannel is a fundamental problem that stands very important from physical, biological and engineering view point. The droplet motion and deformation in micro channels and capillary tubes has been studied by researchers since decades. The dynamics of droplet in hydrodynamics flows through channel or tube has been experimentally studied by Goldsmith and Mason [104], Olbritch [4], Ho and Leal [105] and Olbrtich and Kung [2], at low Reynolds number. Ho and Leal [105] investigated the effects of capillary number and viscosity ratio on droplet shapes. Olbricht & Kung [2] studied experimentally the motion of drops in a capillary tube for a large range of capillary numbers, drop sizes and viscosity ratios. They reported the effects of drop size and viscosity ratio on the critical capillary number above which the drop breakup occurs. In the Stokes flow limit, Chan and Leal [76] and Nadim and Stone [77] investigated the effects of the viscosity ratio and the capillary number Ca on the migration of droplets with diameter much smaller that channel height. In addition to the experimental and theoretical studies, most of the numerical investigations for simulating the behavior of a single gas bubble or drop in Poiseuille flow at zero Reynolds number (Stokes flow approximation) were carried out using boundary-integral method (BIM) [3, 6, 85, 87–89]. On the other hand, Mortazavi and Tryggvason [90] studied the deformation and lateral migration of two-dimensional drop in a flow channel at finite Reynolds number using the full Navier−Stokes equations with a finite-difference/front-tracking approach. Konda *et al.* [106] numerically studied migration of a droplet in a converging-diverging channel using a finite-volume approach and demonstrated droplet shape oscillations while it migrates inside the channel due to an imposed pressure-gradient. Nourbaksh and Mortazavi [107] reported the dependency of the drop migration on the viscosity ratio.

Several theoretical, numerical, and experimental studies have also been carried out those explore the effects of application of electric field to various fluid systems. The pioneering theoretical works of O'Konski & Thatcher [27], Garton & Krasucki [108] in 1950s and 1960s involved electrohydrostatic analyses on droplet deformation. It was assumed that the fluids are perfect dielectric and mainly accounted for the electric forces normal to the droplet interface. They found that the droplet always deforms into a prolate shape. Taylor [109] and Ajayi [110] proposed

the leaky dielectric model which could account for the electric stresses tangential to the interface and predicted the deformation of a droplet into a oblate shape, as observed in the experiments of Allen and Mason [111]. Tsukada *et al.* [112] and Feng & Scott [113] used finite element method to study the droplet deformation under the influence of uniform electric field using a leaky dielectric model. To study the interaction between a pair of droplets placed in a uniform electric field Baygents *et al.* [114] developed a boundary integral method and applied their formulation to both dielectric and leaky dielectric models. Berry *et al.* [115] simulated conducting drops in a non-conducting medium. Lac & Homsy [28] used a boundary integral method to study the deformation and break up of a droplet in a uniform electric field and obtained a phase diagram showing the variation of droplet shapes under the influence of different electrical properties. Fernandez *et al.* [116] incorporated finite-volume and front-tracking methods to study the behaviour of an emulsion of leaky dielectric droplets in an electric field generated by parallel plate electrodes. Fernandez [117] did a similar study to investigate the response of an emulsion of a leaky dielectric droplet in a shear flow by employing the same formulation. Hua *et al.* [118] also utilised a front-tracking/finite-volume method to solve the full Navier−Stokes equations and studied the motion of a droplet suspended in a viscous medium under the influence of an electric field. In their work, they considered three different electrical models: leaky dielectric model, perfect dielectric model and constant charge model. Zhang & Kwok [119] developed a lattice Boltzmann method employing dielectric theory to study the droplet behavior in a uniform electric field. Sato *et al.* [29] experimentally studied the deformation and break up of silicone droplets in the presence of electric field. Timung *et al.* [120] reported a noninvasive way to disintegrate a microdroplet into a string of further miniaturized ones under the influence of an external electrohydrodynamic field inside a microchannel.

The numerous studies discussed above constitute considerable progress towards the understanding of the effects of electric field on droplet motion and deformation in tubes and channels. However, in most of the previous studies, the dynamics was investigated by placing the droplet at the centreline of the channel/tube. The cross stream migration phenomenon of droplets at low Reynolds number in channels still seems to be less explored and needs more attention. The work discussed in previous chapter (Chapter 4) may also be placed in perspective and extended further. The presence of electric field also has a profound influence on the droplet migration. Therefore, in the present work, we focus on the dynamics of droplet migration and

deformation started from an initial off center position and investigate the effect of electric field on the cross stream migration phenomenon.

The remainder of the chapter is organised as follows: In Sec. 5.2, the formulation of the problem is discussed. The qualitative and quantitative validations are conducted to check the accuracy of the mathematical model. This leads to Sec. 5.3 where the results of our computations for a wide range of parameters are discussed. The results include the study of droplet migration in both the absence and presence of electric field. Finally, a short summary is given in Sec. 5.4.

5.2 Formulation

In this section, we introduce the mathematical model that is employed to study the droplet migration in a two-dimensional (2D) channel with and without the influence of electric field and also examine its accuracy in capturing the flow physics. Figure 5.1 shows a schematic illustration of the computational domain considered in the present study. The motion of an initially spherical droplet of radius R_0 is

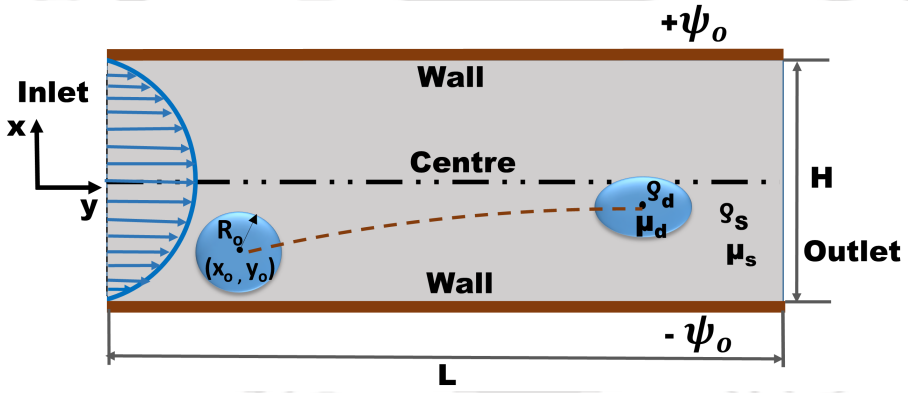

Figure 5.1: The schemtaic representaion (not to scale) of the lateral migration of a droplet inside a channel under the influence of external Poiseuille flow and uniform electric field.

placed at a position (x_0, y_0). The hydrodynamics are governed by the incompressible Navier- Stokes and continuity equations, along with an electro-hydrodynamic model to describe the electric field effects. The electromechanical coupling occurs at the interface that separates the droplet phase and the suspending fluid, since material and electrical properties are taken to be constant in each phase.

5.2.1 Numerical methods

The hydrodynamics are governed by the incompressible Navier-Stokes and continuity equations and an electro-hydrodynamic (EHD) model is used to describe the electric field effects. In order to track the interface, an advection equation for the volume fraction of the injected fluid, α is solved using the Volume-of-Fluid (VOF) approach. The detailed electro-hydrodynamic model adopted for the present study is described in Section.2.4. The aforesaid governing equations are solved using an open source code *Gerris* [58]. The salient features pertaining to *Gerris* are mentioned in Section 2.3 and described extensively in ref. [58, 59].

5.2.2 Initial and boundary conditions

The following initial and boundary conditions are implemented to solve the governing equations. Initially (at $t^* = 0$), both the fluids are considered to be at rest [121]. A fully-developed velocity profile is imposed at the inlet of the channel ($x = 0$), which is given by

$$u(x) = 1.5V_{avg}\left(1 - \frac{y^2}{(H/2)^2}\right), \quad \text{and} \quad v(x) = 0, \tag{5.1}$$

where, V_{avg} is the average velocity of the imposed flow. The no-slip and no-penetration conditions ($u = v = 0$) are imposed at the channel walls, i.e. $y = \pm H/2$. At the outlet of the channel ($x = L$), the Neumann boundary conditions for the velocity components and fixed pressure condition are applied. They are given by

$$\frac{\partial u}{\partial x} = \frac{\partial v}{\partial x} = 0, \quad \text{and} \quad p = p_0. \tag{5.2}$$

The external electric field is applied by imposing constant voltage boundary conditions $\psi = +\psi_o$ and $\psi = -\psi_o$ at the upper and lower walls of the channel, respectively.

5.2.3 Non-dimensionalisation

The results obtained from the numerical simulations are presented in terms of dimensionless parameters. The height of the channel, H, and average imposed velocity V_{avg} are used as the length and velocity scales, while μ_s is used as the viscosity scale. The aspect ratio, a^*, defined as the ratio of the initial droplet diameter to the height

of the channel, is given by $2R_0/H$. The chosen reference quantities give rise to the following set of dimensionless parameters

$$\begin{aligned} \text{Ca} &\equiv \frac{\mu_s V_{avg}}{\gamma},\ \text{Re} \equiv \frac{\rho_s V_{avg} H}{\mu_s},\ \lambda = \frac{\mu_d}{\mu_s}, \\ S &= \frac{\epsilon_d}{\epsilon_s},\ R = \frac{\sigma_d}{\sigma_s},\ E^* = \frac{E}{V_{avg}}\sqrt{\frac{\epsilon_o}{\rho_s}}. \end{aligned} \tag{5.3}$$

The parameters in Eq. (5.3) correspond to the capillary number, Reynolds number, viscosity, permittivity and conductivity ratios and a dimensionless electric field, respectively. Here E_c is the characteristic scale for electric field strength given as $E_c = V_{avg}\sqrt{\rho_s/\epsilon_o}$. The seemingly uncommon scaling for electric field is stimulated by the numerical work and is adopted so that the dimensionless parameter associated with the Maxwell stresses in Eq. (2.34) is unity. For the sake of convenience, E^* is represented as E for the rest of the paper and denotes the dimensionless electric field strength. In the present study, the Reynolds number is assumed to be small (Re = 1), i.e. the influence of inertia force can be assumed to be negligible compared to the viscous force. Furthermore, as we study the migration of a neutrally buoyant droplet in the simulations. The results are presented in terms of dimensionless time, $t^* \equiv tV_{avg}/H$. We also introduce a dimensionless term y_c, which represents the lateral position (area averaged center) of the droplet in the channel. The value of the y_c ranges between -0.5 to $+0.5$. The length of the channel is considered to be $L = 40H$.

5.2.4 Validation

5.2.4.1 Qualitative comparisons

For the purpose of validation, we compare our simulation results with the experimental results of Olbricht & Kung [2] for a drop of size $a^* = 0.95$ suspended in a system with $\lambda = 0.99$. Note that Olbricht & Kung [2] investigated the dynamics of droplet migration in a capillary tube, unlike in a two-dimensional channel as considered in the present study. Three different Ca are considered, *viz* $0.05, 0.10$ and 0.16. Figure 5.2 depicts that the present computational results possess a good qualitative match with their experimental counterpart.

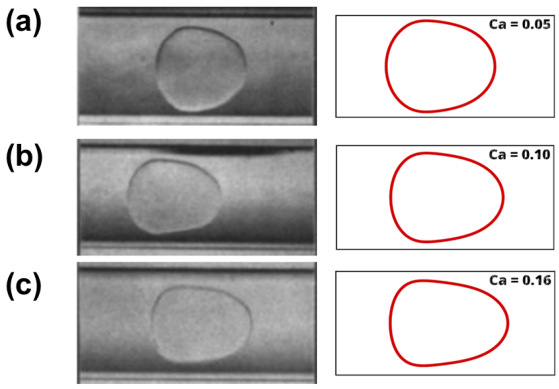

Figure 5.2: Comparison of drop shape for three different Ca: 0.05, 0.10 and 0.16. The other parameters are $a^* = 0.95$ and $\lambda = 0.99$. Left panel: Experimental results [2] and right panel: Present simulations.

5.2.4.2 Quantitative comparisons

To examine the accuracy of the present numerical solver for electro hydrodynamic simulations, the deformation of a spherical drop suspended in a stationary fluid is examined. The deformation is characterised by the Taylor's deformation parameter $D = \frac{L-B}{L+B}$, where L and B are the end-to-end length of the droplet measured along the x and y directions respectively. A positive D represents the deformation along the field direction (prolate shape), whereas a negative D represents the deformation perpendicular to the field direction (oblate shape); $D = 0$ represents a spherical droplet. The analytical solution for the drop deformation under electric field provided by Taylor [109] is given by

$$D = \frac{9\mathrm{Ca}_E}{8(2+R)^2}\left[R^2 + 1 - 2S + \frac{3}{5}(R-S)\frac{2+3\lambda}{1+\lambda}\right], \tag{5.4}$$

where, $\mathrm{Ca}_E = \frac{E^2\epsilon_o R_o}{\gamma}$ is defined as the electrical capillary number, which signifies the relative strength of the external electric field over capillary force. Figure 5.3 presents a quantitative comparison between the theoretical prediction of Eq. (5.4) and the results obtained from our current simulations. A good agreement can be observed for the deformation parameter D under varying conditions of Ca_E and R from Fig. 5.3(a) and (b), respectively.

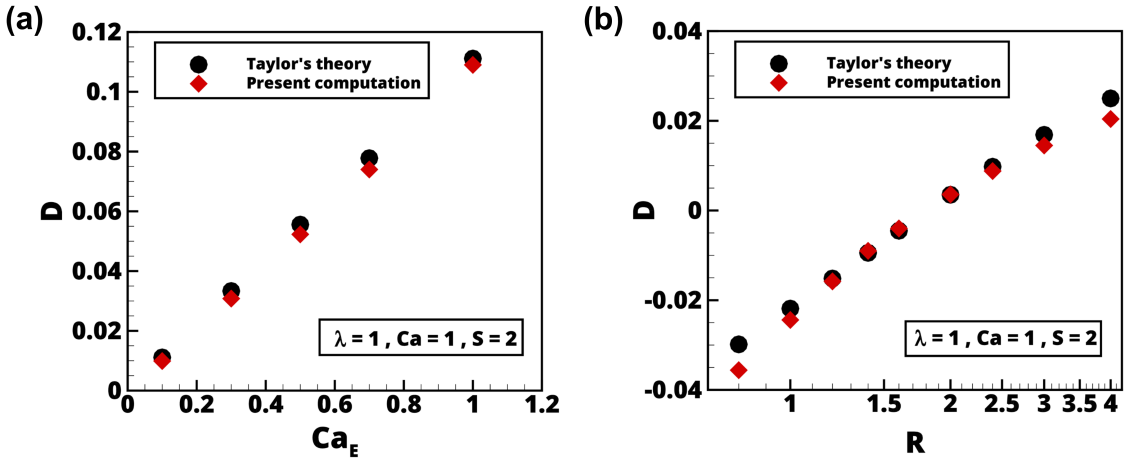

Figure 5.3: Comparison of drop deformation computed from the present simulations with Taylor's theory (Eq. 5.4) for varying Ca_E and R, respectively.

5.2.4.3 Grid independence test

The grid convergence test is conducted by simulating the migration of a droplet in a channel with aspect ratio $a^* = 0.6$. The rest of the dimensionless parameters are $\mathrm{Ca} = 0.7$ and $\lambda = 1.0$. The adaptive mesh refinement (AMR) feature of *Gerris* is employed to increase the grid density near the interfacial region while maintaining a relatively coarser mesh elsewhere. The refinement is done based on the gradient of volume fraction. Figure 5.4(a) presents snapshots of different levels of refinement deployed for the grid convergence test. The smallest (dimensionless) cell sizes are 0.031, 0.016, 0.008 and 0.004 corresponding to grid levels 5, 6, 7 and 8.

The temporal variations of the drop y_c for different grid refinement levels are presented in Fig. 5.4(b). It is observed that the drop y_c measured at $t^* = 15$ differs by $\sim 50\%$ between levels 5 and 6 and by $\sim 11\%$ between levels 6 and 7, whereas the difference between levels 7 and 8 is less than $\sim 3\%$. In view of this, and optimizing the computational time and cost without compromising the accuracy of the results, grids with refinement level 7 are used to generate the rest of the results presented in this study.

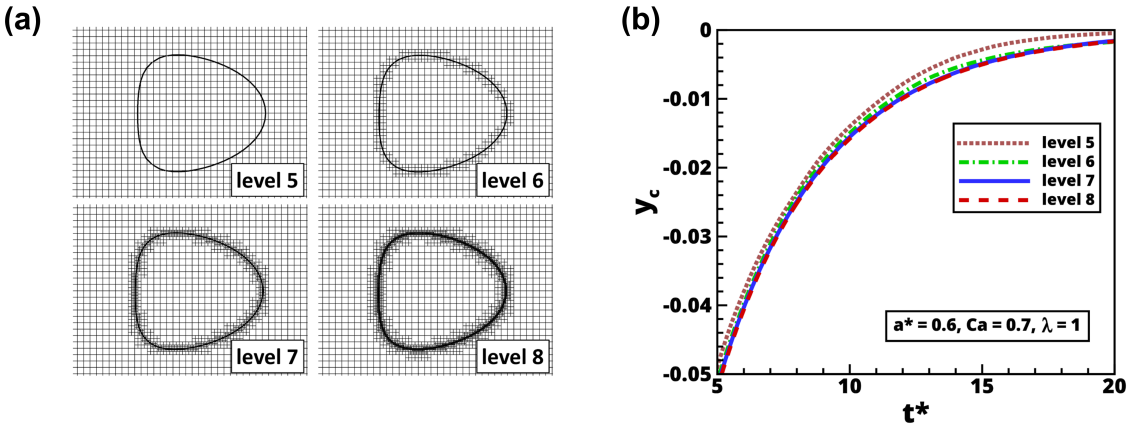

Figure 5.4: Grid convergence test. Panel (a): Snapshots of adaptive mesh generation using different levels of refinement. The refinement level of 7 is selected for the present study; and Panel (b): Comparison of y_c for different levels of grid refinement. The different parameters considered are $a^* = 0.6$, Ca $= 0.7$ and $\lambda = 1.0$.

5.2.5 Fluid properties

The drops can be considered to be composed of silicon oil and the suspending medium comprising of castor oil. Different grades of silicon oil help us to get different viscosity ratios required for the parametric studies [122]. For perfect dielectric fluids, silicon oil droplet in a medium of castor oil or vice versa can be considered depending on the permittivity ratio. For leaky dielectric fluids, two system of fluids are considered. System A represents a drop whose permittivity is lower but conductivity is higher than that of the suspending medium. System B represents a drop whose permittivity is higher but conductivity is lower than that of the suspending medium. Such fluid properties can be obtained by considering silicone oil drop in castor oil medium for system A and castor oil drop in silicone oil medium for system B [20]. The conductivity of silicone oils can be increased using doping in order to obtain a large range of conductivity ratio, R [20].

5.3 Results and discussion

The lateral migration phenomenon of drop inside a micro channel is studied both in the absence and presence of electric field and are discussed in the sub-sections

5.3.1 and 5.3.2, respectively. The cross stream locomotion of a drop placed off-center inside a channel for low Reynolds number flows can be attributed to the shape deformation of the drop under the influence of the incident flow and the variation of shear stress acting across the drop. The shape deformation leads to an aerodynamically favorable shape for the drop to move towards the centerline. The deformation is more prominent for larger sized drops which undergo larger shape deformation. A similar mechanism was thoroughly discussed in Karimi *et al.* [123] in the context of cell migration in microfluidics. Owing to the proximity of an off-center drop to the channel wall, the influence of shear force is significant and the variation of shear stress across the drop leads to the migration of the drop from the initially released position to an equilibrium position. Additionally, the rotation of the drop can result in the generation of Magnus lift force and the strength of this force is dependent on the angular velocity of the spinning droplet. The rotational effect has been found to be negligible for a significant portion of this study. However, the application of an external electric field under certain conditions may result in strong rotation of the drop as it traverses across the channel. The lift force generated by Magnus effect assumes significance in such flow conditions.

5.3.1 Drop dynamics under the influence of Poiseuille flow without electric field

The dynamics of drop deformation and lateral migration in the Poiseuille flow in a microchannel (in the absence of electric field) are dictated by the relevant non-dimensional parameters: drop size (a^*), capillary number (Ca) and viscosity ratio (λ). Therefore, the effect of each one of these parameters for a drop placed at an off center position is discussed in this subsection.

5.3.1.1 Effect of drop position

To understand the effect of the initial position of the drop on its migration phenomenon, a drop of moderate size ($a^* = 0.6$) was placed at different off-center positions along the y-axis. The capillary number and viscosity ratio were considered to be 0.7 and 1, respectively. Over a wide range of initial position of the drop, it is observed that the drop moves away from the channel walls and drifts towards the centerline and attains a steady bullet shape with the drop center lying in the channel

centerline. For the set of parameters, this phenomenon is observed to be consistent regardless of the initial off-center placement of the drop. Figure 5.5a shows the migration of the drop towards the channel centre from different off center positions. Although Mortazavi & Tryggvason [90] showed that the migration of a small drop towards or away from the wall depends on the viscosity ratio between the drop and medium, but for the moderate size drops suspended in systems with matching viscosities, the drops always tend to migrate towards the channel center. A similar dynamics was also observed by Griggs *et al.* [88] and Coulliette & Pozrikidis [87]. During its movement to the channel center, the drop undergoes shape deformations and finally attains a steady bullet like shape.

The streamlines in and around the drop placed at $y_c = 0, -0.1$ and -0.15 are

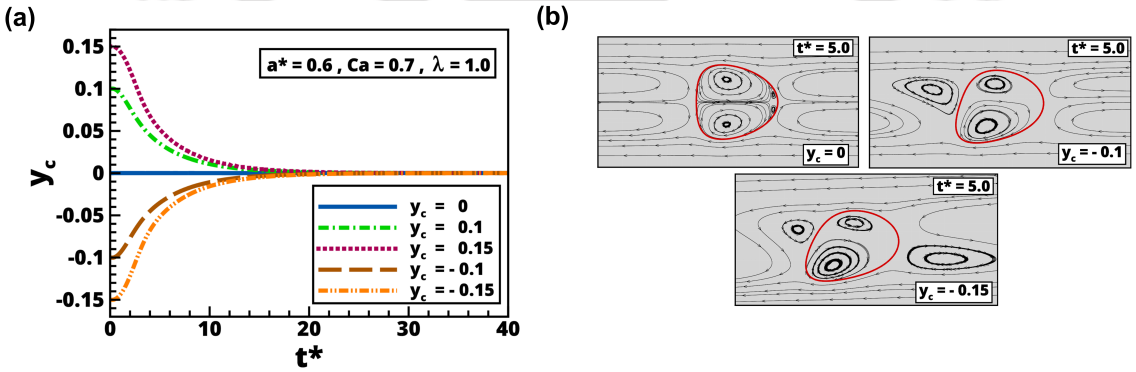

Figure 5.5: A drop ($a^* = 0.6$) initially placed at different off-centre positions gradually migrates towards the centreline of the channel. The other parameters are Ca = 0.7 and $\lambda = 1$. Panel (a): The lateral position of the drop versus time; and Panel (b): The streamlines around the drop placed at $y_c = 0, -0.1$ and -0.15, respectively. The flow field is presented in the frame of reference of the drop.

shown in Fig. 5.5(b). The images are taken at $t^* = 5$. At this particular time instant, the drop placed initially at the centerline ($y_c = 0$) has already reached a steady bullet like shape and moves with a steady velocity. However, the drops placed at off center positions have not attained a steady bullet shape, rather they are observed to be laterally migrating towards the channel centerline while traversing in the axial direction. It is clearly evident from Fig. 5.5(a) for the drop placed initially at $y_c = -0.15$ that the prominent vortices formed around the drop promotes the lateral deformation and pushes the drops to drift towards the channel centerline.

Though a little less pronounced but this phenomenon is also seen to be exhibited well by the drop placed initially at $y_c = -0.1$.

The confined flow inside a microchannel results in a sharp gradient of velocity across the channel cross-section and the shear force is stronger close to the walls. The initial migration rate (slope of y_c versus t^* in Fig. 5.5(a)) of a drop for initial $y_c = \pm 0.15$ is higher than that observed for initial $y_c = \pm 0.1$. This can be attributed to the larger shear variation experienced by such drops. As the drop approaches the centerline, the shear force acting on the drops decreases and the migration rate attains a smaller value for both values of y_c considered. Furthermore, the shear force on the drop can also be tuned by manipulating the drop size, the capillary number as well as the viscosity ratio, which can result in significant modification of the shape deforamtion as well as the shear force, thereby affecting the dynamics of the migration process. The influence of drop size, the capillary number and the viscosity ratio is discussed in the following sections.

5.3.1.2 Effect of drop size

The size of the drop plays a vital role in its migration phenomenon. To understand the effect of drop size, simulations are performed for drops of varying sizes in the range of $a^* = 0.3$ to 0.65. All the drops are released from an initial position that is below the centerline ($y^* = -0.15$) of the channel. The other parameters considered are Ca = 0.7 and $\lambda = 1$. The effect of size on the drop migration is shown in Fig. 5.6. For the range of drop sizes considered, and under the given set of conditions, it is observed that all the drops move away from the wall. The temporal variations of drop velocity are plotted in Fig. 5.6(a) for five different drop sizes ranging from $a^* = 0.3$ to 0.65. Figure 5.6(b) shows the variations of the corresponding lateral position of the drop with time. It is seen that the large drops have a higher tendency to migrate towards the channel centerline. For $a^* = 0.65$, the drop reaches the channel centerline and attains a steady shape and velocity. However, smaller drops do not seem to attain a steady lateral position within the length of the channel under consideration. A possible explanation of this is as follows: big drops are associated with enhanced shape deformation, which makes the drops aerodynamically favorable to move towards the centerline of the channel. In contrast, this aerodynamic deformation is absent in the case of small drops as they remain spherical due to the effect of larger surface tension force as compared to bigger drops. The smallest drop

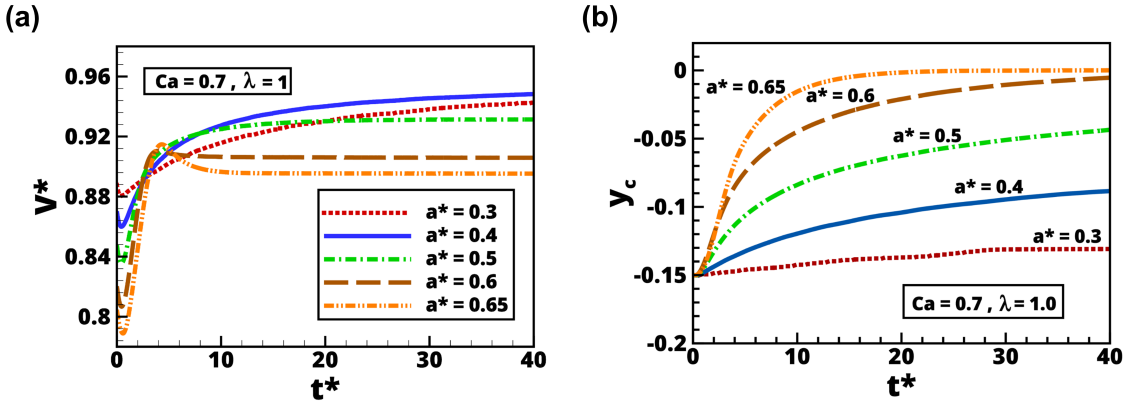

Figure 5.6: Migration of different sized droplets starting from an initial off center position ($y_c = -0.15$) towards the channel centreline. Panel a: Drop velocity versus time. Panel (b): Lateral position versus time. The other parameters are Ca = 0.5 and $\lambda = 1$.

$a^* = 0.3$ exhibits very less lateral migration and seems to settle down at a lateral position very close to the initial off center position. The intermediate drops $a^* = 0.4$ and 0.5 settle at a lateral position that is somewhere between the channel centerline and the initial off-center position. The varied dynamics exhibited by different sized drops can be explained as follows. As the droplet size increases, the equilibrium position of the drop moves closer to the centerline of the channel. The variation of shear stress acting across the drop increases with increasing size of the drop which leads to faster migration of a large drop towards the centerline in comparison to a smaller drop as depicted by Fig. 5.6. Thus, large drops deform more and advect away from the wall at a faster rate than smaller drops for a given pressure drop. It is also observed in Fig. 5.6(a) that the smaller drops move with a higher velocity in the channel as compared to the larger drops. For the length of the channel under consideration, drops with $a^* = 0.5, 0.6$ and 0.65 reach a steady velocity but the smaller drops of sizes $a^* = 0.3$ and 0.4 do not attain a steady velocity. Figure 5.6(b) reveals that for the given length of the channel ($L^* = 40$) the smaller drops ($a^* = 0.3, 0.4$) do not reach the center line of the channel while the larger drops reach the channel centerline quite early.

5.3.1.3 Effect of capillary number

The drop migration is influenced immensely by the capillary number. A higher value of capillary number is led by a lower surface tension force and dominating viscous force. Thus, with the increase in the capillary number, the ability of the drop to deform increases, which in turn leads to an enhanced rate of cross stream migration of the drop. This phenomenon is evident in Fig. 5.7 where the effect of Ca on

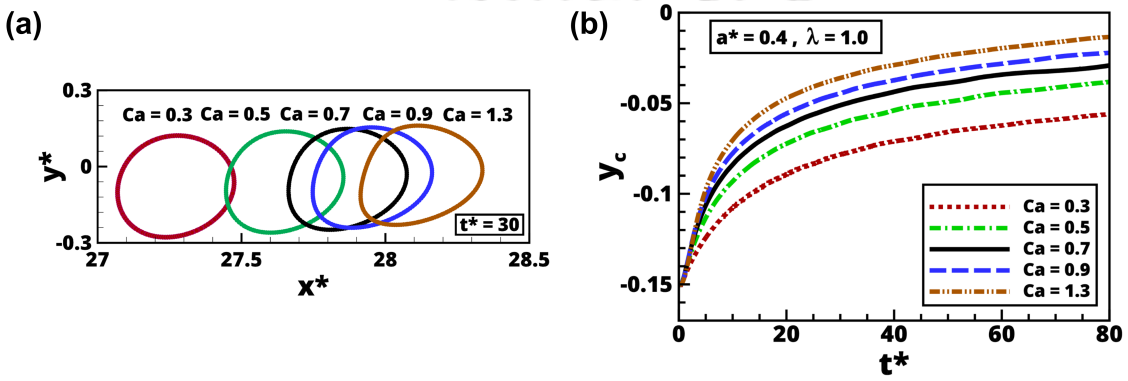

Figure 5.7: The effect of varying Ca (Ca = 0.3 to 1.3) on the migration of a drop initially placed at $y_c = -0.15$. Panel (a): Drop velocity versus time. Panel (b): Lateral position of the drop versus time. The other parameters are $a^* = 0.4$ and $\lambda = 1$.

drop migration is investigated for a drop of size $a^* = 0.4$. Ca is varied from 0.3 to 1.3 while the viscosity ratio is taken as 1. Figure 5.7(a) shows the drop shape and position at $t^* = 30$ for different values of Ca. It is seen that at the same time instant ($t^* = 30$) the drop occupies different positions and assumes different shape under the influence of varied Ca. It is evident from Fig. 5.7(a) that with the increase in Ca, the drop evolves from a nearly spherical shape to a more deformed shape with a lift in their lateral position.Even though we have used a channel length of $40H$ in all the investigations, Fig. 5.7 was especially investigated for a channel length of $80H$ over a longer duration ($t^* = 80$). Longer time simulations depict that the drops do not reach the centerline.

5.3.1.4 Effect of viscosity ratio

The viscosity ratio of the drop fluid to the suspending fluid also plays a vital role in drop migration. In this section, we examine the effect of viscosity ratio on the lateral migration of a drop of size $a^* = 0.4$. The value of Ca is taken as 0.7 and λ is varied from 0.01 to 2.0. Figure 5.8(a) depicts the influence of viscosity ratio on the velocity of the drop while traversing in the channel. It is observed that when Ca is fixed, with the increase in viscosity ratio, the velocity of the drop decreases owing to the increased hydrodynamic resistance. In Fig. 5.8(b), the temporal variations of the center position of the drop is plotted. It is observed that all the drops tend to migrate towards the channel centerline. Once a drop reaches the channel centerline, it moves with a steady velocity maintaining a bullet like shape. The deformation of the drop is dictated by the capillary number as well as the viscosity ratio and their dominance over each other decides the rate at which the drops migrate towards the channel centerline. As the viscosity ratio is increased, the lubricating effects between the wall and the drop are reduced. The drop fails to drift towards the channel centerline easily and tends to settle down in a lateral position that lies somewhere between the channel centerline and the initial off center position of the drop. As shown in Fig. 5.5(b), it is also clear that the migration towards the

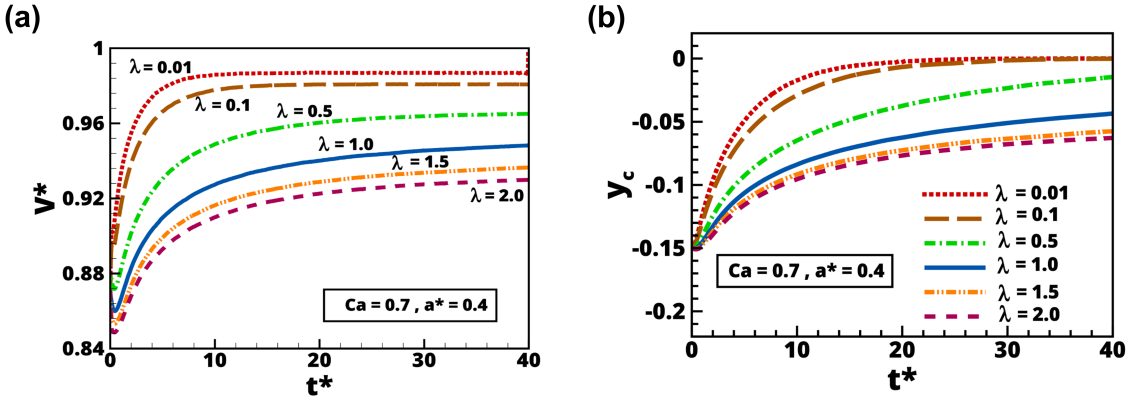

Figure 5.8: The effect of varying viscosity ratio ($\lambda = 0.01$ to 2.0) on the migration of a drop initially placed at $y_c = -0.15$. Panel (a): Drop velocity versus time. Panel (b): Lateral position of the drop versus time. The other parameters are $a^* = 0.4$ and Ca = 0.7.

centerline from different off-center positions are associated with asymmetrical shape

deformation of the droplet. For very low values of Ca, the drop does not deform much (tend to retain their spherical shape) due to the effect of high surface tension (Fig. 5.7). Thus the lateral migration of the droplet can be suppressed for small values of Ca (in the surface tension dominated regime). It is also observed that the drops of small size undergo less deformation (Fig. 5.6). For fixed values of other parameters, increasing the viscosity ratio, λ would again have a similar effect as that of increasing surface tension (Fig. 5.8). Therefore, intuitively we can conclude that the lateral migration of a moderate sized droplet decreases with decreasing Ca and increasing λ.

5.3.2 Drop dynamics under the influence of Poiseuille flow with electric field

As mentioned earlier in Section 2.4, the presence of electric field introduces an additional stress at the interface, termed as the Maxwell stress. The interfacial force may aid or oppose the surface tension force depending upon the sign of radius of curvature of the interface. The shape of the drop is influenced by the resultant effect of surface tension, Maxwell stress and viscous stresses. In this sub-section, we consider perfect dielectrics, where free charge carriers do not exist and electric stresses act normal to the interface. Also, we consider leaky dielectrics (poor conductors) that support accumulation of interfacial charges implying the presence of tangential stresses. The deformation and migration of the droplet in the presence of electric field are significantly affected by the electric properties of the fluid, namely, permittivity, resistivity and conductivity.

5.3.2.1 Dielectric fluids - Effect of permittivity ratio

The effect of permittivity ratio on the lateral migration of a drop ($a^* = 0.4$) is studied by varying the permittivity ratio (S) of the dispersed fluid to continuous fluid between 0.2 and 5.0. The other parameters are fixed at Ca = 0.7, $\lambda = 1$ and the electric field strength, $E = 5$. Figure 5.9(a) shows the shapes attained by the drop for different permittivity ratio at $t^* = 30$. It is clearly seen that as the permittivity ratio increases, the shape of the drop changes significantly. At high permittivity ratio, the drop takes a convex shape at the front and a concave shape at the back. This is because, the higher dielectric permittivity of the drop fluid as

compared to the suspending medium leads to the accumulation of a large number of induced bound charges across the interface, which generates the electro-hydrodynamic (EHD) stress to elongate the droplet towards the electrodes and form the plug inside the channel. Figure 5.9(b) shows that with the increase in permittivity ratio the lateral migration of the drop increases quite monotonically. However, it is also observed that as the permittivity ratio is increased, beyond $S = 3$, the drop overshoots the equilibrium position and oscillates several times around the mean position. These oscillations are more pronounced for $S = 5$ where the oscillations gradually dampen. However, the oscillations do not die down completely within the channel-length of interest. In Fig. 5.9(a), it can be seen that highly deformed droplet shapes are formed for $S = 4.0$ and 5.0, and these critical shapes lead to oscillations of the drops around its equilibrium position. The normalized pressure drop over the channel is shown in Fig. 5.10(a) for $S = 0.2$ to 5.0 at $t^* = 30$. The dashed line in Fig. 5.10(a) represents the normalized pressure drop in the channel in the absence of any drop. It is observed that as the drop undergoes elongation and gradually occupies the entire cross-section of the channel, the pressure drop inside the channel increases. The streamlines in and around the drop are plotted for the two extreme cases, namely for $S = 0.2$ and 5.0, as shown in Fig. 5.10(b). For higher value of S, the deformation of the drop leads to lobe - like shape yielding higher blockage ratio. The streamlines described by the channel fluid reveal a typical situation corresponding to flow past a bluff body inside a channel. The near wake region broadens with the increase in blockage ratio. The reason behind the drop oscillations about the mean position observed in Fig. 5.9(b) for $S = 4$ and 5 can be better explained by analysing Fig. 5.11, which illustrates the evolution of a liquid lobe. In Fig. 5.11, the motion of a drop of $a^* = 0.4$ is shown for $t^* = 0$ to 5.2 when subjected to $E = 5$ and $S = 5$. It is observed that the drop stretches and takes a bow shape rapidly as it starts moving in the channel. But the drop during its motion inside the channel hits the top and bottom wall surfaces, alternatively (as shown by the red arrow). Thus the phenomenon of oscillations of the drop mean position (as witnessed in Fig. 5.9(b) for $S = 5$) is exhibited because, when the drop hits a wall, an opposite and equal force is exerted by the wall on the drop which makes it move away from that surface laterally while it is still in axial motion. As the drop continues to rebound after hitting the wall, it gradually travels across the channel and hits the opposite wall and this event continues. The oscillations of drop mean position is higher at the beginning (as observed in Fig. 5.9(b) for $S = 5$) due to the

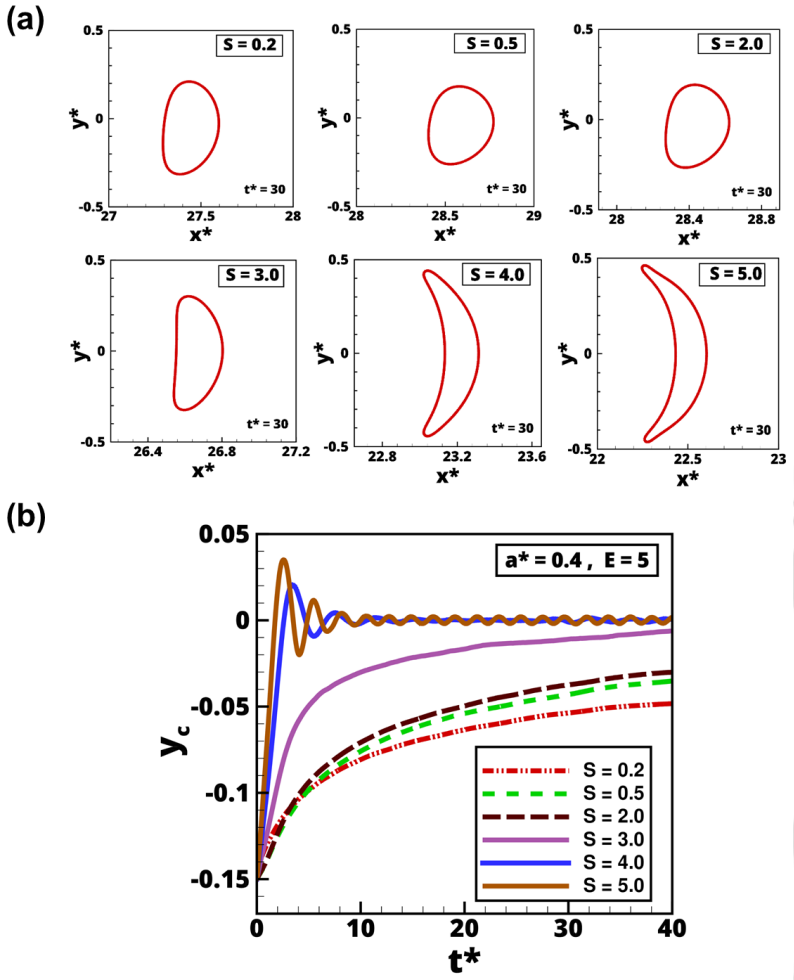

Figure 5.9: Effect of varying permittivity ratio ($S = 0.2$ to 5) on the deformation and migration of a drop initially placed at $y_c = -0.15$. Panel (a): The shape of a drop at $t^* = 30$ subjected to different permittivity ratio S. Panel (b): The lateral position of the drop versus time. Other parameters are $a^* = 0.4$, Ca $= 0.7$, $\lambda = 1$ and $E = 5$.

instability caused by the onset of drop deformation; however as the drop gradually takes a steady shape, the oscillation is found to be varying about a mean position $y_c = 0$ (centerline).

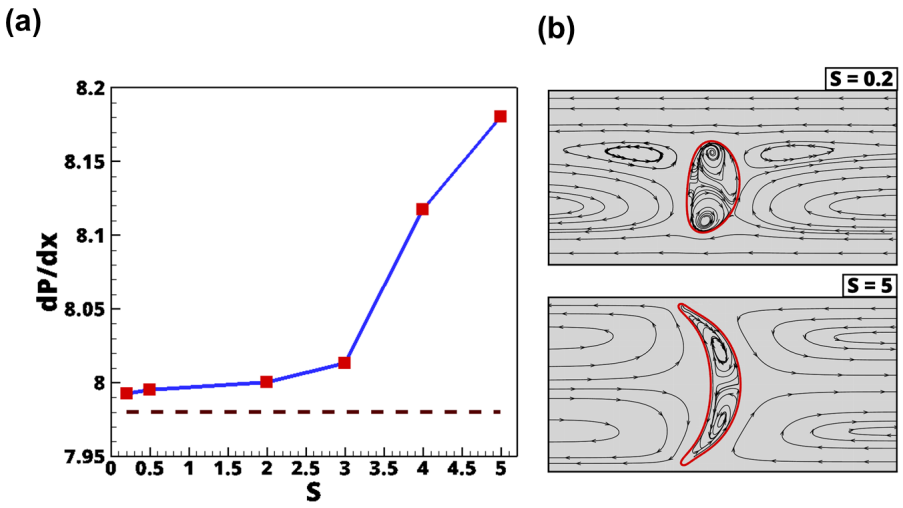

Figure 5.10: Effect of elongation of the drop. Panel (a): The normalized pressure drop in the channel for different permittivity ratio compared to the pressure drop in the channel in the absence of any drop (dashed line) and Panel (b): The stream lines around a drop subjected to varying permittivity ratio ($S = 0.2$ and 5) at $t^* = 30$. The flow field is presented in the frame of reference of the drop. Other parameters are $a^* = 0.4$, Ca $= 0.7$, $\lambda = 1$ and $E = 5$.

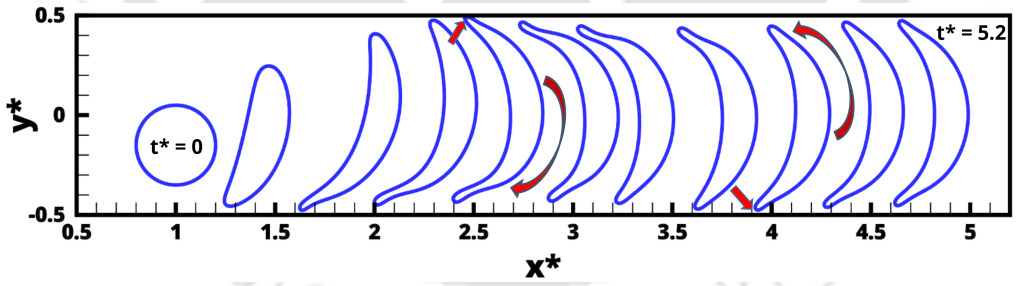

Figure 5.11: Variations of shape a drop ($a^* = 0.4$) initially placed at $y_c = -0.15$ inside the channel and subjected to electric field from $t^* = 0$ to 5.2. The other parameters are Ca $= 0.7$, $\lambda = 1$, $E = 5$ and $S = 5$.

5.3.2.2 Dielectric fluids - Effect of electric field strength

To understand the effect of electric field strength E on the migration of a given drop ($a^* = 0.4$), E is varied from 5 to 20. Figure 5.12(a) depicts the influence of E on the shape of the drop. The images show the deformed shape of the drop at a particular

time instant $t^* = 30$. The steady shapes obtained by the drop subjected to different E clearly reveal that with the increase in E, the drops get highly stretched and elongated in the direction of electric field. Figure 5.12(b) shows the lateral position of the drop while moving inside the channel subjected to varied E. It is observed

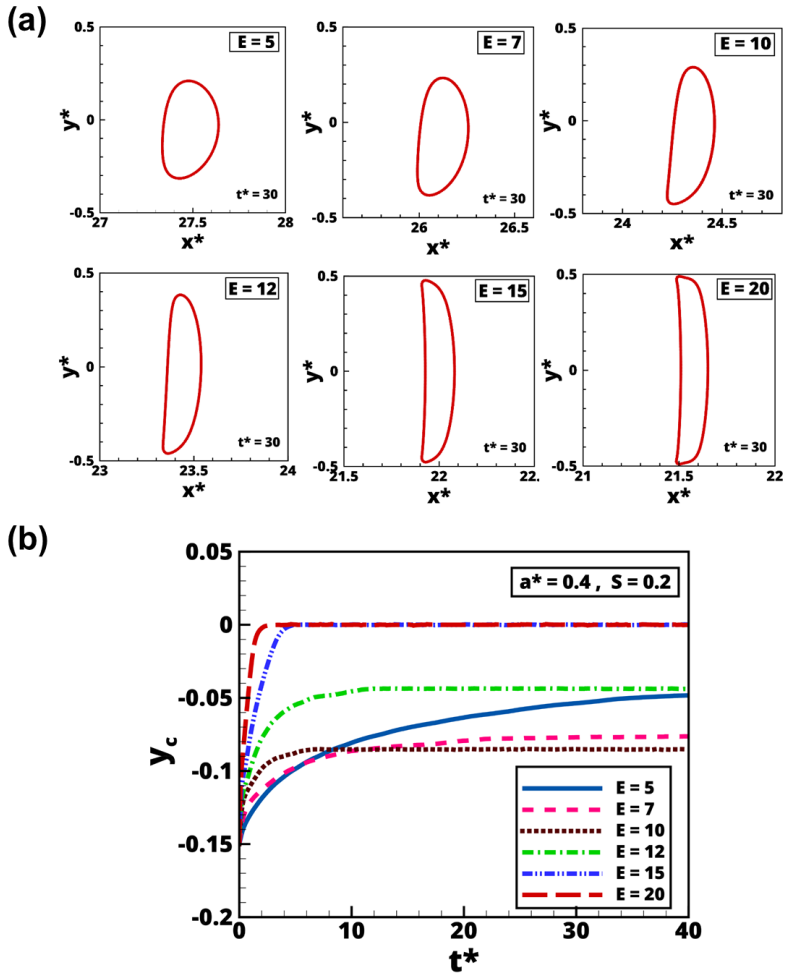

Figure 5.12: Effect of varying electric field strength ($E = 5$ to 20) on the deformation and migration of a drop initially placed at $y_c = -0.15$. Panel (a): The shape of a drop at $t^* = 30$ subjected to different E. Panel (b): The lateral position of the drop versus time. Other parameters are $a^* = 0.4$, Ca $= 0.7$, $\lambda = 1$ and $S = 0.2$.

that, for all other parameters remaining fixed, a drop under the influence of high value of E ($E = 15$ and 20) drifts faster towards the channel centerline and attains a steady velocity and hence a steady lateral position. While for intermediate values

of E ($E = 10$ and 12) the drop attains a steady lateral position somewhere between the initial off-center position and the channel centerline. This trend is seemingly followed by the drop subjected to $E = 7$ somewhere downstream. On the other hand, drop subjected to a lower value of E ($E = 5$) does not reach a steady lateral position for the channel length of interest and it is evident that it exhibits quite less cross stream migration. For $E > 10$, due to large elongation in the direction of electric field (drop tends to completely occupy the channel), the drop becomes symmetrical about $y^* = 0$ axis. Thus the center of gravity of the drop moves to the centerline of the channel. On the other hand, there is a combined influence of asymmetrical shape deformation and the electric field for $E < 10$, which results in an unsteady state till later times and prevents the drop to move to the centerline. For this set of parameters, this transition is occurring for $E = 10$, thereby resulting in a non-monotonic trend around $E = 10$. The normalized pressure drop over the

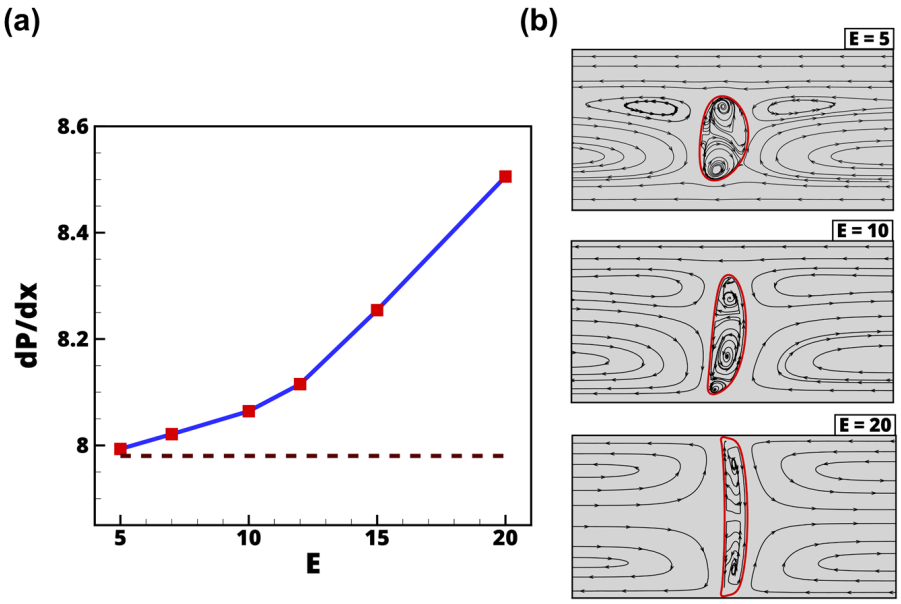

Figure 5.13: Effect of elongation of the drop. Panel (a): The normalized pressure drop in the channel for different electric field strength compared to the pressure drop in the channel in the absence of any drop (dashed line) and Panel (b): The stream lines around a drop subjected to varying permittivity ratio ($S = 0.2$ and 5) at $t^* = 30$. The flow field is presented in the frame of reference of the drop. Other parameters are $a^* = 0.4$, Ca $= 0.7$, $\lambda = 1$ and $E = 5$.

channel is shown in Fig. 5.13(a) for $E = 5$ to 20 at $t^* = 30$. The dashed line in Fig. 5.13(a) represents the normalized pressure drop in the channel in the absence of any drop. It is seen that as the drop gets more and more stretched in the presence of high electric field strength, the pressure drop inside the channel increases. The streamlines in and around the drop are plotted for $E = 5, 10$ and 20, as shown in Fig. 5.13(b). In case of $E = 20$, the stretched drop assumes almost the shape of a vertical elongated body occupying more than 98 percentage of the flow area. Immediate downstream is fully occupied by the separated symmetrical eddies. The approach flow streamlines resemble the stream lines of stagnation flow.

5.3.2.3 Leaky dielectric fluids

To study the effect of conductivity ratio R together with permittivity ratio S and electric field strength E and to understand the result of their dominance over each other on the droplet migration, we consider the fluids to be leaky dielectric. Two different systems are considered, namely, system A in which the drop fluid is more conducting than medium fluid, while permittivity of medium fluid is higher than drop fluid ($S = 0.5$ and $R = 2$); system B has the exactly opposite combination ($S = 2$ and $R = 0.5$). E is varied from 1 to 5. Figures 5.14(a) and 5.14(b) show the shapes of the more conducting and less conducting drops, respectively at $t^* = 30$ for varying E.

In Fig. 5.15, it is seen that in system A ($S = 0.5$ and $R = 2$), the drop migrates nearly monotonically towards the channel centerline (shown by the dotted lines). As E increases from 1 to 5, the drop attains a steady lateral position faster. However, for system B ($S = 2$ and $R = 0.5$), Fig. 5.15 (solid lines) reveals that the drop does not reach the channel centerline but settles at a lateral position close to its initial position. It is also observed in case of system B that with the increase in E from 1 to 3, the drop moves along a steady y_c. However, with further increase in electric field strength $E = 4$ and 5), it is seen that the lateral position of the drop oscillates around a mean value for some time. These oscillations are depicted because the drop along with translational motion now also exhibits rotational motion. This phenomenon is more pronounced for $E = 5$ as compared to $E = 4$. The oscillations gradually dampens with time, in both the cases.

Taylor provided the analytical solution for drop deformation under an electric field as given in Eq. (5.4) and it is observed that for $R < S$, the deformation is

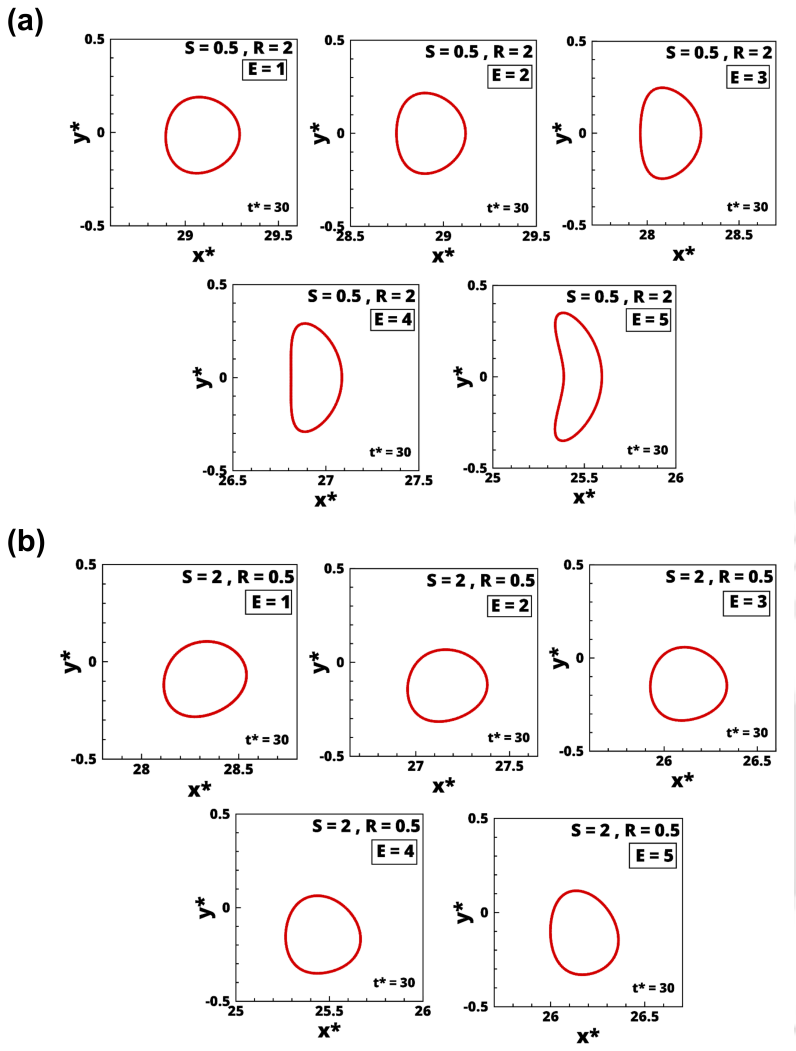

Figure 5.14: Shapes of the drop at $t^* = 30$ while migrating from an initial off center position of $y_c = -0.15$ and subjected to different permittivity ratio S, conductivity ratio R and electric field strength E. Panel (a): Drops suspended in a system of $S = 0.5$ and $R = 2$ and subjected to varying E. Panel (b): Drops suspended in a system of $S = 2$ and $R = 0.5$ and subjected to varying E. E is varied in the range of 1 to 5. Other parameters are $a^* = 0.4$, Ca $= 0.7$ and $\lambda = 1$.

negative, i.e. the drop attains an oblate shape. However, for $R > S$, $D > 0$ and drop becomes prolate. Thus, the relative magnitudes of R and S play the dominant role in deciding the drop deformation, behavior and the migration dynamics.

The influence of R and S on the migration characteristic of the drop is amply

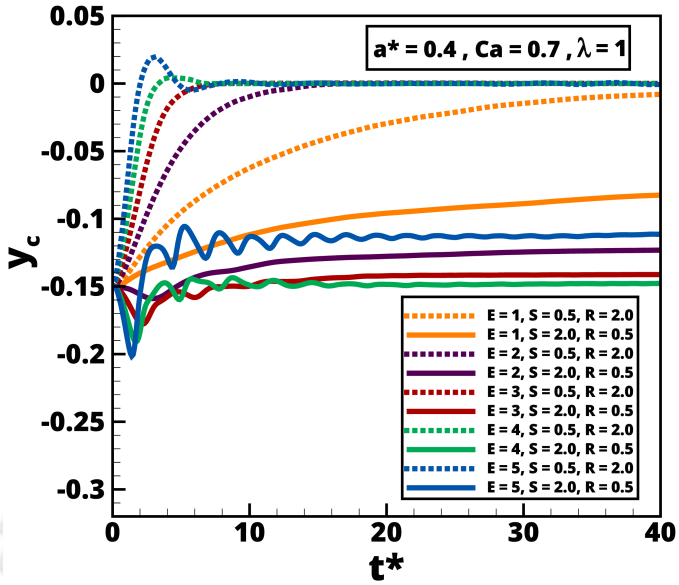

Figure 5.15: The migration of a drop initially placed at $y_c = -0.15$ towards the centreline of the channel influenced by different electric field strength E, permittivity ratio S and conductivity ratio R. Dotted and solid lines represent the position of the drop suspended in system A and B, respectively. Other parameters are $a^* = 0.4$, Ca $= 0.7$ and $\lambda = 1$.

demonstrated in Fig. 5.16(a) and (b) for a drop ($a^* = 4$) migrating under the influence of $E = 5$ suspended in system A and B, respectively. The transient evolution of the drop suspended in both the systems is shown from $t^* = 0.6$ to 20. Snapshot at $t^* = 0.6$ for system A ($R > S$) as shown in Fig. 5.16(a) clearly depicts the prolate deformation whereas for the same time instant the deformation is oblate for system B ($R < S$) as observed in Fig. 5.16(b). The electric force acting on the two sides of the drop is different in case of a non-rotating and a rotating droplet. Figure 5.17 shows the charge density at the interface of a migrating drop suspended in system A and B, respectively at different time instants under the influence of E = 5. The upper electrode of the channel is at a positive potential of $+\psi_o$ whereas the lower electrode is at a negative potential of $-\psi_o$. The plots in Fig. 5.17(a) demonstrates that the charge accumulation in system A is opposite to the direction of the applied electric field. The charge accumulated at the top of the drop for system A is negative whereas at the lower portion of the drop, positive charge accumulates. The opposite nature of charge between the electrodes and the drop interface results in a

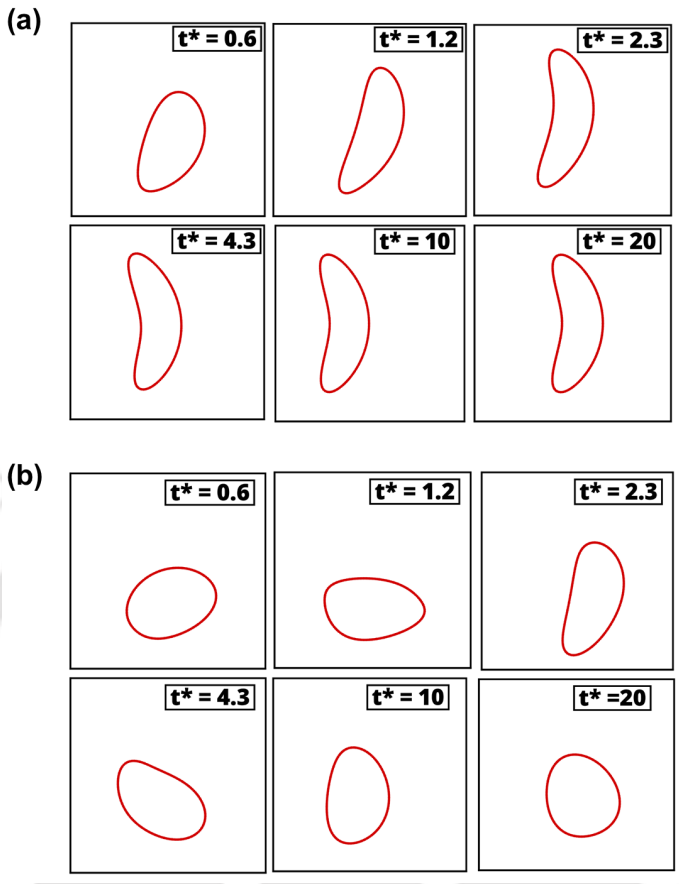

Figure 5.16: The transient evolution of a drop ($a^* = 0.4$) initially placed at $y_c = -0.15$ inside the channel. Panel (a): for system A and Panel (b): for system B. The other parameters are Ca $= 0.7$, $\lambda = 1$, $E = 5$.

pulling force on the drop which leads to an equilibrium position at the centerline. However, the charge accumulation for system B, shown in Fig. 5.17(b), is different from system A with positive charge at the top and negative charge at the bottom of the drop interface (as can be seen for $t^* = 1.2$). This results in a compressive force on the drop and leads to an off-center equilibrium position. It is to be noted that the drop placed off-center migrates towards an equilibrium position as discussed in Sec. 5.3.1.1 and the prolate deformation (system A) assists the migration of the drop towards the center of the channel. The deformation is further enhanced at higher field strength thereby further accelerating the migration rate as clearly evident in Fig. 5.15 for the dotted lines. In contrast, for system B, the drop deforms in the oblate direction and the oblate shape being hydrodynamically unfavourable under-

goes a series of rotations to attain a favourable shape at steady state. As observed from the solid lines in Fig. 5.15, this phenomenon of rotation is more pronounced under the influence high E.

Another reason for the rotational motion is that the drops having higher per-

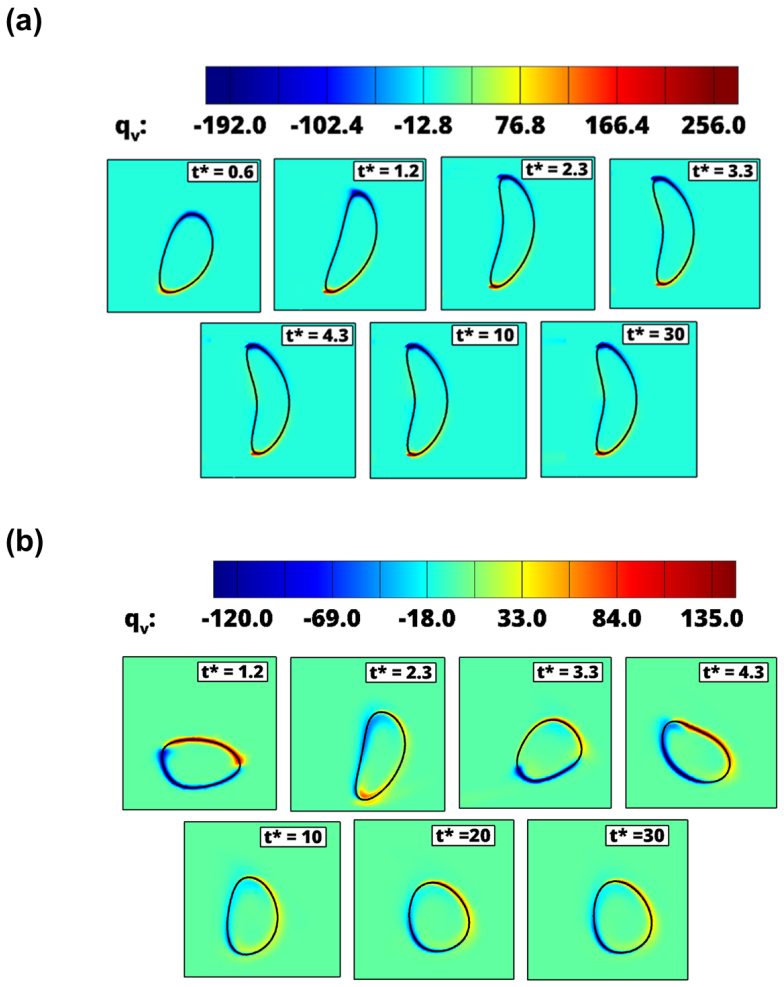

Figure 5.17: The charge density at the interface of a drop ($a^* = 0.4$) initially placed at $y_c = -0.15$ inside the channel subjected to electric field. Panel (a): Charge distribution at the interface of a non rotating drop suspended in system A and Panel (b): Charge distribution at the interface of a rotating drop suspended in system B. The other parameters are Ca $= 0.7$, $\lambda = 1$, $E = 5$, $S = 2$ and $R = 0.5$.

mittivity ratio and lower conductivity ratio (system B) when subjected to a high electric field ($E = 4$ or 5), deform initially in the direction of the field. This results

in a slight decrease in the magnitude of y_c during the early stages of migration as can be seen for $t^* \leq 3$ in Fig. 5.15. However, the higher shear stress tends to drift the droplet towards the channel centerline. The combined effect of these results in

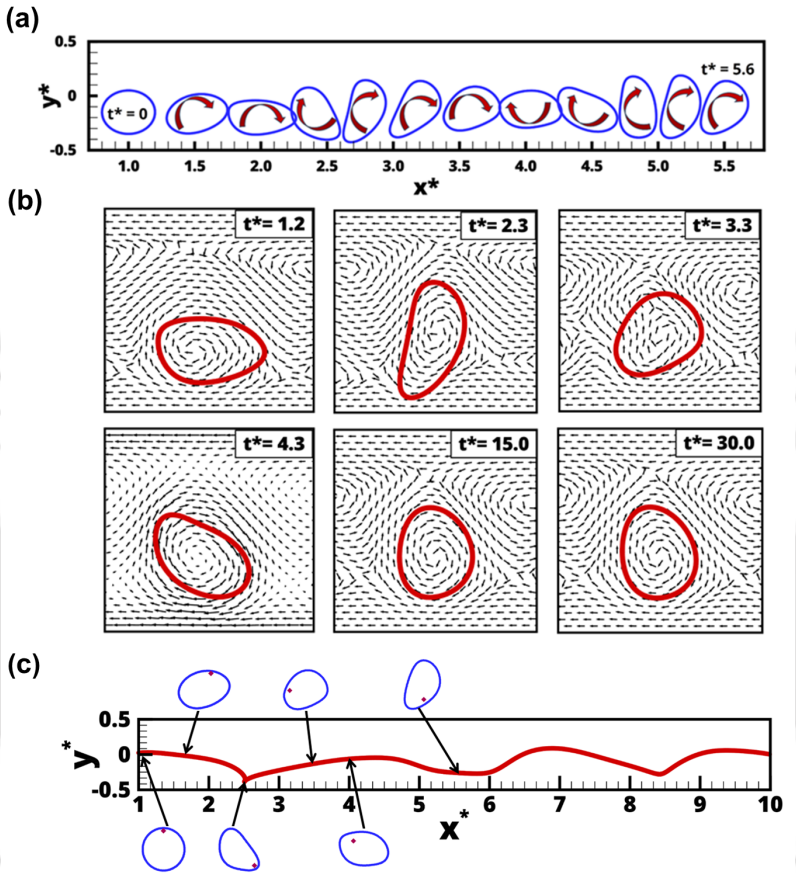

Figure 5.18: The rotation of a drop ($a^* = 0.4$) initially placed at $y_c = -0.15$ inside the channel subjected to electric field. Panel (a): Profile of the rotating drop for $t^* = 0$ to 5.6 and Panel (b): The vector field in and around the drop for $t^* = 1.2, 2.3, 3.3$, 4.3, 15 and 20. Panel (c): The trajectory of a marker point (marked as red dot) near the interface ($x^* = 1$, $y^* = 0.025$). The other parameters are Ca $= 0.7$, $\lambda = 1$, $E = 5$, $S = 2$ and $R = 0.5$. The flow field is presented in the frame of reference of the drop.

the rotation of the droplet which is further aided by the oblate shape of the drop. As the drop rotates, the influence of Magnus lift also comes into picture. It is to be noted that the present study is carried out for low Reynolds number flows inside a

microchannel, wherein the influence of inertia is negligible. The lift force associated with Magnus effect is dependent on the magnitude of both the translational as well as rotational velocity of the droplet. Due to the low migration velocity of the drop, the lift force generated is not significant in the face of strong opposing effect of the applied electric force. The drops thus settle at a certain equilibrium position that is between the channel centerline and initial off-center position. However, for the drops with lower permittivity ratio and higher conductivity ratio ($S < 1$ and $R > 1$), the elongation monotonically increases perpendicular to the flow direction and the deformation is more pronounced at higher magnitude of the applied electric field.

Figure 5.18(a) shows the rotation of a drop inside the channel along with translation for $E = 5$ over a duration of time between $t^* = 0$ and $t^* = 5.6$. However, this phenomenon is prominently exhibited until $t^* = 15$, and gradually dampens out with time. The vector fields are illustrated in Fig. 5.18(b) for $t^* = 1.2, 2.3, 3.3$, 4.3, 15.0 and 30.0. Figure 5.18(c) depicts the trajectory of a marker point near the interface of the drop and the channel liquid ($x = 1, y = 0.025$). The position of the marker point (in red dot) inside the drop is shown for different time instants as the drop migrates inside the channel. The x coordinate depicts the translational displacement of the drop together with the co-moving marker point whereas the displacement in the y direction illustrates the effect of rotational (clockwise) motion of the marker point while drop is in translational motion.

5.4 Summary

Numerical simulations of a neutrally buoyant droplet migrating in a two dimensional channel in the creeping flow regime have been performed using *Gerris*. The Navier-Stokes equations coupled with electric force terms and continuity equation have been solved to study droplet dynamics in a channel with fully-developed flow at the inlet, with and without the influence of an electric field. From the study on effect of drop size, it has been revealed that larger drops migrate slowly in the channel as compared to smaller drops but the lateral migration phenomenon is better exhibited by the larger drops. The cross stream migration phenomenon enhanced with increasing capillary number and decreased with increasing viscosity ratio. In the presence of electric field, it has been observed that for a drop fluid having high permittivity compared to the suspending fluid, the drop deforms highly and oscillates around its

mean position. It is also observed that a more conducting drop tends to migrate towards the channel centerline and the cross migration increases with the increase in E while a less conducting drop tends to settle down at a lateral position somewhere near the initial off-center position.

Chapter 6

Influence of Electric Field on Deformation of a Drop in Shear Flow

The deformation of a neutrally buoyant drop in shear flow is studied in a micro channel by considering both the drop fluid and the suspending medium as immiscible and incompressible. The walls of the channel serve as electrode and the deformable interface is captured using a volume-of-fluid approach coupled with solution of two-dimensional electro-hydrodynamic equations. Both dielectric and leaky dielectric fluids are considered in the study. It is observed that the drop deformation can be enhanced or suppressed by variation of the electrical properties of the fluids, viz, the permittivity ratio, electric field strength and conductivity ratio. The local electric field intensity varies spatially around the drop interface. The nature of electrical forces acting at the interface can be suitably tuned by modulating the applied field strength as well as the relative contrast in the fluid properties.

The contents in this chapter have been published as Nath, B., Biswas, G., and Dalal, A.(2019) 'Influence of electric field on deformation of a drop in shear flow', *Physics of Fluids*, vol. **31**, pp. 042102 (available online, DOI: https://doi.org/10.1063/1.5087066).

6.1 Introduction

The dynamics of a droplet in shear flow under the influence of an external electric field have been investigated by performing extensive numerical simulations. The study is again carried out by solving two-dimensional electrohydrodynamic equations and the interface is captured using a volume-of-fluid approach. For the case of dielectric fluids, the deformation of the drops can be either enhanced or reduced by varying the permittivity ratio and electric field strength. The nature of the polarization forces acting at the interface can be either compressive or tensile depending on the magnitude of the permittivity ratio. The local electric field intensity inside the drop is significantly altered due to the permittivity contrast between the fluids. The computations for leaky dielectric fluids reveal that the deformation of the drop can be effectively tuned by altering the permittivity as well as the conductivity ratios. The nature of charge accumulation and the electric forces acting at the interface are critically dependent on the relative contrast between the electric properties of both the phases. The conductivity ratio decides the magnitude and nature of charge at the upper and lower portions of the droplet interface thereby fundamentally maneuvering the droplet dynamics under the applied electric field.

The investigation on the deformation and orientation of a drop in shear flow is a subject of fundamental importance in dispersion science, in the field of lubrication [124] and in emulsification and mixing processes. For some microfluidics related applications, the study of drop dynamics in confined shear flows is relevant. In such confined channels, the wall effects act to stabilize elongated drop shapes and this feature stands very relevant for the production of elongated micro-structures utilized in several industrial applications, such as food processing, where the particle shape can be frozen by gelation [15].

The research interest in the field of drop dynamics in shear flow evoked ever since the first theoretical analysis of drop shape in shear flow was conducted by Taylor [125, 126]. Taylor showed that the shape of a sheared drop is governed by two non-dimensional parameters, namely, the viscosity ratio between the dispersed phase and the continuous phase and the magnitude of the dominance of viscous force over surface tension force, indicated by capillary number Ca. Torza *et al.* [127] experimentally validated the drop deformation parameter derived by Taylor and found very good agreement even at the values of Ca that were expected to be well beyond the range of validity of Taylor's analysis. With the increase in Ca, the pre-

dictions due to the theory deviated from experimental observations as pointed out by Elmendorp [128] since the calculated drop shape exhibited a neck in the middle. This discrepancy was expected as Taylor's theory was valid only in the limit of Ca << 1. Thereafter many researchers investigated the deformation of a drop in shear flow and observed deviations from Taylor's predictions at large values of Ca. In the absence of an electrostatic field the interplay of inertia and surface tension forces are responsible for the drop deformation which was depicted in several two- and three-dimensional studies [129–134] in shear flow. From the work of Taylor [126], Torza *et al.* [127] and Rumscheidt and Mason [135] it is evident that when a spherical drop is placed in a simple shear flow, it responds immediately by deforming and creating internal circulation. Renardy [131] studied the effect of confinement and inertia, in detail, and reported that the confinement in microchannels enables a drop to sustain significant elongation before the breakup is brought about. The mechanism is deemed to promote a mono-disperse droplet distribution. It has been established by some researchers [136–139] that if the drop is sufficiently more viscous than the suspending fluid then independent of the value of the surface tension, the shear flow deforms it until it reaches a stationary oblate stationary shape. Indefinite thinning and elongation occur in principle for large drop viscosities at zero Reynolds numbers as the shear is increased. Eventually the drop may tend to disintegrate due to non-hydrodynamic effects like Van der Waals forces. Sibillo *et al.* [15] reported about the complex oscillating transients and drop stabilization against breakup in micro confined shear flows and observed an elongated drop shape which would be unstable in the unbounded case. They showed that the wall effects can be exploited to obtain nearly monodisperse emulsions in microconfined shear flows.

In the presence of an electric field, the interfacial stresses get modified. In perfect dielectric fluids the normal components of the electric displacement field on either side of the interface match and the diffused charge layers are not formed at the interface. In the case of leaky dielectric fluids (poor conductors), even a small conductivity allows electric charge carriers to settle at the drop interface and this leads to the formation of a diffused charge layer [140]. Taylor [109] analyzed the static configuration of spherical drops in a creeping flow regime (zero Reynolds number limit) and analytically deduced a relation that dictates prolate and oblate shapes of the drops. Some researchers [8, 28, 113, 141, 142] studied the electrohydrodynamics of drops in axisymmetric configurations. Fernández *et al.* [116] considered electrostatic effects on two-dimensional oblate shaped drops in a channel motivated by the

experiments of Ozen *et al.* [143]. In their numerical model, Fernández *et al.* [116] approximated the discontinuous jump in the electric permittivity across the interface by a smoothed function. They then assumed that the electric field and the dielectric permittivity are continuous and incorporated a reduced form of the electrohydrodynamic force in the momentum equations [144]. Tomar *et al.* [145] derived a new representation of the electrohydrodynamic force satisfying the concept of continuum forces introduced by Brackbill *et al.* [52]. Recently, Borthakur *et al.* [21] used the electrohydrodynamic module of Gerris and studied drop-formation from submerged orifice in the presence of an electric field in both dielectric and leaky dielectric fluids.

As understood from the discussion above, this field of research is very relevant. However, even today, the understanding of the effects of confinement on drop deformation and orientation is rather limited. In fact, it is worth noticing that starting from the pioneering work of Taylor [3], most of the literature on flow-induced drop deformation is devoted to the unbounded flow situation. The presence of an electric field is known to further modify the interfacial stresses and hence a profound influence on the drop dynamics is expected. So far very few studies have been performed to account for the effect of the presence of electric field in drop deformation and its orientation in the microchannels. In view of this, in the present study, we emphasize on understanding the effect of electric field strength, permittivity ratio and conductivity ratio on the drop dynamics for perfect and leaky dielectric fluids.

The rest of the paper is arranged as follows : Sec. 6.2 discusses the formulation of the problem. The results obtained from the validation and grid convergence test performed to check the accuracy of the mathematical model are also discussed. This is followed by Sec. 6.3, where the results obtained from our computations for a wide range of parameters are discussed. The results include the study of drop deformation and orientation in the presence of an electric field for both dielectric and leaky dielectric fluids. Finally, the summary is drawn in Sec. 6.4.

6.2 Formulation

The formulation of the problem and solution methodology adapted to investigate the dynamics of an initially spherical droplet of radius R_o placed inside a microchannel of height H and subjected to shear is discussed in this section. The computational domain is shown in Fig. 6.1. The walls of the channel act as electrodes to apply

an external electric field. Due to the influence of shear, the morphology of the drop changes from the initial spherical shape to an ellipsoidal like shape. The maximum length of the drop is termed as L_{max} and minimum width as L_{min}. The angle which the major axis of the drop makes with the x-axis is denoted by θ. The total interfacial length of the deformed drop is denoted as L_i. The dispersed and the

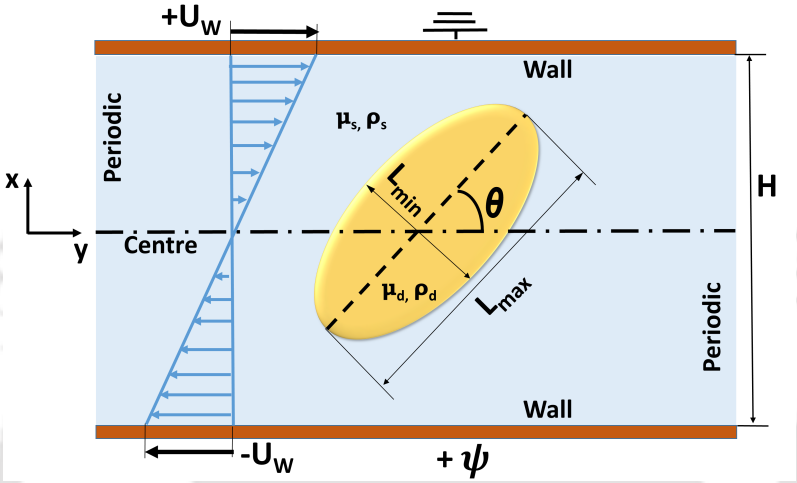

Figure 6.1: The schematic representation (not to scale) of a drop suspended inside a channel and deforming under the influence of external shear flow and electric field.

continuous fluids chosen in the study are assumed to be immiscible, incompressible and Newtonian. The viscosity and density of the dispersed fluid (droplet) and continuous fluid are (μ_d, ρ_d) and (μ_s, ρ_s), respectively. The deformation of the drop is quantified by introducing a term D_i called the deformation index, such that $D_i = (L_{max} - L_{min})\,/(L_{max} + L_{min})$.

6.2.1 Initial and boundary conditions

The initial and boundary conditions implemented to solve the governing equations are such that, in the beginning (at $t^* = 0$), both the fluids are considered to be static [121, 146, 147]. A continuous uniform shear is imposed in the channel by moving the walls in opposite directions at equal speeds. No slip and no penetration conditions are applied at the walls ($u = \pm U_w, v = 0$). The domain is considered to be periodic along x-axis. The shear rate is given by $\dot{\gamma} = U_w/H$, where U_w is the imposed velocity at the walls ($y = \pm H/2$). The external electric field is applied by

imposing constant voltage boundary conditions with $\psi = +\psi$ at the lower wall of the channel, while the upper wall is grounded ($\psi = 0$).

6.2.2 Numerical method

The deformation and orientation of a drop in a channel is studied using a finite volume open source computer code, *Gerris* [58] as mentioned in Section 2.3. The electro-hydro module [22] of Gerris is adequately capable of solving the incompressible Navier−Stokes equations coupled with an electric potential and electric charge density very accurately [68, 69, 121]. The detailed electro-hydrodynamic model adopted for the present study is described in Section. 2.4.

6.2.3 Non-dimensionalisation

The dimensionless parameters pertaining to this study are discussed in this subsection. The height of the channel, H, and wall velocity U_w are used as the length and velocity scales, respectively and μ_s is used as the viscosity scale. The aspect ratio, r^*, is the ratio of the initial droplet diameter to the height of the channel and is given by $2R_0/H$. The chosen reference quantities give rise to the following set of dimensionless parameters

$$\begin{aligned} \mathrm{Ca} &\equiv \frac{\mu_s U_w}{\gamma},\ \mathrm{Re} \equiv \frac{\rho_s U_w H}{\mu_s},\ \eta = \frac{\rho_d}{\rho_s},\ \lambda = \frac{\mu_d}{\mu_s}, \\ S &= \frac{\epsilon_d}{\epsilon_s},\ R = \frac{\sigma_d}{\sigma_s},\ E^* = \frac{E}{U_w}\sqrt{\frac{\epsilon_o}{\rho_s}},\ Re_E = \frac{\epsilon_s U_w}{\sigma_s H}. \end{aligned} \tag{6.1}$$

The parameters in Eq. (6.1) correspond to the capillary number, Reynolds number, density, viscosity, permittivity and conductivity ratios, a dimensionless electric field and electrical Reynolds number, respectively. Here, E_c is the characteristic scale for electric field strength given as $E_c = U_w\sqrt{\rho_s/\epsilon_s}$. The seemingly uncommon scaling for electric field is stimulated by the numerical work and is adopted so that the dimensionless parameter associated with the Maxwell stresses in Eq. (2.34) is unity. The dimensionless electric potential is given by, $\psi^* = \frac{\psi}{U_w L}\sqrt{\frac{\rho_s}{\epsilon_s}}$. For the sake of convenience, E^* and ψ^* are represented as E and ψ, respectively for the rest of the paper. In the present study, the Reynolds number is assumed to be small (Re = 1). Furthermore, we have studied the migration of a neutrally buoyant droplet in

the simulations ($\eta = 1$). The results are presented in terms of dimensionless time, $t^* \equiv tU_w/H$.

6.2.4 Validation

We demonstrate the accuracy of the adopted two-phase numerical model by comparing our results with existing literature. Hua *et al.* [7] investigated the deformation of a drop in confined shear flow. Figure 6.2(a) compares the deformation of a drop obtained from the present simulations with the results of Hua *et al.* under conditions of $r^* = 1/6$, Ca $= 0.2$, Re $= 1$ and $\lambda = 1$. It is observed that the present simulations agree well with the numerical results of Hua *et al.* [7]. The present study also incorporates an electro-hydrodynamic model to simulate the electric field effects. The first-order small deformation model for a two-dimensional viscous drop was developed by Feng [8] and is analogous to Taylor's linear model for a spherical drop [109]. In the linear model the equilibrium drop deformation was approximated by -

$D_i = \frac{R^2+R+1-3S}{3(1+R)^2}$ Ca$_E$

where, Ca$_E$ is called the electric capillary number and defined as Ca$_E = \frac{E^2\epsilon_s R}{\gamma}$. Figure 6.2(b) shows a comparison between the results from our present simulations with the analytical predictions of Feng [8] for $S = 2$ and $R = 2.5$. A good quantitative agreement is observed thereby validating our electro-hydrodynamic model.

6.2.5 Grid independence test

The grid independence test is conducted for a drop of size $r^* = 0.35$ in a channel for Ca $= 0.7$ and $\lambda = 1$, in the absence of an electric field. The adaptive mesh refinement (AMR) feature of *Gerris* is employed to increase the grid density near the interfacial region while maintaining a relatively coarser mesh elsewhere [58]. The refinement is done based on the gradient of volume fraction. The smallest (dimensionless) cell sizes corresponding to grid levels 5, 6, 7, and 8 are 0.031, 0.016, 0.008, and 0.004, respectively. The temporal variations of D_i for different grid refinement levels are presented in Fig. 6.3(a). The inset figure in Fig. 6.3(a) focuses on the deformation peaks for the different levels. It is observed that D_i measured at $t^* = 30$ differs by $\sim 0.292\%$ between levels 7 and 8. In view of optimizing the computational time and cost without compromising the accuracy of the results, grids with refinement level 7

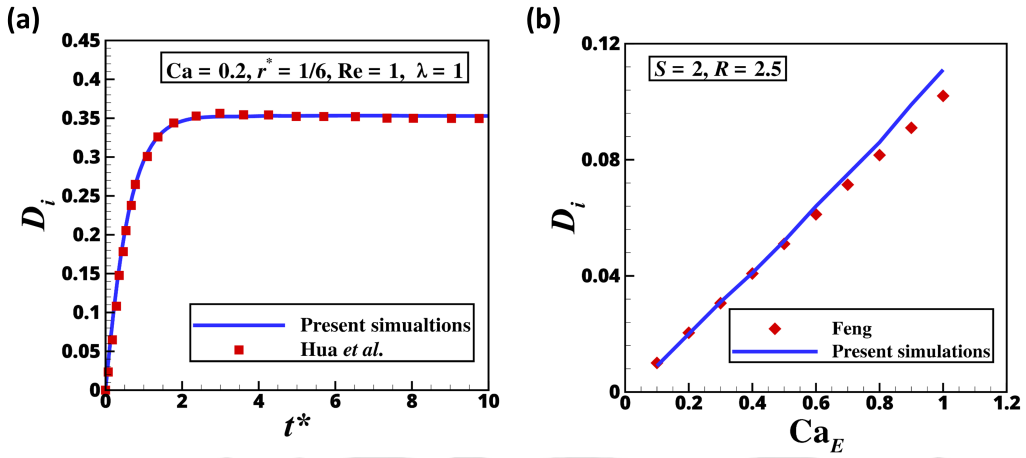

Figure 6.2: Comparison of drop deformation computed from the present simulations with (a) Numerical results of Hua *et al.* [7] and (b) Analytical predictions of Feng [8], respectively.

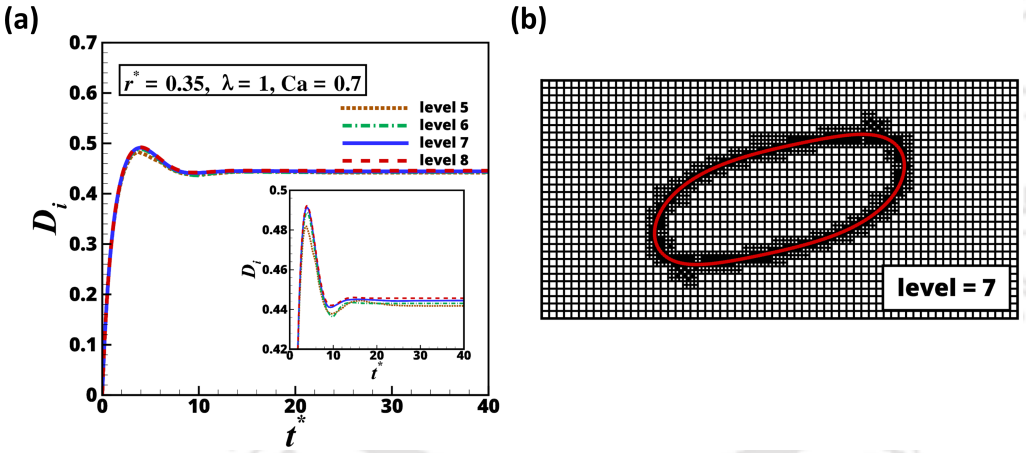

Figure 6.3: Grid convergence test. Panel (a): Comparison of D_i for different levels of grid refinement. The different parameters considered are $r^* = 0.35$, Ca $= 0.7$ and $\lambda = 1.0$ and Panel (b): Snapshot of adaptive mesh generation using refinement level of 7.

are deployed to generate the rest of the results presented in this study. Figure **??**(b) shows a snapshot of level 7 refinement for $t^* = 30$.

6.2.6 Fluid properties

The immiscible Newtonian mediums considered in the study, can be assumed to be composed of silicon oil as dispersed phase and castor oil as suspending phase. Different viscosity ratios considered for the parametric studies can be obtained by considering different grades of silicon oil [122]. Perfect dielectric fluids can be considered to be composed of a silicon oil droplet in a medium of castor oil or vice versa, depending on the permittivity ratio [140].

6.3 Results and discussion

Having validated our predictions with earlier experimental and numerical results, in this section, we discuss the results obtained by varying the pertinent electrical parameters. Due to the presence of electric field an additional stress is introduced at the interface which is known as Maxwell stress. The shape and deformation of the drop in the presence of an electric field is influenced by the combined effect of surface tension, viscous forces and Maxwell stress. We commence our investigations on the deformation of a droplet in shear flow under the action of an imposed electric field employing the assumption of perfect dielectric fluids. Subsequently, we extend our study by considering the fluids to be leaky dielectric. A large set of operating conditions are to be taken under consideration and in the results that follow, we have fixed the values of r^*, Ca and λ at 0.35, 0.5 and 1.0 throughout the entire study. The influence of the variation of these parameters on the droplet deformation and orientation have been investigated by a host of previous researchers [126, 127, 131, 133, 135]. In the current analysis, we focus on the electro-hydrodynamics of the simulated system and study extensively the impact of the electrical properties as well as the applied electric field on the droplet behavior and its associated dynamics.

6.3.1 Perfect dielectric

We investigate the influence of the permittivity ratio (S) on the deformation and orientation of the droplet keeping the electric field strength E fixed at 10. Figure 6.4(a) shows the temporal variation of the deformation parameter D_i with S. It is observed that with the increase in S, D_i increases monotonically. However, the deformation curve undergoes a maxima and minima, which is more pronounced for

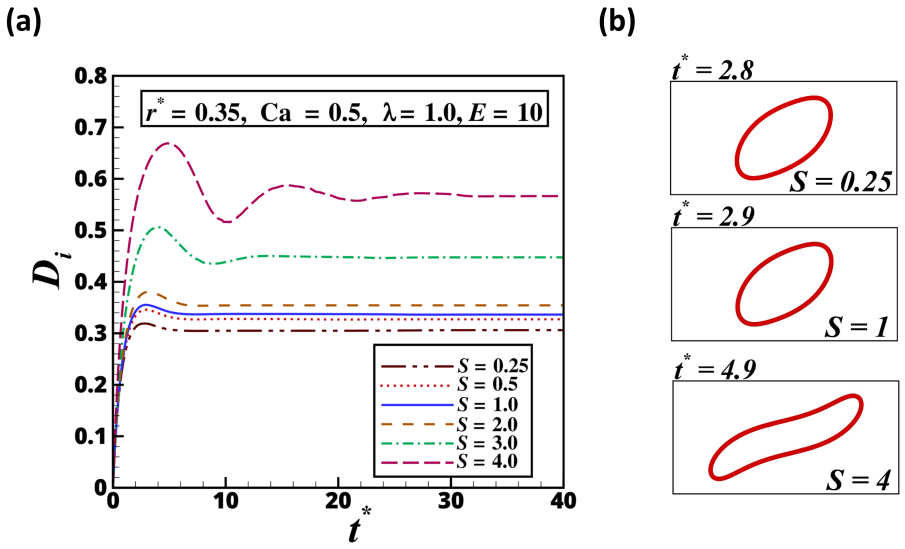

Figure 6.4: Effect of permittivity ratio on the (a) Temporal variation of deformation parameter D_i, and (b) The morphology of the drop when deformation is maximum (for $S = 0.25, 1$ and 4, respectively). The electric field E is fixed at 10.0.

$S > 1$. The shape of the drop at the instant of maximum deformation is shown in Fig. 6.4(b) for $S = 0.25, 1$ and 4, respectively. It is seen that the drop profile changes marginally between $S = 0.25$ and 1. However, for $S = 4$ we observe that at the point of maximum deformation, the drop takes a very unstable non ellipsoidal shape. The oscillations noticed in Fig. 6.4(a) for $S = 4$, reveal that in order to overcome the instability caused due to sudden overshoot in deformation, the drop undergoes expansion and contraction several times before attaining a steady shape. Figure 6.5 shows the temporal evolution of a drop with $S = 4$. It is observed that with the onset of incident shear flow, the drop undergoes substantial elongation briskly attaining several unsteady shapes, as seen from $t^* = 0$ to 5. This leads to an overshoot in D_i as observed in Fig. 6.4(a). To gain stability and attain a steady shape, the drop keeps expanding and contracting for sometime. It is noticed that, beyond $t^* = 5$, the deformation starts contracting and at $t^* = 10$ we can see a compressed drop. However, for $10 < t^* < 15$ the drop again undergoes expansion followed by slight compression for $15 < t^* < 20$. This continues till $t^* = 30$, beyond which the drop attains a steady shape and D_i ceases to change, as confirmed from Figs. 6.5 and 6.4(a). Figure 6.6 (a) depicts the interface profiles of the drops after attaining steady state for different magnitudes of S. A quantitative picture

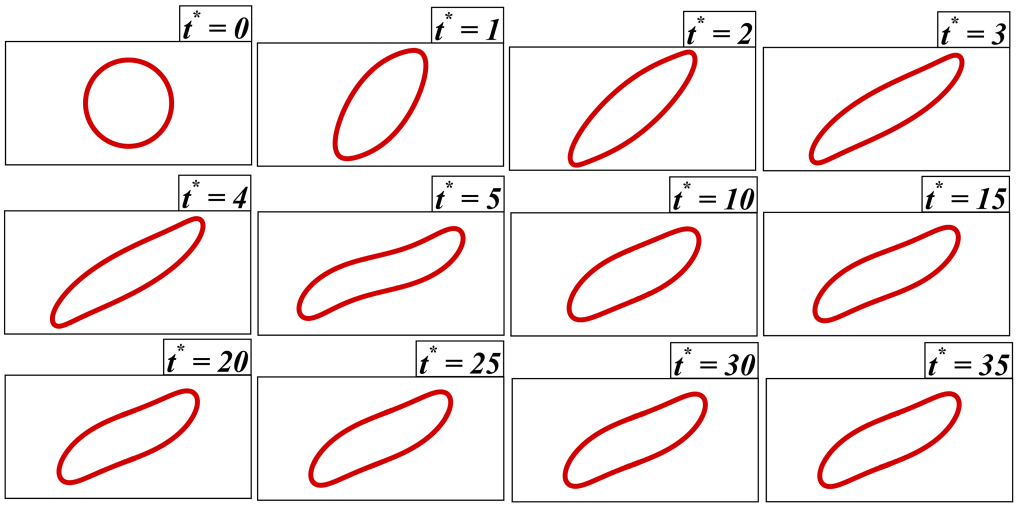

Figure 6.5: Evolution of a drop with time for $S = 4$. The electric field E is fixed at 10.0.

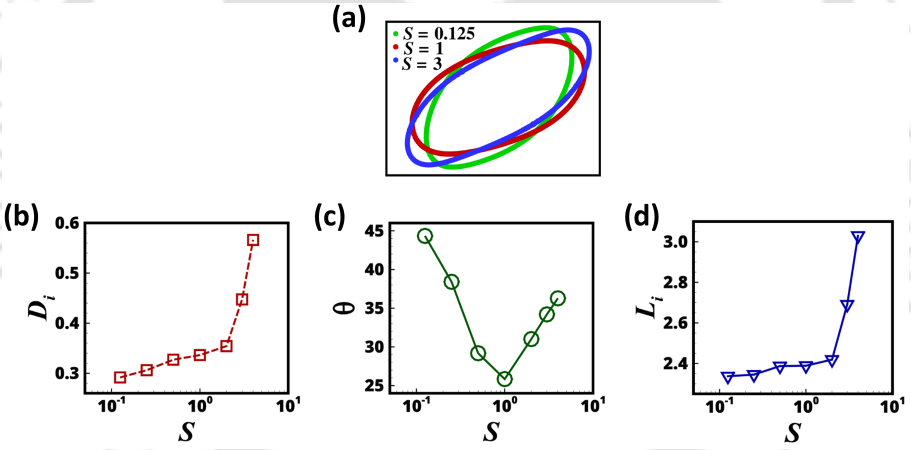

Figure 6.6: Effect of permittivity ratio on the (a) Interface morphology of the droplet, (b) Deformation parameter D_i, (c) Orientation angle θ and (d) Interfacial length L_i. The electric field E is fixed at 10.0.

of the variations of steady state deformation parameter D_i, orientation angle θ and interfacial length L_i with permittivity ratio S are presented in Figs. 6.6 (b), (c) and (d) respectively. The dotted line represents the condition when electric field is absent. It can be observed that, in comparison to the condition of no electric field, the deformation of the drop is enhanced due to the application of electric field for $S > 1$ and suppressed under the condition of $S < 1$. The orientation angle, however,

monotonically increases when S is either increased or decreased beyond unity. The interfacial length L_i follows a similar trend to that of the deformation parameter D_i.

In order to explain the primary difference in the dynamics brought about by

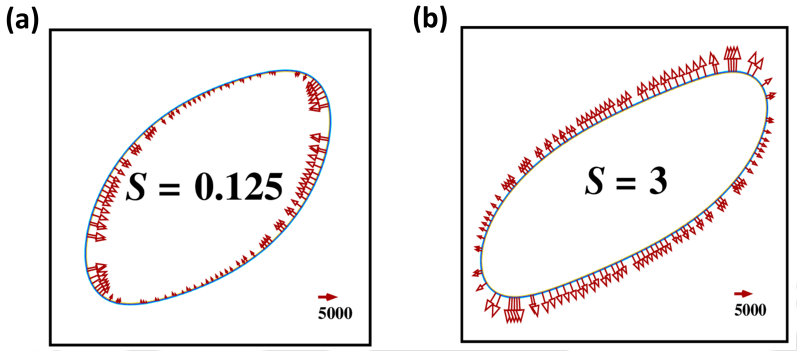

Figure 6.7: The electric forces acting at the drop interface for (a) $S = 0.125$ and (b) $S = 3.0$ under an applied electric field of $E = 10.0$. Only selected force vectors are plotted to maintain clarity.

the variation of S, we study the influence of the electric forces acting at the interface. For the case of dielectric fluids, the polarization force acts at the interface and the magnitude of the electric force is proportional to the contrast of permittivity existing between the two phases and squared magnitude of the applied electric field ($F_E = -\frac{1}{2}E^2\nabla\epsilon$). The electric force is directed from the medium of higher permittivity to lower permittivity and acts only on the interface as the permittivity gradient exists only across the interface. Additionally, the polarization force is always locally perpendicular to the interface. For a fixed value of E, the electric force acting at the interface increases with the increase in the permittivity contrast between the two phases, i.e. either an increase or decrease of S from unity. For $S = 1$, the values of D_i, θ and L_i match with the scenario when electric field is absent, as shown in Fig. 6.6. This can be attributed to the fact that when no permittivity contrast exists between the two phases ($S = 1$), the electric force vanishes at the interface. The distribution of the polarization force acting at the interface is presented for $S = 0.125$ and 3.0 in Fig. 6.7. It can be clearly discerned that the electric forces are compressive in nature for $S = 0.125$ and tensile in nature for the case of $S = 3.0$. As a consequence, the drop deformation is suppressed under the condition of $S < 1$ and enhanced when $S > 1$. Additionally, the distribution of

the forces show a higher non-uniformity at the interface for $S = 0.125$. Due to the spatial inhomogeneity of the electric forces, a counter-clockwise couple is generated which tends to increase the orientation angle of drop at steady state. The interfacial length L_i is closely linked to the extent of deformation and hence L_i increases when the drop deformation increases ($S > 1$) and decreases for reduced drop deformation ($S < 1$).

The inhomogeneity of the electric forces can be elucidated by considering the

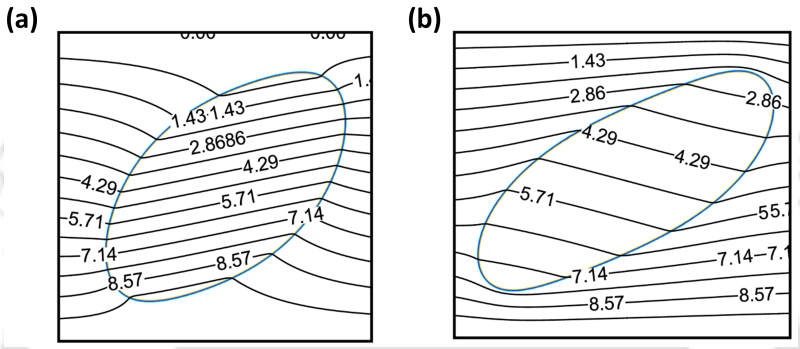

Figure 6.8: Iso-contour lines of the electric potential for (a) $S = 0.125$ and (b) $S = 3.0$ under an applied electric field of $E = 10.0$.

local variation of the electric field strength. In the absence of the drop phase, a spatially uniform electric field with lines of constant potential parallel to the electrodes is generated. Due to the presence of the drop phase, the uniform electric field is disturbed due to the disparity in the dielectric permittivity between the two phases. Figure 6.8 presents the iso-contour lines of the electric potential superimposed on the contour of vorticity for $S = 0.125$ and 3.0. It can observed that the iso-potential lines are non-uniformly spaced in the surrounding fluid near the drop interface for $S = 0.125$. The higher spacing between the iso-potential lines signifies regions of lower electric field intensity. For the condition of $S = 0.125$, two regions of low electric field intensity can be identified near the top and bottom of the droplet and hence, the magnitude of electric forces diminishes in these regions. In contrast, for the case of $S = 3.0$, the iso-potential lines have an approximately uniform distribution around the interface which leads to significantly higher electric forces acting on the entire droplet.

We now explore the influence of the applied electric field strength (E) on the droplet dynamics. Figure 6.9(a) shows the temporal variation of D_i for E varying

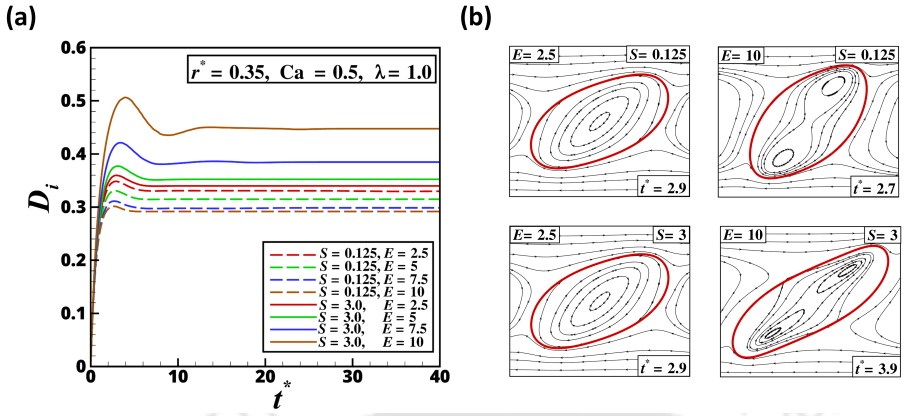

Figure 6.9: Effect of permittivity ratio on the (a) Temporal variation of deformation parameter D_i and (b) Flow field in and around the drop while it undergoes peak deformation.

in the range of 2.5 to 10. The results obtained are compared for two set of permittivity ratios, $S = 0.125$ and 3. It is observed that contrasting deformation trend is exhibited for the two cases. For $S = 3$, D_i increases with increase in E (as shown by the solid lines) whereas for $S = 0.125$, the deformation decreases with increase in E (represented by dashed lines). A close observation of Fig. 6.9(a) reveals that the deformation peak shifts to the right with increasing E for $S = 3$ while it shifts to the left with increase in E for $S = 0.125$. Figure 6.9(b) shows the flow field in and around a droplet (for $S = 0.125$ and 3, respectively) when it undergoes peak deformation influenced by $E = 2.5$ and 10, respectively. It is seen that for both $S = 0.125$ and 3, the peak deformation is reached at $t^* = 2.9$ for $E = 2.5$, although the deformation is slightly higher for $S = 3$. The inner circulation of the fluid inside the drop is similar in both the cases, for $E = 2.5$. However, for $E = 10$, two vortices are formed inside the drop, in each case. For $S = 0.125$, the deformation reaches its maxima soon after the onset of induced shear flow ($t^* = 2.7$), forming stable vortices near the poles that tends to orient the drop in the direction of external electric field. For $S = 3$, the peak deformation is reached at $t^* = 3.9$, and unstable vortices are noticed inside the drop. Thereafter, the drop subjected to $S = 3$ and $E = 10$ undergoes several transitions in shape to attain a steady shape. Figure 6.10 presents the variation of D_i, θ and L_i with E for two different permittivity ratios, $S = 0.125$ and 3.0 in case of drops that have attained a steady shape. It can be discerned from Fig. 6.10 that D_i and L_i show a contrasting behavior with increasing E for $S = 0.125$

and 3.0 (as seen in 6.9(a) previously). This is because, as the electric force acting at the interface is proportional to E^2, the increasing electric field strength enhances or diminishes the droplet deformation for $S = 0.125$ and 3.0, respectively. However, due to the higher strength of the counter-clockwise couple with increasing E, the magnitude of θ increases under both the conditions of $S = 0.125$ and 3.0.

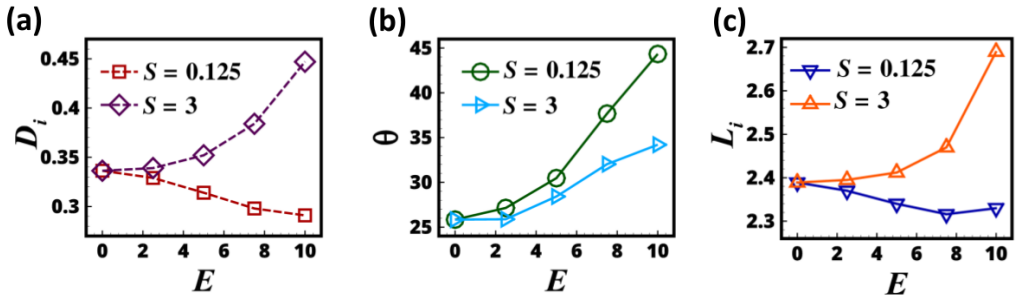

Figure 6.10: Effect of electric field strength on the (a) Deformation parameter D_i, (b) Orientation angle θ and (c) Interfacial length L_i for $S = 0.125$ and $S = 3.0$.

6.3.2 Leaky dielectric fluids

In this section, we demonstrate the results from our computations employing the leaky dielectric model. Taylor [109] derived an analytical expression for the deformation of a stationary droplet in an uniform electric field which depends on the ratios of fluid permittivity S as well as its conductivity R. Due to the small but finite electrical conductivity of the liquids, the leaky dielectric model supports the presence of both normal and tangential electric stresses at the interface. Hence, we expect differences in the dynamics of the droplets between perfect dielectric and leaky dielectric systems. The electric Reynolds number defined as, $Re_E = \frac{\epsilon_s U_w}{\sigma_s H} = \frac{(\epsilon_s/\sigma_s)}{(H/U_w)} = \frac{t_E}{t_f}$, is the ratio of time scale of charge relaxation (electric time scale t_E) to the flow time scale t_f. For $t_E < t_f$, no volumetric charges exist in the bulk fluid and the charges accumulate at the interface instantaneously satisfying the assumption of leaky dielectric fluids. In our present investigations, we have maintained a fixed value of $Re_E = 0.1$ for the entire study using leaky dielectric fluids. Additionally all the computed results are presented for steady state for leaky dielectric fluids.

We consider two (R, S) pairs of leaky dielectric fluids with values of $(0.5, 2.0)$ and $(2.0, 0.5)$ respectively, denoted as system A and B respectively. System A rep-

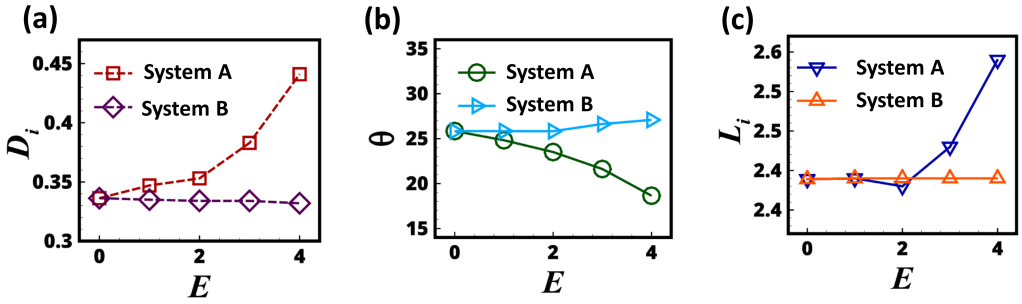

Figure 6.11: Effect of electric field strength on the (a) Deformation parameter D_i, (b) Orientation angle θ and (c) Interfacial length L_i for system A and B.

resents a drop whose electrical conductivity is lower but permittivity is higher than the surrounding fluid while, system B represents a drop whose conductivity is higher but permittivity is lower than the surrounding fluid. Figure 6.11 presents the influence of the applied electric field strength E on the dynamics of deformation and orientation of the droplet for the two systems under consideration. It can be clearly perceived from Fig. 6.11 that the droplet deformation D_i and interfacial length L_i increases with applied field strength for System A whereas the orientation angle decreases. In contrast, the droplet of System B is almost insensitive to the variation of E in comparison to System A.

In order to shed light on the differing behavior of the two systems under consider-

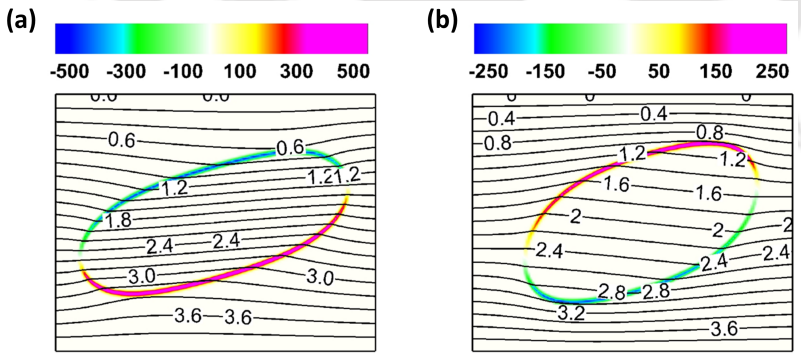

Figure 6.12: Iso-contour lines of the electric potential for (a) System A and (b) System B under an applied electric field of $E = 4.0$.

ation, we compare the charges accumulated at the interface between system A and B as shown in Fig. 6.12. For system A, the upper portion of the drop becomes

negatively charged whereas the lower portion is positively charged. In complete contrast to system A, positive charge accumulates at the upper portion of the drop whereas negative charges are observed near the lower portion of the drop in system B. Additionally, the magnitude of charge accumulation is higher in system A in comparison to system B. It is to be noted that in the present study, the lower wall is maintained at a constant electric potential thereby resulting in the generation of an electric field which is directed along the $+y$ direction. The resultant effect of this dissimilar charge accumulation between the two systems manifests in the opposing nature of Coulombic forces acting at the drop interface.

Figure 6.13 illustrates the electric forces acting on the interface for system A

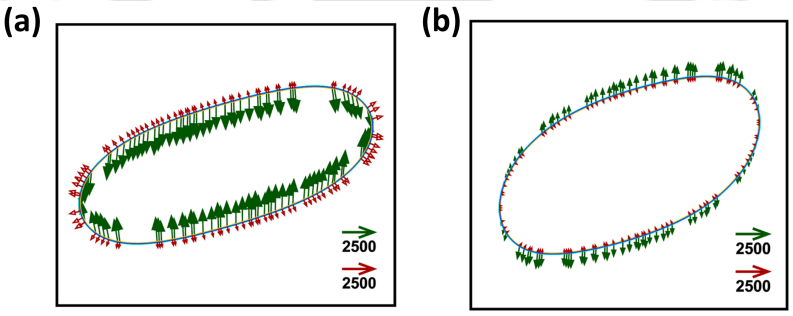

Figure 6.13: The electric forces acting at the drop interface for (a) System A and (b) System B under an applied electric field of $E = 4.0$. The Coulombic forces acting on the free charges ($q_v\mathbf{E}$) are shown in green color, whereas the polarization forces acting on the dipoles ($-\frac{1}{2}\mathbf{E}\cdot\mathbf{E}\nabla\epsilon$) are depicted in red colour. Only selected force vectors are plotted to maintain clarity.

and B keeping E fixed at 4.0. The net electric forces for leaky dielectric fluids can be categorized into the Coulombic component ($q_v\mathbf{E}$) exerted on the free charges and polarization component acting on the dipoles ($-\frac{1}{2}\mathbf{E}\cdot\mathbf{E}\nabla\epsilon$). It can be observed from Fig. 6.13 that the Coulombic component dominates over the polarization forces for both systems A and B. The polarization forces are directed from the medium of higher to lower permittivity for both the systems. For system A, the nature of Coulombic forces are overall compressive, excluding the region near the poles of the deformed drop. It is to be noted that the the polarization forces always act normal to the interface whereas the Coulombic forces have both a normal as well as a tangential component at the interface. A close examination of the force distribution

for system A reveals that near the pole region, the Coulombic forces are mostly tangential in nature. Furthermore, the magnitude of the polarization forces are significantly higher at the drop poles. This results in a net tensile pull at the poles of the drop and the drop elongates along the ellipsoidal axis. The compressive nature of the Coulombic forces lowers the angle of orientation at steady state for system A. In contrast, the nature of Coulombic forces are overall tensile in nature for system B. The magnitude of both polarization and Coulombic forces are significantly reduced in comparison to system A. As such, the dynamics remain relatively insensitive to the change of E for system B.

We now investigate the influence of conductivity ratio R keeping the electric field

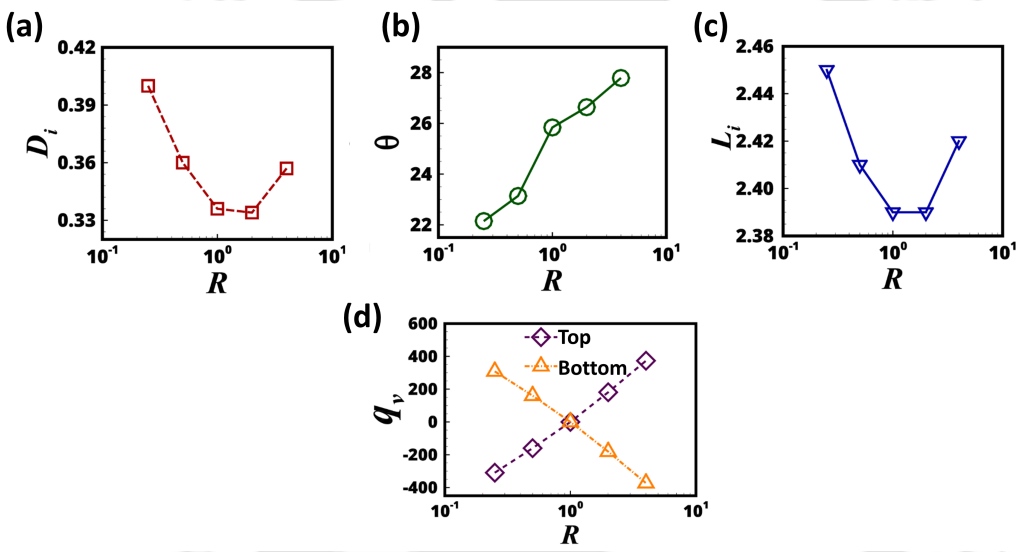

Figure 6.14: Effect of conductivity ratio on the (a) Deformation parameter D_i, (b) Orientation angle θ, (c) Interfacial length L_i and (d) Volumetric charge density q_v. The electric field E and permittivity ratio S are fixed at 4.0 and 1.0.

strength and permittivity fixed at 4.0 and 1.0. The variation of D_i, θ and L_i with increasing R is depicted in Fig. 6.14. The results demonstrate that θ and L_i increases when the conductivity contrast between the fluids is enhanced, i.e. for either R greater or lesser than unity. However, the orientation angle decreases when θ is lesser than unity and increases for θ greater than unity. In order to highlight the primary difference brought about by the change of R, we present the maximum charge (either positive or negative) accumulated in both the top ($y > 0$) and bottom ($y < 0$) portions of the drop as illustrated in Fig. 6.14 (d). It can be clearly

discerned that the charge accumulation shows a transition from negative (positive) to positive (negative) in the top (bottom) portion of the drop as R is increased beyond unity. For $R = 1.0$, the charge vanishes over the entire interface and Coulombic forces ceases to exist. The contrasting nature of charge accumulation at the top and bottom portions of the drop and its variation with changing R modulates the behavior of the Coulombic forces thereby significantly altering the dynamics of the droplets.

6.4 Summary

This study investigates the influence of an external electric field on the deformation and orientation of a drop in shear flow inside a microchannel. The two-dimensional simulations are performed employing the volume-of-fluid interface capturing method coupled with electro-hydrodynamic equations in the framework of *Gerris*. Both the immiscible fluids are considered as either perfect dielectrics or leaky dielectrics. It is observed that drop deformation can be either enhanced or reduced for dielectric fluids, depending on the value of permittivity ratio S. The nature of polarization forces are tensile when the permittivity of drop fluid is higher than the suspending fluid and compressive in the reverse case. For leaky dielectrics, we observed contrasting behaviour of drop deformation with electric field strength for drops suspended in a medium with higher drop conductivity and less permittivity as compared to the opposite case. The charge accumulated at the interface of the drop suspended in the two varying systems are also opposite in nature.

Chapter 7

Understanding Flow Dynamics, Viability and Metastatic Potency of Cervical Cancer (HeLa) Cells through Constricted Microchannel

To investigate the phenomenon of metastasis of cancer cells, a constricted microchannel was designed and fabricated. Cervical cancer (HeLa) cells were taken as a model cell line. Under experimental conditions, the cells deformed while passing through the constriction, allowing quantification of several hydrodynamic parameters such as entry time, transit velocity and elongation index along with many other biological parameters. Reasonable viability of the cells after passage through the constriction, determined by dual AO/EtBr staining, was substantiated by trypan blue dye exclusion assay that confirmed the retention of around 50% viable HeLa cell population at the outlet. The expression of MMP2 protein in the cells confirmed that the cells retain their metastatic potency at the channel outlet.

The contents in this chapter have been published as Nath, B., Raza, A., Sethi, V., Dalal, A., Ghosh, S.S., and Biswas, G.(2018) 'Understanding flow dynamics, viability and metastatic potency of cervical cancer (HeLa) cells through constricted microchannel', *Scientific Reports*, vol. **8**, pp. 17537 (available online, DOI: https://doi.org/10.1038/s41598-018-35646-3).

7.1 Introduction

Even in this modern era of cancer therapeutics, scientists and oncologists have not been able to resolve the mystery of metastatic cancer, which causes high mortality worldwide. In many instances, cancer is found to be reinvigorated in the other parts of the body, where chemotherapeutic drugs cease to work. Escalation of doses is often seen to damage healthy cells and worsen the prognosis [148]. A population of small, loosely bound clusters of cancer cells deriving from the primary tumour sites, also known as circulating tumour cells (CTCs), are able to stray away from the aggregate cluster through motion in the bloodstream or the lymphatic system, causing metastasis [149]. Hence, the analysis of CTC dynamics plays a paramount role in understanding the nature of parent tumour aggregates [150]. CTCs are often utilized as effective blood-borne biomarkers to enhance treatment methodologies [151] and curtail metastasis [152]. They also provide a measure of cancer genotype during therapy and phases of disease progression. About 5 to 50 CTCs per 5 ml of blood in the bloodstream of several cancer patients [149] have been reported to pass through even micron-sized capillaries and undergo great deformation, with a pronounced impact on their morphology. The isolation of CTC clusters from the peripheral blood of cancer patients has established their presence in the blood flow and their ability to pass successfully through the capillary beds and finger capillaries [153–159]. A thorough investigation of these aspects may lead to a better estimation of the nature of drugs and requirements of modalities to manage the treatment.

In the past few decades, several efforts have been made to elucidate the role of CTCs in seeding metastasis, where two or more CTCs form clusters, and these clusters are reported to be strong initiators of metastasis compared with singlets [153, 160–162]. The flow of cells in a capillary is complex owing to the size of the capillary (5 to 10 μm), and if cancer cells were to exhibit increased deformability they would have a higher probability of migrating to other parts of the body [163]. However, the nucleus is approximately 5 to 10 times stiffer than the surrounding cytoskeleton and thereby resists large changes in shape [164]. Therefore, the nucleus is thought to be the rate-limiting organelle regarding migration through small openings. Yamauchi *et al.* studied the cytoplasmic and nuclear deformation of cancer cells migrating in capillaries by injecting cells into the hearts of nude mice [165]. It is often challenging to study the behavior of CTCs in real conditions, hence constricted microfluidic channels with a width smaller than the diameter of the cells

are often fabricated using standard microfabrication techniques, as they are efficient in providing an environment to mimic in vivo capillaries [166]. Such constricted channels have been used to evaluate the mechanical properties of red blood cells (RBCs) [167–171], leukocytes [172–174] and cancer cells [175–177] . For example, Hou *et al.* [176] demonstrated experimentally a simple microfluidic channel to distinguish the difference in stiffness between benign and breast cancer cells. Several other groups have studied the behavior of CTCs in capillaries computationally [177, 178]. Numerical adaptation to study the dynamics of CTCs allows precise control over the various important hydrodynamic parameters to elucidate the transit behavior of the CTC clusters only. The recent experimental and numerical work of Au *et al.*. [177] demonstrated the flow of CTC aggregates through capillaries and negated restriction of the passage of CTCs through capillaries owing to the difference between the size of the tumour cells and the diameters of the capillaries [179].

The main objective of this work is to elucidate the flow behavior of metastatic cancer cells experimentally, similar to CTCs, evaluating the flow dynamics and viability indices of cancer cells in a constricted microchannel. For this purpose, cervical cancer (HeLa) cells have been used as a model system to examine metastatic flow. CTCs of HeLa have been studied by several other researchers recently [150, 180, 181]. To emulate the flow conditions, a microchannel having both converging and diverging sections with a constricted portion is fabricated using polydimethylsiloxane (PDMS), and the open surface was sealed with a glass cover-slide. HeLa cells have been allowed to pass through the constricted channels of width 7 μm for a distance of 200 μm at a constant peristaltic flow rate (30 μl/h). In contradiction to the decades-held assumption that owing to the difference in size between the CTC diameter and diameter of capillaries, the clusters are incapable of traversing through microcapillaries [182], we aim to find how the Hela cells are capable of migrating through microcapillaries by undergoing immense deformation. Physical parameters such as entry time, transit velocity and elongation index of a single HeLa cell are evaluated using representative images deconvoluted from high-speed videographs. Although, a similar investigation on motion of CTCs by Au *et al.* [177] showed deformation of CTCs traversing through capillaries, but there was no experimental evidence on either cell viability or metastatic gene expression profile to explain biomimetic conditions. These queries motivated us to extend our study in the direction of addressing some crucial biological behaviour of these transiting HeLa cells that would help us to understand the potency of cancer cells to metastasize at dis-

tant sites passing through microcapillaries. To the best of our knowledge, this is the first experimental report to demonstrate the existence of live and metastatic populations of cancer cells after passing through a constriction, which could have a significant impact on revealing the therapeutic modalities of metastatic cancers in the near future. The crux of the current concept is illustrated in the Fig. 7.1

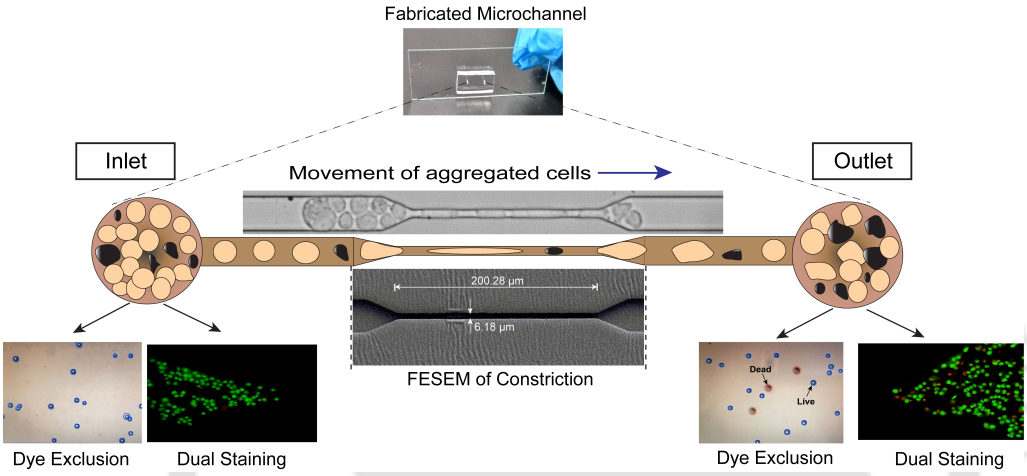

Figure 7.1: Schematic representation of the motion of aggregated HeLa cells passing through a microcapillary to seed distant metastasis.

7.2 Materials and methods

The procedure incorporated in fabricating the channels, cultivating the HeLa cells and setting up the experimental equipments have been discussed in details in Chapter 3. The materials and methodolgy adopted in the present experiments are discussed below.

7.2.1 Reagents and chemicals

All molecular grade chemicals and reagents were purchased from Sigma-Aldrich, unless mentioned otherwise.

7.2.2 Dual staining

Morphological identification of live, apoptotic and necrotic cells was performed by dual staining with Acridine Orange (AO)/ethidium bromide (EtBr). EtBr stains only the DNA of the dead or membrane-compromised cells whereas AO stains all the cells. HeLa cells were taken in a 1.5 ml tube and stained with a mixture of 2 μg/ml AO and 6 μg/ml EtBr and kept in the dark at 37 °C. After 10 min, the cells were centrifuged at 650 rpm for 5 min and the pelleted cells were redispersed in the DMEM medium for further processing. The cells were visualized under an epi-fluorescence microscope (Eclipse Ti-U, Nikon, Tokyo, Japan) using 10X objective. Excitation filter of 480/15 nm was used to collect green fluorescence of AO, whereas 540/25 nm excitation filter was used for collecting red fluorescence of EtBr.

7.2.3 Trypan blue staining

Trypan blue dye is used to stain membrane-compromised or dead cells, whereas live cells exclude the dye. HeLa cells were seeded at a density of 1×10^5 in a 60 mm cell culture dish in the presence of DMEM medium. Confluent cells were washed with PBS and resuspended in fresh DMEM medium in an Eppendorf tube. Equal volumes of trypan blue dye (10 μl) and the cells were mixed and loaded on the counting chamber. The viable cells (%) were counted using a Countess automated cell counter (Invitrogen). The images highlighting the live and dead cells were also captured using the same instrument.

7.2.4 Virulence study

A virulence study was performed to investigate whether the HeLa cells retain their metastatic ability after passing through the channel. For this, HeLa cells were grown in a 60 mm cell culture dish and subsequently harvested. The cells were collected in an Eppendorf tube after passing through the channel and tube. The collected cells were dispersed in DMEM medium in a 60 mm cell culture dish, regrown and observed at 10X magnification under a bright field microscope (Eclipse Ti-U, Nikon, Tokyo, Japan) for 12, 48 and 72 h. Metastatic gene expression analysis Matrix metalloproteinases (MMPs) are a group of enzymes that are mostly responsible for oncogenesis, growth and normal tissue turnover by degrading most of the extracellular matrix [183]. MMP2 expression was examined using quantitative real-time PCR

(qPCR) in HeLa cells before and after passing through the microchannel. After passing through the microchannel, the cells were collected and grown to confluency on a culture plate. Further, the cells were lysed and total RNA was isolated. Total RNA (1 μg) was used to prepare cDNA using a Verso cDNA Kit (Thermo Scientific). qPCR was performed using the MMP2 primers and SYBR Green as reporter dye (Power SYBR Green PCR master mix, Applied Biosystems) in a Rotor-Gene Q (Qiagen). The relative MMP2 mRNA expression was calculated by the $\Delta\Delta$Ct method using GAPDH, the endogenous control.

7.3 Results and discussion

7.3.1 Characterisation and flow profile of HeLa cells through a constricted microchannel

The design of the microchannel is shown in Fig. 7.2(a). The architecture of the fabricated PDMS-based microchannel was visualized under a bright-field microscope (Fig. 7.2(b)). The lower panel in Fig. 7.2(b) shows a magnified view of the constricted portion of the channel. The precise width and length of the constricted section were ascertained by Field emission scanning electron microscopy (FESEM) analysis and were found to be 6.18 and 200.28 μm, respectively, as shown in Figs. 7.2(c) and (d). The tapered sections were marked to show the entrance and exit portions of the constricted passage (Fig. 7.2(e)), with a total length of 34.94 μm. The width of the channel was considered to be 7 μm for the entire study. The experimental setup was calibrated with a continuous flow of PBS for 30 min. Then 1×10^5 HeLa cells/ml were allowed to flow through the microchannel at an optimum flow rate of 30 μl/h. The cells moved through the constricted passage of the microchannel at high speed. The motion of the cells was video-graphed by Phantom MIRO-LAB320 High-speed camera at 50000-60000 fps using 20X objective in Leica DMI3000 M Microscope. It was observed that the HeLa cells appeared as singlets as well as loosely bound aggregates in the inlet reservoir. Figures 7.3(a), (b) and (c) illustrate that HeLa cells of approximate size 20 μm were deformed and elongated extensively while passing through the constriction of width 7 μm. Figure 7.3(a) (i-vi) shows time-lapse movement of a single HeLa cell through the constricted passage. Figure 7.3(a) (i-ii) show that the cells were squeezed slowly and then entered

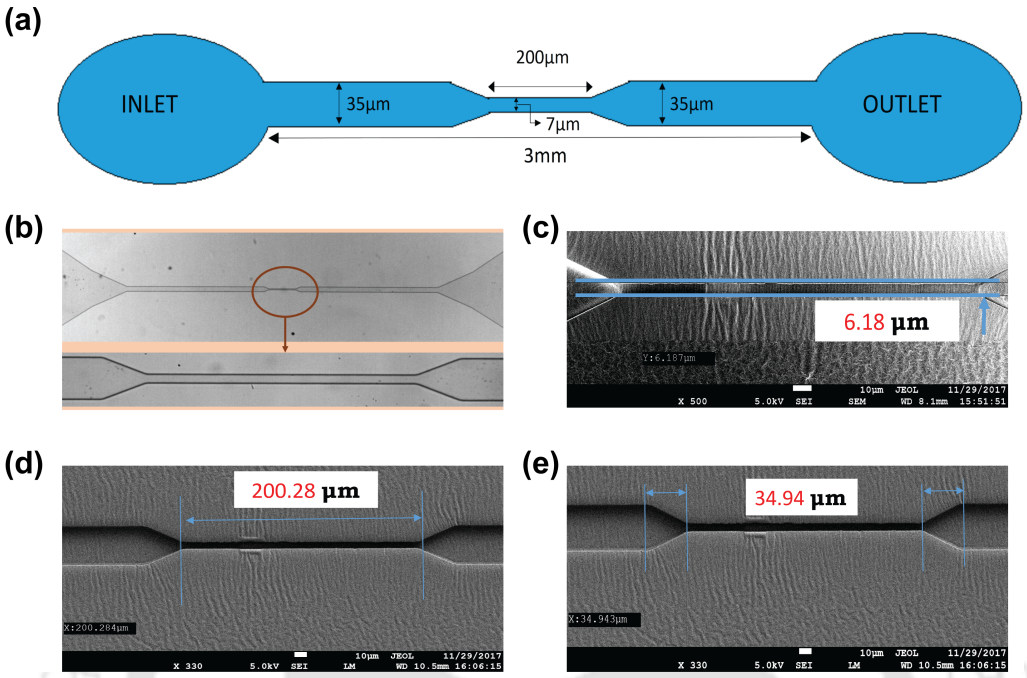

Figure 7.2: Design and characterization of the microchannel. (a) Design of the microchannel; (b) Microscopic view of the microchannel with a magnified view of the constricted section; (c) FESEM analysis of the width of the constricted passage; (d) FESEM analysis of the length of the constricted passage; (e) FESEM analysis of the length of the tapered section on either side of the constricted section.

the constriction. Similarly, enhanced deformation and elongation of the cells were observed in Fig. 7.3(a) (iii-iv) while moving inside the constriction. Once the cells had moved out of the constriction, they gradually returned back to shape, as shown in Fig. 7.3(a) (v). Finally, the cells moved further downstream of the channel and almost regained the original shape, as shown in Fig. 7.3(a) (vi). Movement of three HeLa cells through the constricted portion of the channel is shown in Fig. 7.3(b) (i-vi), where the cells entered one at a time and passed through the constriction in a moving queue. The movement of aggregated HeLa cells through the constricted channel was also recorded and is shown in Fig. 7.3(c) (i-viii). It was observed that many cells were aggregated and connected with each other. However, the cells underwent continuous reorientation and rearrangement while entering the constriction and in this continuous process, the cells got detached from each other. As a result, many cells appeared to be disconnected or loosely bound in the entry region,

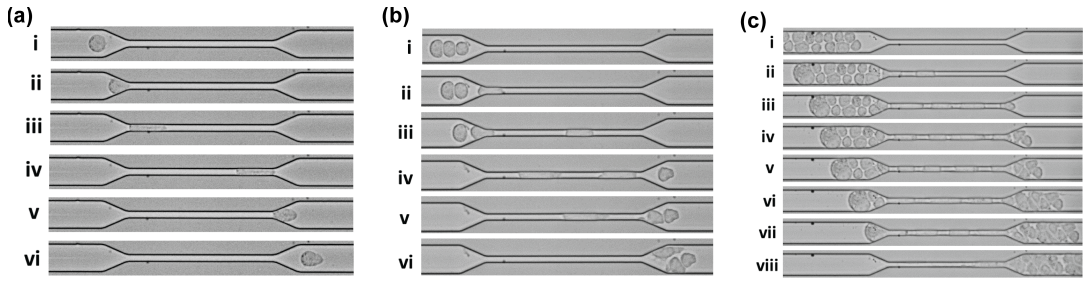

Figure 7.3: High-speed camera imaging of the migration of HeLa cells through the constricted portion of the microchannel. (a) Motion of a single cell: (i) a single drop approaching the constriction, (ii) cell entering the constriction, (iii) and (iv) cell moving inside the constriction, (v) cell squeezing out of the constriction and (vi) cell flowing outside the constriction; (b) Motion of three cells: (i) three cells approaching the constriction, (ii) and (iii) cells entering the constriction one by one, (iv) and (v) cells travelling inside the constriction and moving out one by one and (vi) cells flowing outside the constriction; (c) Motion of a cluster of cells: (i) cluster of cells approaching the constriction, (ii) and (iii) cells entering the constriction in a queue and traveling through it and (iv)-(viii) cells entering through the constriction and moving out one by one to re-form the cluster.

whereas they aggregated again after leaving the constricted portion.

7.3.2 Estimation of flow parameters of a single HeLa cell

The dynamics of motion and deformation of HeLa cells through a constricted channel were analysed from the movement of single cells of different sizes (17-30 μm). Still images were obtained from the recorded videos at the required time frames. Image J software was used for image processing, which enabled us to measure the diameter and length of the cells. The scale for measurement was set from the known dimensions of the channel. Physical parameters, such as entry time, transit velocity and elongation index, of a single HeLa cell were calculated based on the positioning of a cell in differentsections of the microchannel, as portrayed in Fig. 7.4(a). The domain of interest was divided into three sections: Entry, Transit and Exit regions. The Entry and Exit regions were subdivided into Entry regions I and II and Exit

regions I and II, respectively. At the beginning of Entry region I, the time (t) and

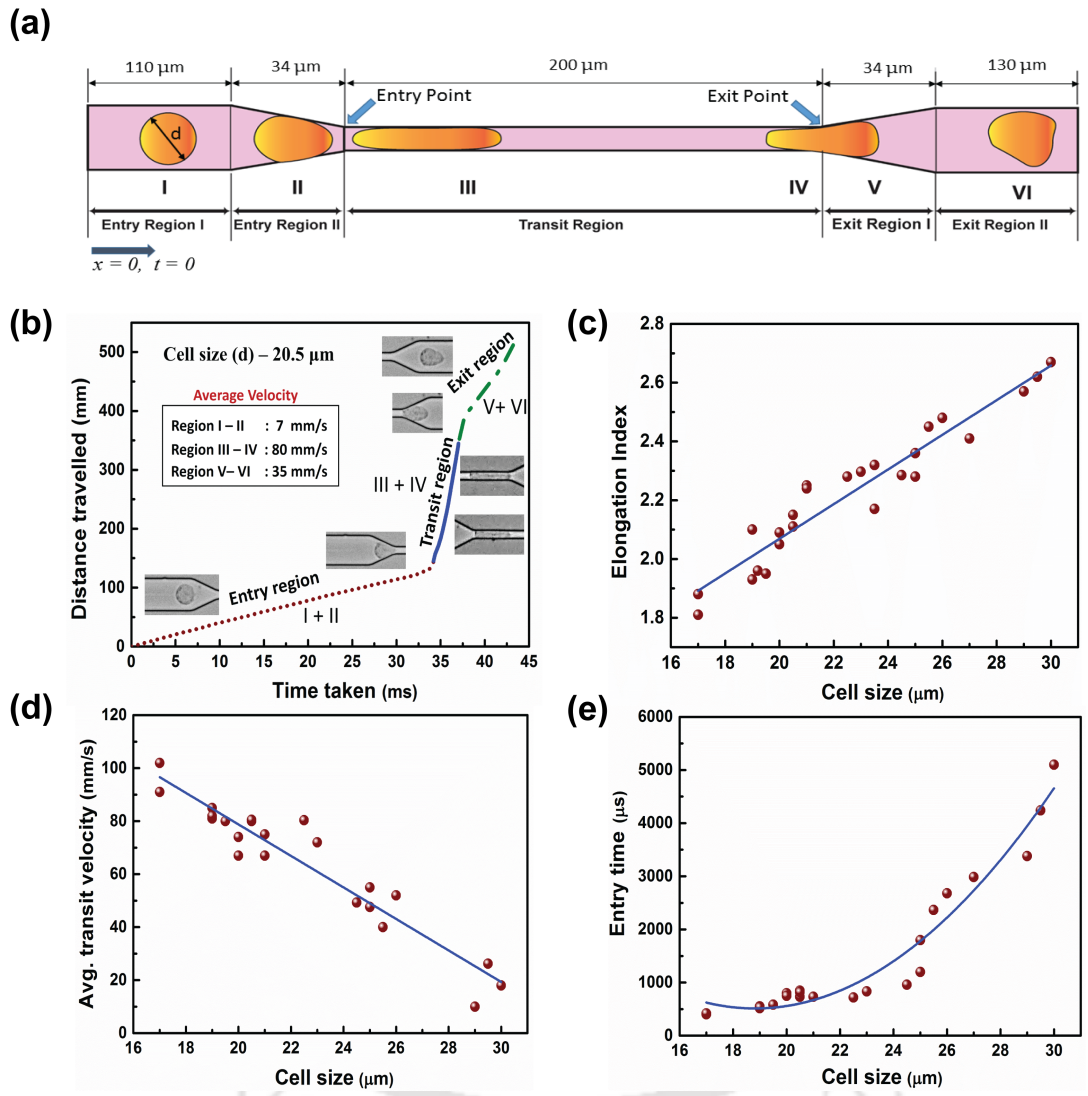

Figure 7.4: Movement of single cells in the microchannel. (a) Schematic representation of the motion of a single cell through different sections of the constricted channel. (b) Motion of a single cell of diameter 20.5 μm. (c), (d), (e) Elongation index, transit velocity and entry time, respectively, of single cells with diameters ranging from 17 to 30 μm.

distance (x) travelled by a cell were taken as $t = 0$ and $x = 0$. Entry region I was 110 μm long and 35 μm wide, where cells were found to retain their original shapes. Subsequently, the cells entered the converging section of length 34 μm denoted Entry

region II. The cells were mostly deformed in this region and prepared to enter the constriction ahead. Next, the cells moved to the Transit region, with a length of 200 μm and a width of 7 μm. The cell deformed substantially in this region, undergoing extensive elongation. They then moved out to the Exit region I of length 34 μm, which was a diverging section where the cells tried to recover their shape. In Exit region II, with a length of 130 μm and a width 35 μm, the cells continued to regain a circular shape while traversing downstream. The different positions of the cell are marked I, II, III, IV, V and VI, as shown in Fig. 7.4(a). Figure 7.4(b) shows the dynamics of a single cell of diameter 20.5 μm traversing through the different regions. The slope obtained from the distance traveled versus time graph revealed that the cell moved very slowly in the Entry region, where it approached the constriction and squeezed itself to enter it. The slope was very steep in the transit region, where the cell became elongated and moved with a high velocity. In the Exit region, the cells again slowed down while trying to retrieve their shape. The average cell velocity was calculated to be 4, 70 and 26 mm/s in the Entry, Transit and Exit regions, respectively. The deformation, velocity and entry time of the cells were calculated considering the diameter of cells ranging from 17 to 30 μm. Figures 7.4(c), (d) and (e) show the scatter plots for the different parameters using cells of varied sizes. The best fitted curves for the data points in the graphs are depicted by the blue lines. As the cells became elongated and deformed on entering the constricted channel, the elongation index of the cells was measured with respect to the original diameter and is given by-

$$\text{Elongation index} = l/d$$

where, l = maximum length of the cell in the microchannel and

d = original diameter of the cell.

Figure 7.4(c) shows that the deformation and elongation of large cells were greater than those of small cells while transiting through the constriction. It was observed in Fig. 7.4(d), based on the calculation of the transit velocity that a small cell passed through the constricted passage much faster than a large cell. The time taken by the HeLa cells to enter the constriction is shown in Fig. 7.4(e). It was noted that large cells took longer time than small cells to squeeze and accommodate themselves in the constricted passage.

7.3.3 Assessment of cell viability

It was important to explore the survival ability and mortality rate of the cells as they passed through the 7 μm constricted portion of the microchannel to address stimulated metastatic flow. Representative images after AO/EtBr dual staining are shown in Fig. 7.5, for cells in different sections of the constricted microchannel. It is evident from Fig. 7.5(a) that the cells were live and stained green, with hardly any dead cell (visible in red), in the Inlet section of the channel. Figure 7.5(b) shows live cells entering the channel from the inlet, and Fig. 7.5(c) shows a green deformed live cell that had just entered the constricted portion. From Fig. 7.5(d), it

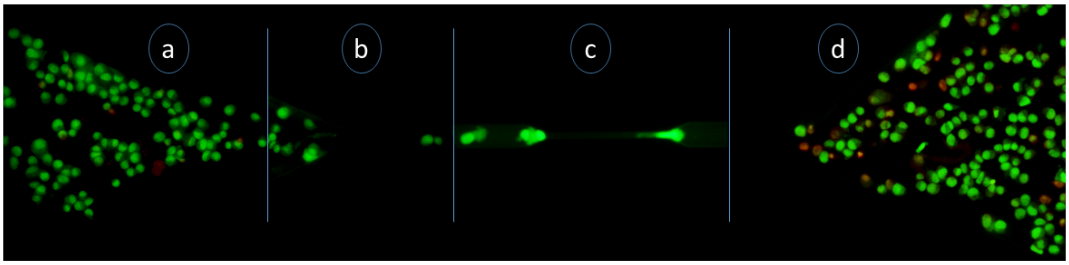

Figure 7.5: Representative images of AO/EtBr dual staining in different sections of the channel. (a) Live cells in the inlet section (with some debris); (b) Live cells entering the channel from the inlet; (c) A live cell moving in the constricted portion of the channel; and (d) Live and dead cells in the outlet section.

is observed that, although the number of dead cells increased in the Outlet section, a significant population of live cells (around 50 %) also existed. From this experiment, it was inferred that a portion of HeLa cells died during extensive deformation and elongation, but a moderate fraction of HeLa cells still retrieved their original shape and remained alive even after passing through the constriction. Such a population of live cells could represent the survival of metastatic cancer cells in harsh circulating conditions through microcapillaries in the human body. The accumulation of a high population of dead cells (stained red) at the outlet was possibly due to extensive deformation of cells leading to membrane compromisation while passing through the constricted channel.

7.3.4 Evaluation of viability (HeLa cells) by the trypan blue method

Live or dead cells were also analysed using the trypan blue dye exclusion assay: live and healthy cells were unstained or excluded from dye, whereas dead or membrane-compromised cells appeared blue due to trypan blue retention. The stained cells

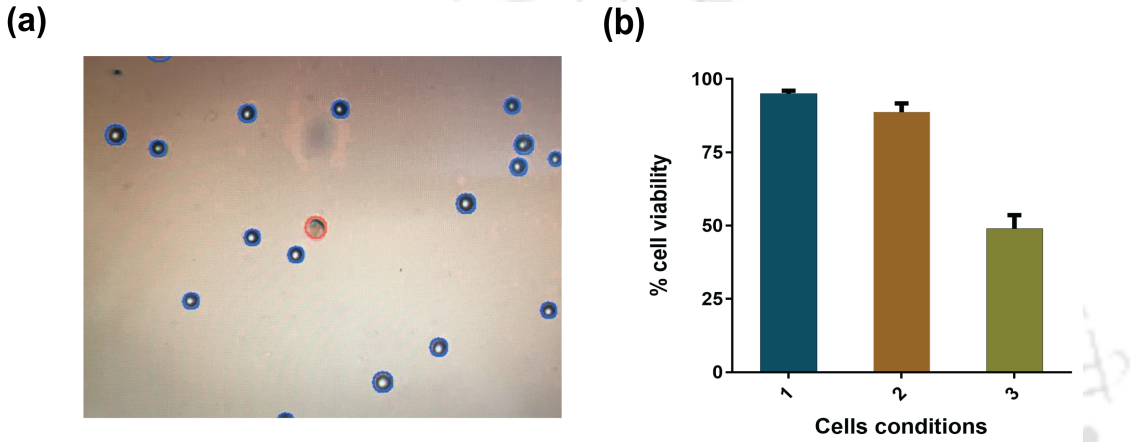

Figure 7.6: Viability of HeLa cells passing through the constricted channel. (a) Image of stained cells obtained from the Countess automated cell counter; (b) Comparison of percentage of cells still viable after passing through the constriction with the initial conditions and with cells maintained in the same environment for same period of time but not passed through the constriction. Cell condition 1 refers to the initial cells, cell condition 2 refers to mock experimental control cells without passing through the channel and cell condition 3 refers to the cells collected from the outlet of the constricted channel.

were analysed in the cell counting device and the number of live and dead cells were calculated using the Countess automated cell counter. To study the viability of the cells passing through constriction, adequate number of cells were collected from the outlet of the channel, which consisted of singlets as well as aggregates. Figure 7.6(a) illustrates the stained cells obtained from the Countess automated cell counter, showing live and dead cells. The graphical representation of the results is presented in Fig. 7.6(b).

The results shown in Fig. 7.6(b) for viability index were obtained from three

independent set of experiments. It was observed from the trypan blue dye exclusion assay that the initial conditions of the HeLa cells (before entering the constricted channel) were such that 95% of the cells were alive. When the cells suspended in the medium were allowed to pass through the constricted channel, around 50% of the cells retained their properties well and were alive. This corroborates the previous fluorescence-based study and gives a quantitative idea about the viability of the cells.

7.3.5 Metastatic profile

The experimental evidences confirmed the ability of HeLa cells to change morphology by deformation for crossing a 7 μm constriction and remained mostly alive. Further,

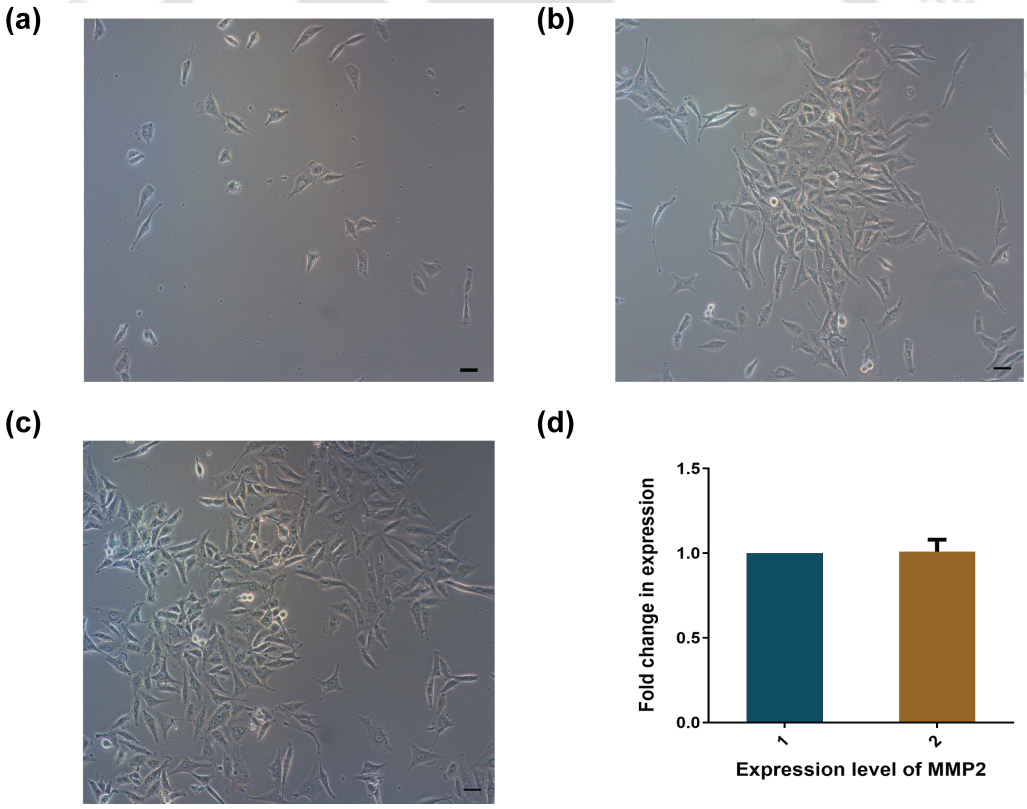

Figure 7.7: Metastatic profile of HeLa cells. Microscopic images of the cells collected from the outlet of the constricted channel and regrown in a cell culture dish for (a) 12, (b) 48 and (c) 72 h; and (d) representation of expression level of MMP2. Bar = 50 μm.

HeLa cells that accumulated at the outlet were collected and allowed to adhere to a culture disc to access the metastatic profile. Figure 7.7(a) depicts the adherence of cells, collected from the outlet, by 12 h. The cells started to divide and formed colonies (Fig. 7.7(b)) by 48 h, and became confluent at 72 h (Fig. 7.7(c)). The sequence of images (Fig. 7.7(a)-(c)) indicates the capability of HeLa to regrow and to form colonies even after passing through a harsh constricted passage. In the second line of investigation, the expression of the protein MMP2, involved in the degradation of the matrix enabling cells to be released into the bloodstream [183], was evaluated. In HeLa cells, the expression of MMP2 protein is considerably higher than in non-cancerous cells [184]. Hence qPCR was performed on the cDNA obtained from the total RNA of HeLa cells grown for 72 h after collection from the inlet and outlet of the setup. The qPCR (Fig. 7.7(d)) showed that the expression of MMP2 under both conditions remained unaltered. The results shown in Fig. 7.7(d) were accumulated from three independent set of experiments. Such fascinating results confirmed that the cells hardly lost any virulence and retained their capability to adhere, forming colonies that are reminiscent of CTC-like behavior.

7.4 Summary

This study investigates the flow dynamics of HeLa cells through a constricted microchannel. The main objective of the study was to mimic a situation to visualize how the cancer cells migrate from one part of the body to another part via blood capillaries. We intended to observe how the cells being larger in size than capillaries move through it. For the very purpose a microchannel having converging and diverging section with a 7 μm constriction had been fabricated using PDMS. Under experimental conditions, the cells deformed extensively in order to pass through the channel, allowing quantification of several physical parameters such as entry time, transit velocity and elongation index along with many other biological parameters. Morphological identification of live and apoptotic cells were performed by dual staining with acridine orange (AO)/ethidium bromide (EtBr) which gave a qualitative conclusion that due to constriction some cells died but around 50% cells retained all their physical properties and were potent enough for metastasis. The trypan blue dye exclusion assay gave a quantitative result and further reconfirmed the cell viability after passing through the constriction. The motion of aggregated HeLa

cells showed that they not only deform but reorient themselves and undergo proper sequencing to pass through the constricted passage.

Chapter 8

Conclusions and Scope for Further Studies

8.1 Conclusions

Investigations on motion and deformation of deformable drops and cancer cells through microchannels have been done by solving four interrelated research problems, addressed in the present thesis. Validations for the numerical solution are presented before proceeding with a detailed parametric study. In the first problem we performed numerical simulations of a neutrally buoyant droplet migrating in a cylindrical tube in the creeping flow regime using an in-house code, developed based on CLSVOF method. The axisymmetric Navier-Stokes and continuity equations were solved to determine the dynamics of a droplet migrating in a capillary tube with an imposed fully-developed flow at the inlet of the tube. In the context of physiological flows, the parameters (droplet size and capillary diameter) considered are relevant for the motion of red blood cells in arterioles, the motion of artificial capsules in industrial applications related to food and polymer processings, and two phase flows in a porous media, to name a few. The next problem focused in understanding the phenomenon of cross-stream migration of a drop in a two-dimensional channel, subjected to different initial off center positions of the drop. The Navier-Stokes equations coupled with electric force terms and continuity equation are solved to study droplet migration in a channel with fully-developed flow at the inlet, with and without the influence of an electric field. The numerical

simulations are performed using *Gerris* that implements VOF method to capture the deformable interfaces. The third study investigates the influence of an external electric field on the deformation and orientation of a drop in a shear flow. The simulations are performed in a two-dimensional framework and the coupled electro-hydrodynamic equations are solved using *Gerris*. The volume-of-fluid method has been deployed for the evolution of the interface considering both the fluids as either perfect dielectrics or leaky dielectrics. Finally, in the last problem of interest, we extended our understanding of motion and deformation of deformable drops through microchannels to understand the dynamics of the cancer cells in constricted microchannels. The viability and metastaic potency of the cancer cells after passing through the constrictions was examined by performing in-vitro experiments analyzing several biological assays. Some of the important findings from each of these investigations that deserve mention, are stated below.

8.1.1 Migration of a droplet in a cylindrical tube in the creeping flow regime

A parametric study is conducted by varying the ratio of droplet radius to the tube radius, capillary number and viscosity ratio between the droplet and the surrounding fluid injected at the inlet of the tube. First, we focused on the dynamics of unbroken droplets (small droplets) and found that for small droplets, increasing the size of the droplet decreases the droplet velocity, owing to increased deformability and the influence of the close proximity with the wall. For very small droplets, the drop velocity approaches the maximum velocity of the surrounding fluid flowing in the tube. Then, we investigated the effect of viscosity ratio (λ) and capillary number (Ca) on the droplet dynamics by fixing the droplet size to 0.7 times of channel radius ($a = 0.7$) . We found that increasing Ca increases the deformation and velocity of the droplet. For Ca ≈ 1 and $\lambda = 0.1$, an indentation is formed at the rear end of the drop, which is apprehended to grow further or disappear depending on the flow conditions. It is observed that with the increase in viscosity ratio, the drop deforms more and endures more resistance to the flow, thereby decreasing its velocity. We found that for a fixed value of Ca, the drop deformation increases with the increase in λ, such that the length of the drop increases and the width of the drop decreases, which in turn increases the thickness of the fluid film surrounding

the droplet. We then performed numerical investigations to understand the physics involving disintegrating droplets migrating inside the tube. By keeping the viscosity ratio and capillary number fixed as 0.1 and 1, respectively, droplet size is varied from $a = 0.7$ to 0.9. We observed that when the drop size is comparable to the tube diameter ($a = 0.9$), the tendency of the drop to break into smaller droplets increases. For $a = 0.8$, we observed that the daughter droplets merge back to the main droplet at the later times. The merged droplet then traverses with a steady shape. On the other hand, the drop with $a = 0.7$, deforms initially and develops an indentation at the trailing edge. But, this indentation dies down and the drop attains a steady shape after some time without breaking up. As we observed that the droplet with size comparable to the tube diameter ($a = 0.9$) reveals interesting physics of breakup, we investigated the effect of viscosity ratio for this droplet. We noticed that low viscosity drops breakup due to a re-entrant jet formed at the rear end, which gradually penetrates carrying the external fluid into the drop. In the case of more viscous drops a travelling capillary wave instability develops, which breaks the drop into daughter droplets. We found that as the drop viscosity increases, the drop undergoes more deformation and several daughter droplets are formed. The phenomenon of Ostwald ripening is also observed in this process. Finally, we determined the critical value of the capillary number beyond which a drop first breaks, for different droplet sizes and viscosity ratios.

8.1.2 Cross stream migration of drops suspended in Poiseuille flow in the presence of an electric field

For a drop traversing in a Poiseuille flow at a very low Reynolds number, the effects of the initial position of the drop, drop size, the capillary number and the viscosity ratio on its motion and deformation are thoroughly studied. It is observed that when a drop of size $a^* = 0.6$ is placed at different initial positions in the flow field for $\mathrm{Ca} = 0.7$ and $\lambda = 1.0$, the drop gradually migrates towards the centerline of the channel and eventually takes a steady lateral position. The initial y_c position was varied between -0.15 and 0.15. To understand the effect of drop size on cross stream migration, we considered drops of sizes varying from $a^* = 0.3$ to 0.65 for the same flow condition ($\mathrm{Ca} = 0.7$ and $\lambda = 1.0$). For the drops that are released from an initial off center position, $y_c = -0.15$, it is observed that larger drops move more slowly in

the channel as compared to smaller drops but the lateral migration phenomenon is better exhibited by the larger drops. Drops of size $a^* = 0.3$ and 0.4 exhibit very little cross migration phenomenon. From these studies (effect of initial position and size of the droplet), it is evident that the migration phenomenon of moderate size drops is quite interesting. Therefore, for the rest of the investigations the drop size is fixed at $a^* = 0.4$ and the initial off-center position is fixed at $y_c = -0.15$. An attempt has been made to understand the factors that enhance cross-stream migration. The effect of the capillary number on drop migration is studied by considering a drop of size $a^* = 0.4$ placed at $y_c = -0.15$ for $\lambda = 1$. The capillary number is varied between Ca = 0.3 and 1.3 and it is observed that with the increase in Ca the drop migration increases. The effect of viscosity ratio on the drop migration is studied by varying λ between 0.01 and 2.5. This study concluded that with the increase in viscosity ratio the drop migration decreases. In order to understand drop migration in a Poiseuille flow under the influence of external electric field, we considered a drop of size, $a^* = 0.4$ placed at $y_c = -0.15$ for Ca = 0.7 and $\lambda = 1$. Both dielectric and leaky dielectric fluids are taken into consideration in this study. In the case of dielectric fluids, the effects of permittivity ratio (S) and the strength of electric field (E) on drop migration are studied. It is observed that for a drop fluid having high permittivity compared to the suspending fluid, the drop deforms highly and oscillates around its mean position. When the electric field strength is increased from $E = 5$ to 20 for a fixed permittivity ratio, it is observed that the cross stream migration increases and the drops become stretched and elongated in the direction of the electric field. In the case of leaky dielectric fluids, the electric field strength is varied from $E = 1$ to 5 and two sets of fluid combinations are considered. In one case the permittivity of the drop-fluid is less than that of the suspending medium while the drop-fluid is more conducting than the suspending fluid ($S = 0.5$ and $R = 2$) and in the other case, the conditions are reversed ($S = 2$ and $R = 0.5$). It is observed that a more conducting drop tends to migrate towards the channel centerline and the cross migration increases with the increase in E while a less conducting drop tends to settle down at a lateral position somewhere near the initial off-center position. An interesting phenomenon is revealed in the case of a less conducting drops under a stronger electric field wherein the drops exhibit rotation together with translation.

8.1.3 Influence of electric field on deformation of a drop in shear flow

The influence of an external electric field on the deformation and orientation of a drop in shear flow is an important area of drop dynamics. The simulations reveal that under the influence of an electric field, the deformation of the drop can be either enhanced or reduced for dielectric fluids, depending on the magnitude of permittivity ratio S. The polarization force acting at the interface is directed from the medium of higher permittivity to lower permittivity. The nature of polarization forces are compressive for $S < 1.0$ and tensile in the case of $S > 1.0$. The disparity in the electrical permittivity across the interface influences the applied electric field thereby leading to spatial variation of the field intensity. The iso-potential lines converge inside a drop with lower permittivity, whereas, a diverging behavior is observed for the iso-potential lines in the case of a drop with higher permittivity than the surrounding fluid. Systems of leaky dielectric fluids have been studied too and in particular two cases have been computed in detail. The first system (System A) consists of a drop which is less conducting but has higher permittivity than the surrounding fluid. In the second system (System B), the drop is more conducting but has a lower permittivity than the suspending fluid. It is observed that the deformation of drops for System A increases with the applied electric field strength E whereas, for system B, the deformation is suppressed with increasing E, albeit in a subtle way. The reason for the contrasting behavior of systems A and B lies in the opposing nature of charge accumulation at the drop interface. The Coulombic forces dominate over the polarization forces in the case of leaky dielectric fluids. The contradictory nature of charge accumulation for systems A and B results in the development of compressive Coulombic forces for system A and tensile Coulombic forces for system B. The conductivity ratio R decides the nature of charge accumulation at the upper and lower portions of the drop thereby altering the droplet deformation and orientation under the application of the external electric field.

8.1.4 Understanding flow dynamics, viability and metastatic potency of cervical cancer (HeLa) cells through constricted microchannel

As enumerated earlier, in the experimental work, flow dynamics and survival ability of cancer cells transiting through microcapillaries that mimic the microvascular environment has been elucidated. PDMS microchannel of minimum constricted width of 7 μm for a distance of 200 μm in a total length of 3 mm was fabricated that possessed close analogy in terms of dimensions with human capillaries (width in the range of 5 - 10 μm). The FESEM characterization of the channel ensured that the fabricated channel actually possessed the dimensions as per our design. The remarkable ability of singlets and even aggregated cluster of HeLa cells to transit through capillary sized micro-constriction was witnessed by capturing videos through high speed camera. It was observed that the key to aggregated HeLa cells transit through narrow capillaries could be due to their ability to rapidly unfold into single file chains while entering into the constriction, which significantly reduces their overall resistance to flow. The associated HeLa cells segregated as individual cells in tandem while traversing through the microcapillary and reorganized themselves to aggregate again after exit. The high speed videographs were deconvoluted to obtain still images and crucial parameters like cell elongation index, average transit velocity and entry time of the single cells passing through constriction were calculated, to understand the dynamics of HeLa cell motility. This detailed investigation of the hydrodynamic parameters of HeLa cells of varied sizes helped us in finding a common trend in which the cells deform and move inside the constriction with respect to their sizes. The values of the different hydrodynamic parameters obtained in this study correspond to the optimized flow rate of 30 l/h for our experiments. The extensive change in morphology of the cells witnessed while transiting through constriction raised our inquisitiveness to find out whether the cells that exit through the constriction could retain their metastatic potency. Reasonable viability of the cells after passage through the constriction, determined by dual AO/ EtBr staining, was substantiated by trypan blue dye exclusion assay that confirmed the retention of around 50% viable HeLa cell population at the outlet. Data from the mentioned experiments suggested that the HeLa cells, even after passing through the constriction, remained viable to form further tumors at extremities of the body. In other

set of experiments, we successfully collected the cells from the outlet of the constricted channel and grew the cells in cell culture. In 48 h of cell culture, the cells started to divide and formed colonies and by the end of the 72 h they achieved confluency. This experiment assured that, although most of the cells died during extensive deformation and elongation, yet a substantial population of live cells was found to exist, which retained the capability of portraying the phenomenon of metastasis further. Moreover, Real-time measurement of MMP2 expression to determine important metastatic biomarker of HeLa cells opened up a new paradigm to understand the possible dynamics of cancer cells to spread metastasis by traversing through microcapillaries in human body.

8.2 Scope for further studies

More understanding on the motion and deformation of deformable drops and cancer cells through microchannels is needed for variety of applications pertaining to microfluidics and nanofluidics. The current investigations identify a few potential research problems for the future investigations.

1. The dynamics of a non-Newtonian drop in a Newtonian/non-Newtonian flowing fluid can be studied to add physiological significance to the investigation. In this thesis, all the investigation on drop dynamics have been carried out considering both the drop as well as the suspending medium as Newtonian fluids. An attempt towards studying the dynamics of a viscoelastic droplet in the presence of surfactants is also desirable. In food and process industries, various polymeric compounds are used. These compounds generally display non-Newtonian behaviour. In addition, a physical system comprising of a viscoelastic droplet along with bulk-insoluble surfactants can be used as a crude model to mimic the dynamics of a biological cell. This numerical development can be implemented to simulate the motion of cancer cells and further investigate the phenomenon of metastasis.

2. All the numerical problems dealt in this thesis consider the study of isolated droplets. The interactions between two or more droplets have not been attempted. In concentrated emulsions, such an analysis will be more useful. Hence an analysis on droplet interactions and collisions inside microchan-

nels can be aimed at. Also, a detailed investigation on suspending fluid and drop/cell interaction in microchannel or tube would reveal interesting physics.

3. The effect of surfactants on the migration and drop break up can be studied. Also, the droplet interactions can be investigated by considering a non-uniform surfactant distribution. The transition capillary number for deformation and breakup can be obtained by a more detailed theoretical analysis.

4. In the present thesis, the influences of only direct current electric field on the drop deformation and cross-stream migration have been investigated. The present study can be further enriched by analyzing the effect of alternating current electric field on the droplet dynamics.

5. The study of cancer cells can be broadened by studying the nature and behaviour of variety of cancer cells. In the present thesis, only HeLa cells have been considered. The results obtained using HeLa cells can be compared with other cell lines to draw a more accurate conclusion pertaining to the deformability, viability and metastatic potency of different cell lines.

6. The condition of the nucleus of the cell while the drop traverses in the constricted channels undergoing deformation, need to be observed. During extreme elongation of the drop, the nucleus may break. The nucleus contains the majority of the cell's genetic material. For the cell to be viable and metastatically potent, the nucleus has to remain intact. Hence, the phenomenon of nucleus deformation, breakup and merging need to be investigated.

References

[1] Faltas B. (2012) 'Cornering metastases: therapeutic targeting of circulating tumor cells and stem cells', *Frontiers in Oncology*, vol. 2, p. 68.

[2] Olbricht W.L. and Kung D.M. (1992) 'The deformation and breakup of liquid drops in low reynolds number flow through a capillary', *Physics of Fluids*, vol. 4, pp. 1347–1354.

[3] Tsai T.M. and Miksis M.J. (1994) 'Dynamics of a drop in a constricted capillary tube', *Journal of Fluid Mechanics*, vol. 274, pp. 197–217.

[4] Olbricht W.L. (1996) 'Pore-scale prototypes of multiphase flow in porous media', *Annual Review of Fluid Mechanics*, vol. 28, pp. 187–213.

[5] Ho B.P. and Leal L.G. (1975) 'The creeping motion of liquid drops through a circular tube of comparable diameter', *Journal of Fluid Mechanics*, vol. 71, pp. 361–383.

[6] Martinez M.J. and Udell K.S. (1990) 'Axisymmetric creeping motion of drops through circular tubes', *Journal of Fluid Mechanics*, vol. 210, pp. 565–591.

[7] Hua H., Shin J., and Kim J. (2014) 'Dynamics of a compound droplet in shear flow', *International Journal of Heat and Fluid Flow*, vol. 50, pp. 63–71.

[8] Feng J.Q. (2002) 'A 2d electrohydrodynamic model for electrorotation of fluid drops', *Journal of Colloid and Interface Science*, vol. 246, pp. 112–121.

[9] Teh S.Y., Lin R., Hung L.H., and Lee A.P. (2008) 'Droplet microfluidics', *Lab on a Chip*, vol. 8, pp. 198–220.

[10] Burns M.A., Johnson B.N., Brahmasandra S.N., Handique K., Webster J.R., Krishnan M., Sammarco T.S., Man P.M., Jones D., Heldsinger D., et al. (1998) 'An integrated nanoliter dna analysis device', *Science*, vol. 282, pp. 484–487.

[11] Tokeshi M., Minagawa T., Uchiyama K., Hibara A., Sato K., Hisamoto H., and Kitamori T. (2002) 'Continuous-flow chemical processing on a microchip by combining microunit operations and a multiphase flow network', *Analytical Chemistry*, vol. 74, pp. 1565–1571.

[12] Anna S.L., Bontoux N., and Stone H.A. (2003) 'Formation of dispersions using flow focusing in microchannels', *Applied Physics Letters*, vol. 82, pp. 364–366.

[13] Skommer J., Akagi J., Takeda K., Fujimura Y., Khoshmanesh K., and Wlodkowic D. (2013) 'Multiparameter lab-on-a-chip flow cytometry of the cellcycle', *Biosensors and Bioelectronics*, vol. 42, pp. 586 – 591.

[14] Jensen K.F. (2001) 'Microreaction engineering-is small better?', *Chemical Engineering Science*, vol. 56, pp. 293–303.

[15] Sibillo V., Pasquariello G., Simeone M., Cristini V., and Guido S. (2006) 'Drop deformation in microconfined shear flow', *Physical Review Letters*, vol. 97, p. 054502.

[16] Kumar V., Paraschivoiu M., and Nigam K. (2011) 'Single-phase fluid flow and mixing in microchannels', *Chemical Engineering Science*, vol. 66, pp. 1329 – 1373.

[17] Song H., Tice J.D., and Ismagilov R.F. (2003) 'A microfluidic system for controlling reaction networks in time', *Angewandte Chemie International Edition*, vol. 42, pp. 768–772.

[18] Baroud C.N., Gallaire F., and Dangla R. (2010) 'Dynamics of microfluidic droplets', *Lab on a Chip*, vol. 10, pp. 2032–2045.

[19] Garstecki P., Fuerstman M.J., Stone H.A., and Whitesides G.M. (2006) 'Formation of droplets and bubbles in a microfluidic t-junctionscaling and mechanism of break-up', *Lab on a Chip*, vol. 6, pp. 437–446.

[20] Maehlmann S. and Papageorgiou D.T. (2009) 'Numerical study of electric field effects on the deformation of two-dimensional liquid drops in simple shear flow at arbitrary reynolds number', *Journal of Fluid Mechanics*, vol. 626, pp. 367–393.

[21] Borthakur M.P., Biswas G., and Bandyopadhyay D. (2018) 'Dynamics of drop formation from submerged orifices under the influence of electric field', *Physics of Fluids*, vol. 30, p. 122104.

[22] López-Herrera J., Popinet S., and Herrada M. (2011) 'A charge-conservative approach for simulating electrohydrodynamic two-phase flows using volume-of-fluid', *Journal of Computational Physics*, vol. 230, pp. 1939–1955.

[23] Basaran O.A. (2002) 'Small-scale free surface flows with breakup: Drop formation and emerging applications', *AIChE Journal*, vol. 48, pp. 1842–1848.

[24] Wu Y. and Clark R.L. (2008) 'Electrohydrodynamic atomization: a versatile process for preparing materials for biomedical applications', *Journal of Biomaterials Science, Polymer Edition*, vol. 19, pp. 573–601.

[25] Velev O.D., Prevo B.G., and Bhatt K.H. (2003) 'On-chip manipulation of free droplets', *Nature*, vol. 426, p. 515.

[26] Ha J.W. and Yang S.M. (2000) 'Deformation and breakup of newtonian and non-newtonian conducting drops in an electric field', *Journal of Fluid Mechanics*, vol. 405, pp. 131–156.

[27] O'Konski C.T. and Thacher Jr H.C. (1953) 'The distortion of aerosol droplets by an electric field', *The Journal of Physical Chemistry*, vol. 57, pp. 955–958.

[28] Lac E. and Homsy G. (2007) 'Axisymmetric deformation and stability of a viscous drop in a steady electric field', *Journal of Fluid Mechanics*, vol. 590, pp. 239–264.

[29] Sato H., Kaji N., Mochizuki T., and Mori Y.H. (2006) 'Behavior of oblately deformed droplets in an immiscible dielectric liquid under a steady and uniform electric field', *Physics of Fluids*, vol. 18, p. 127101.

[30] Tan S.H., Semin B., and Baret J.C. (2014) 'Microfluidic flow-focusing in ac electric fields', *Lab on a Chip*, vol. 14, pp. 1099–1106.

[31] Erkal J.L., Selimovic A., Gross B.C., Lockwood S.Y., Walton E.L., McNamara S., Martin R.S., and Spence D.M. (2014) '3d printed microfluidic devices with integrated versatile and reusable electrodes', *Lab on a Chip*, vol. 14, pp. 2023–2032.

[32] Kim S.J., Song Y.A., and Han J. (2010) 'Nanofluidic concentration devices for biomolecules utilizing ion concentration polarization: theory, fabrication, and applications', *Chemical Society Reviews*, vol. 39, pp. 912–922.

[33] Hong J., Edel J.B., et al. (2009) 'Micro-and nanofluidic systems for high-throughput biological screening', *Drug Discovery Today*, vol. 14, pp. 134–146.

[34] Warburg O. (1956) 'On the origin of cancer cells', *Science*, vol. 123, pp. 309–314.

[35] DeBerardinis R.J., Lum J.J., Hatzivassiliou G., and Thompson C.B. (2008) 'The biology of cancer: metabolic reprogramming fuels cell growth and proliferation', *Cell Metabolism*, vol. 7, pp. 11–20.

[36] Elledge S.J. (1996) 'Cell cycle checkpoints: preventing an identity crisis', *Science*, vol. 274, pp. 1664–1672.

[37] Schroeder A., Heller D.A., Winslow M.M., Dahlman J.E., Pratt G.W., Langer R., Jacks T., and Anderson D.G. (2012) 'Treating metastatic cancer with nanotechnology', *Nature Reviews Cancer*, vol. 12, p. 39.

[38] Oppenheimer S.B. (2006) 'Cellular basis of cancer metastasis: A review of fundamentals and new advances', *Acta Histochemica*, vol. 108, pp. 327–334.

[39] Leber M.F. and Efferth T. (2009) 'Molecular principles of cancer invasion and metastasis', *International Journal of Oncology*, vol. 34, pp. 881–895.

[40] Duffy M., McGowan P., and Gallagher W. (2008) 'Cancer invasion and metastasis: changing views', *The Journal of Pathology*, vol. 214, pp. 283–293.

[41] Chambers A.F., MacDonald I.C., Schmidt E.E., Koop S., Morris V.L., Khokha R., and Groom A.C. (1995) 'Steps in tumor metastasis: new concepts from intravital videomicroscopy', *Cancer and Metastasis Reviews*, vol. 14, pp. 279–301.

[42] Morris V., Schmidt E., MacDonald I., Groom A., and Chambers A. (1997) 'Sequential steps in hematogenous metastasis of cancer cells studied by in vivo videomicroscopy.', *Invasion & Metastasis*, vol. 17, pp. 281–296.

[43] O'Flaherty J.D., Gray S., Richard D., Fennell D., O'Leary J.J., Blackhall F.H., and O'Byrne K.J. (2012) 'Circulating tumour cells, their role in metastasis and their clinical utility in lung cancer', *Lung Cancer*, vol. 76, pp. 19–25.

[44] Miller M.C., Doyle G.V., and Terstappen L.W. (2010) 'Significance of circulating tumor cells detected by the cellsearch system in patients with metastatic breast colorectal and prostate cancer', *Journal of Oncology*, vol. 2010.

[45] Hirt C.W. and Nichols B.D. (1981) 'Volume of fluid (vof) method for the dynamics of free boundaries', *Journal of Computational Physics*, vol. 39, pp. 201–225.

[46] Youngs D.L., 'Time-dependent multi-material flow with large fluid distortion', in K. Morton and M.E. Baines, (Editors) 'Numerical Methods for Fluid Dynamics', (Academic Press, New York, 1982), pp. 273–285.

[47] Puckett E.G., Almgren A.S., Bell J.B., Marcus D.L., and Rider W.J. (1997) 'A high-order projection method for tracking fluid interfaces in variable density incompressible flows', *Journal of Computational Physics*, vol. 130, pp. 269 – 282.

[48] Osher S. and Sethian J.A. (1988) 'Fronts propagating with curvature-dependent speed: algorithms based on hamilton-jacobi formulations', *Journal of Computational Physics*, vol. 79, pp. 12–49.

[49] Sussman M. and Puckett E.G. (2000) 'A coupled level set and volume-of-fluid method for computing 3d and axisymmetric incompressible two-phase flows', *Journal of Computational Physics*, vol. 162, pp. 301–337.

[50] Son G. and Hur N. (2002) 'A coupled level set and volume-of-fluid method for the buoyancy-driven motion of fluid particles', *Numerical Heat Transfer, Part B: Fundamentals*, vol. 42, pp. 523–542.

[51] Wang Z., Yang J., Koo B., and Stern F. (2009) 'A coupled level set and volume-of-fluid method for sharp interface simulation of plunging breaking waves', *International Journal of Multiphase Flow*, vol. 35, pp. 227–246.

[52] Brackbill J.U., Kothe D.B., and Zemach C. (1992) 'A continuum method for modeling surface tension', *Journal of Computational Physics*, vol. 100, pp. 335–354.

[53] Harlow F.H. and Welch J.E. (1965) 'Numerical calculation of time-dependent viscous incompressible flow of fluid with free surface', *Physics of Fluids*, vol. 8, p. 2182.

[54] Strang G. (1968) 'On the construction and comparison of difference schemes', *SIAM Journal on Numerical Analysis*, vol. 5, pp. 506–517.

[55] Chang Y.C., Hou T.Y., Merriman B., and Osher S. (1996) 'A level set formulation of eulerian interface capturing methods for incompressible fluid flows', *Journal of Computational Physics*, vol. 124, pp. 449–464.

[56] Renardy Y. and Renardy M. (2002) 'Prost: a parabolic reconstruction of surface tension for the volume-of-fluid method', *Journal of Computational Physics*, vol. 183, pp. 400–421.

[57] Son G. (2003) 'Efficient implementation of a coupled level-set and volume-of-fluid method for three-dimensional incompressible two-phase flows', *Numerical Heat Transfer, Part B: Fundamentals*, vol. 43, pp. 549–565.

[58] Popinet S. (2003) 'Gerris: a tree-based adaptive solver for the incompressible euler equations in complex geometries', *Journal of Computational Physics*, vol. 190, pp. 572–600.

[59] Popinet S. (2009) 'An accurate adaptive solver for surface-tension-driven interfacial flows', *Journal of Computational Physics*, vol. 228, pp. 5838–5866.

[60] Ling Y., Fullana J.M., Popinet S., and Josserand C. (2016) 'Droplet migration in a hele–shaw cell: Effect of the lubrication film on the droplet dynamics', *Physics of Fluids*, vol. 28, p. 062001.

[61] Chen X., Xue C., Zhang L., Hu G., Jiang X., and Sun J. (2014) 'Inertial migration of deformable droplets in a microchannel', *Physics of Fluids*, vol. 26, p. 112003.

[62] Borthakur M.P., Biswas G., Bandyopadhyay D., and Sahu K.C. (2019) 'Dynamics of an arched liquid jet under the influence of gravity', *European Journal of Mechanics-B/Fluids*, vol. 74, pp. 1–9.

[63] Bell J.B., Colella P., and Glaz H.M. (1989) 'A second-order projection method for the incompressible navier-stokes equations', *Journal of Computational Physics*, vol. 85, pp. 257–283.

[64] Francois M.M., Cummins S.J., Dendy E.D., Kothe D.B., Sicilian J.M., and Williams M.W. (2006) 'A balanced-force algorithm for continuous and sharp

interfacial surface tension models within a volume tracking framework', *Journal of Computational Physics*, vol. 213, pp. 141–173.

[65] Cummins S.J., Francois M.M., and Kothe D.B. (2005) 'Estimating curvature from volume fractions', *Computers & Structures*, vol. 83, pp. 425–434.

[66] Rudman M. (1997) 'Volume-tracking methods for interfacial flow calculations', *International Journal for Numerical Methods in Fluids*, vol. 24, pp. 671–691.

[67] Popinet S. (2015) 'A quadtree-adaptive multigrid solver for the serre–green–naghdi equations', *Journal of Computational Physics*, vol. 302, pp. 336–358.

[68] Ferrera C., López-Herrera J., Herrada M., Montanero J., and Acero A. (2013) 'Dynamical behavior of electrified pendant drops', *Physics of Fluids*, vol. 25, p. 012104.

[69] Cimpeanu R., Papageorgiou D.T., and Petropoulos P.G. (2014) 'On the control and suppression of the rayleigh-taylor instability using electric fields', *Physics of Fluids*, vol. 26, p. 022105.

[70] Tortora G.J. and Derrickson B. (2012) 'The cardiovascular system: blood vessels and hemodynamics', *Principles of Anatomy and Physiology*, pp. 610–635.

[71] Hetsroni G., Haber S., and Wacholder E. (1970) 'The flow fields in and around a droplet moving axially within a tube', *Journal of Fluid Mechanics*, vol. 41, pp. 689–705.

[72] Brenner H. (1971) 'Pressure drop due to the motion of neutrally buoyant particles in duct flows. ii. spherical droplets and bubbles', *Industrial and Engineering Chemistry Fundamentals*, vol. 10, pp. 537–543.

[73] Bungay P.M. and Brenner H. (1973) 'Pressure drop due to the motion of neutrally buoyant particles in duct flows. iii. non-neutrally buoyant spherical droplets and bubbles', *Zeitschrift für Angewandte Mathematik und Mechanik*, vol. 53, pp. 187–192.

[74] Hyman W.A. and Skalak R. (1972) 'Viscous flow of a suspension of liquid drops in a cylindrical tube', *Applied Scientific Research*, vol. 26, pp. 27–52.

[75] Hyman W.A. and Skalak R. (1972) 'Non-newtonian behavior of a suspension of liquid drops in tube flow', *AIChE Journal*, vol. 18, pp. 149–154.

[76] Chan P.H. and Leal L.G. (1979) 'The motion of a deformable drop in a second-order fluid', *Journal of Fluid Mechanics*, vol. 92, pp. 131–170.

[77] Nadim A. and Stone H.A. (1991) 'The motion of small particles and droplets in quadratic flows', *Studies in Applied Mathematics*, vol. 85, pp. 53–73.

[78] Konda H., Tripathi M.K., and Sahu K.C. (2016) 'Bubble motion in a converging–diverging channel', *Journal of Fluids Engineering*, vol. 138, p. 064501.

[79] G. Segré and A. Silberberg (1961) 'Radial particle displacements in poiseuille flow of suspensions', *Nature*, vol. 189, pp. 209–210.

[80] Sutera S.P. and Hochmuth R.M. (1968) 'Large scale modeling of blood flow in the capillaries.', *Biorheology*, vol. 5, p. 45.

[81] Hochmuth R.M. and Sutera S.P. (1970) 'Spherical caps in low reynolds-number tube flow', *Chemical Engineering Science*, vol. 25, pp. 593–604.

[82] Prothero J.W. and Burton A.C. (1962) 'The physics of blood flow in capillaries: III. The pressure required to deform erythrocytes in acid-citrate-dextrose', *Biophysical Journal*, vol. 2, p. 213.

[83] Prothero J. and Burton A.C. (1961) 'The physics of blood flow in capillaries: I. the nature of the motion', *Biophysical Journal*, vol. 1, p. 565.

[84] Karnis A., Goldsmith H.L., and Mason S.G. (1963) 'Axial migration of particles in poiseuille flow', *Nature*, vol. 200, pp. 159–160.

[85] Zhou H. and Pozrikidis C. (1994) 'Pressure-driven flow of suspensions of liquid drops', *Physics of Fluids*, vol. 6, pp. 80–94.

[86] Khayat R.E., Luciani A., and Utracki L.A. (1997) 'Boundary-element analysis of planar drop deformation in confined flow. Part 1. Newtonian fluids', *Engineering Analysis with Boundary Elements*, vol. 19, pp. 279–289.

[87] Coulliette C. and Pozrikidis C. (1998) 'Motion of an array of drops through a cylindrical tube', *Journal of Fluid Mechanics*, vol. 358, pp. 1–28.

[88] Griggs A.J., Zinchenko A.Z., and Davis R.H. (2007) 'Low-Reynolds-number motion of a deformable drop between two parallel plane walls', *International Journal of Multiphase Flow*, vol. 33, pp. 182–206.

[89] Wang Y. and Dimitrakopoulos P. (2012) 'Low-Reynolds-number droplet motion in a square microfluidic channel', *Theoretical and Computational Fluid Dynamics*, vol. 26, pp. 361–379.

[90] Mortazavi S. and Tryggvason G. (2000) 'A numerical study of the motion of drops in poiseuille flow. Part 1. Lateral migration of one drop', *Journal of Fluid Mechanics*, vol. 411, pp. 325–350.

[91] Chakraborty I., Biswas G., and Ghoshdastidar P.S. (2013) 'A coupled level-set and volume-of-fluid method for the buoyant rise of gas bubbles in liquids', *International Journal of Heat and Mass Transfer*, vol. 58, pp. 240–259.

[92] Chakraborty I., Biswas G., and Ghoshdastidar P.S. (2011) 'Bubble generation in quiescent and co-flowing liquids', *International Journal of Heat and Mass Transfer*, vol. 54, pp. 4673–4688.

[93] Chakraborty I., Ray B., Biswas G., Durst F., Sharma A., and Ghoshdastidar P.S. (2009) 'Computational investigation on bubble detachment from submerged orifice in quiescent liquid under normal and reduced gravity', *Physics of Fluids*, vol. 21, p. 062103.

[94] Ray B., Biswas G., and Sharma A. (2010) 'Generation of secondary droplets in coalescence of a drop at a liquid-liquid interface', *Journal of Fluid Mechanics*, vol. 655, pp. 72–104.

[95] Ray B., Biswas G., and Sharma A. (2012) 'Bubble pinch-off and scaling during liquid drop impact on liquid pool', *Physics of Fluids*, vol. 24, p. 082108.

[96] Guido S. and Preziosi V. (2010) 'Droplet deformation under confined Poiseuille flow', *Advances in Colloid and Interface Science*, vol. 161, pp. 89–101.

[97] Taylor G. (1963) 'Cavitation of a viscous fluid in narrow passages', *Journal of Fluid Mechanics*, vol. 16, pp. 595–619.

[98] Bretherton F. (1961) 'The motion of long bubbles in tubes', *Journal of Fluid Mechanics*, vol. 10, pp. 166–188.

[99] Cherukumudi A., Klaseboer E., Khan S.A., and Manica R. (2015) 'Prediction of the shape and pressure drop of taylor bubbles in circular tubes', *Microfluidics and Nanofluidics*, vol. 19, pp. 1221–1233.

[100] Hill M.J.M. (1894) 'On a spherical vortex', *Philosophical Transactions of the Royal Society of London A: Mathematical, Physical and Engineering Sciences*, vol. 185, pp. 213–245.

[101] Lac E. and Sherwood J.D. (2009) 'Motion of a drop along the centreline of a capillary in a pressure-driven flow', *Journal of Fluid Mechanics*, vol. 640, pp. 27–54.

[102] Fraser R., Eisenklam P., Dombrowski N., and Hasson D. (1962) 'Drop formation from rapidly moving liquid sheets', *AIChE Journal*, vol. 8, pp. 672–680.

[103] Dombrowski N. and Johns W. (1963) 'The aerodynamic instability and disintegration of viscous liquid sheets', *Chemical Engineering Science*, vol. 18, pp. 203–214.

[104] Goldsmith H. and Mason S. (1961) 'Axial migration of particles in poiseuille flow', *Nature*, vol. 190, pp. 1095–1096.

[105] Ho B.P. and Leal L.G. (1974) 'Inertial migration of rigid spheres in two-dimensional unidirectional flows', *Journal of Fluid Mechanics*, vol. 65, pp. 365–400.

[106] Konda H., Tripathi M.K., and Sahu K.C. (2016) 'Bubble motion in a converging–diverging channel', *Journal of Fluids Engineering*, vol. 138, p. 064501.

[107] Nourbakhsh A. and Mortazavi S. (2010) 'A three-dimensional study of the motion of a drop in plane poiseuille flow at finite reynolds numbers', *Iranian Journal of Science and Technology Transaction B-Engineering*, vol. 34, pp. 179–196.

[108] Garton C. and Krasucki Z. (1964) 'Bubbles in insulating liquids: stability in an electric field', *Proceedings of the Royal Society of London A: Mathematical, Physical and Engineering Sciences*, vol. 280, pp. 211–226.

[109] Taylor G. (1966) 'Studies in electrohydrodynamics. i. the circulation produced in a drop by electrical field', *Proceedings of the Royal Society of London A: Mathematical, Physical and Engineering Sciences*, vol. 291, pp. 159–166.

[110] Ajayi O. (1978) 'A note on taylor's electrohydrodynamic theory', *Proceedings of the Royal Society of London A: Mathematical, Physical and Engineering Sciences*, vol. 364, pp. 499–507.

[111] Allan R. and Mason S. (1962) 'Particle behaviour in shear and electric fields. i. deformation and burst of fluid drops', *Proceedings of the Royal Society of London A: Mathematical, Physical and Engineering Sciences*, vol. 267, pp. 45–61.

[112] Tsukada T., Katayama T., Ito Y., and Hozawa M. (1993) 'Theoretical and experimental studies of circulations inside and outside a deformed drop under a uniform electric field.', *Journal of Chemical Engineering of Japan*, vol. 26, pp. 698–703.

[113] Feng J.Q. and Scott T.C. (1996) 'A computational analysis of electrohydrodynamics of a leaky dielectric drop in an electric field', *Journal of Fluid Mechanics*, vol. 311, pp. 289–326.

[114] Baygents J., Rivette N., and Stone H. (1998) 'Electrohydrodynamic deformation and interaction of drop pairs', *Journal of Fluid Mechanics*, vol. 368, pp. 359–375.

[115] Berry J., Davidson M., and Harvie D. (2013) 'A multiphase electrokinetic flow model for electrolytes with liquid/liquid interfaces', *Journal of Computational Physics*, vol. 251, pp. 209 – 222.

[116] Fernndez A., Tryggvason G., Che J., and Ceccio S.L. (2005) 'The effects of electrostatic forces on the distribution of drops in a channel flow: Two-dimensional oblate drops', *Physics of Fluids*, vol. 17, 093302.

[117] Fernndez A. (2008) 'Response of an emulsion of leaky dielectric drops immersed in a simple shear flow: Drops more conductive than the suspending fluid', *Physics of Fluids*, vol. 20, 043303.

[118] Hua J., Lim L.K., and Wang C.H. (2008) 'Numerical simulation of deformation/motion of a drop suspended in viscous liquids under influence of steady electric fields', *Physics of Fluids*, vol. 20, p. 113302.

[119] Zhang J. and Kwok D.Y. (2005) 'A 2d lattice boltzmann study on electrohydrodynamic drop deformation with the leaky dielectric theory', *Journal of Computational Physics*, vol. 206, pp. 150–161.

[120] Timung S., Chaudhuri J., Borthakur M.P., Mandal T.K., Biswas G., and Bandyopadhyay D. (2017) 'Electric field mediated spraying of miniaturized droplets inside microchannel', *Electrophoresis*, vol. 38, pp. 1450–1457.

[121] Borthakur M.P., Biswas G., and Bandyopadhyay D. (2018) 'Dynamics of deformation and pinch-off of a migrating compound droplet in a tube', *Physical Review E*, vol. 97, p. 043112.

[122] Burcham C. and Saville D. (2000) 'The electrohydrodynamic stability of a liquid bridge: microgravity experiments on a bridge suspended in a dielectric gas', *Journal of Fluid Mechanics*, vol. 405, pp. 37–56.

[123] Karimi A., Yazdi S., and Ardekani A. (2013) 'Hydrodynamic mechanisms of cell and particle trapping in microfluidics', *Biomicrofluidics*, vol. 7, p. 021501.

[124] Shapira M. and Haber S. (1990) 'Low reynolds number motion of a droplet in shear flow including wall effects', *International Journal of Multiphase Flow*, vol. 16, pp. 305 – 321.

[125] Taylor G.I. (1932) 'The viscosity of a fluid containing small drops of another fluid', *Proceedings of the Royal Society of London A: Mathematical, Physical and Engineering Sciences*, vol. 138, pp. 41–48.

[126] Taylor G.I. (1934) 'The formation of emulsions in definable fields of flow', *Proceedings of the Royal Society of London A: Mathematical, Physical and Engineering Sciences*, vol. 146, pp. 501–523.

[127] Torza S., Cox R., and Mason S. (1972) 'Particle motions in sheared suspensions xxvii. transient and steady deformation and burst of liquid drops', *Journal of Colloid and Interface Science*, vol. 38, pp. 395 – 411.

[128] Elmendorp J., *Dispersive mixing in liquid systems*, chap. 2 (John Wiley & Sons, 1991), pp. 17–100.

[129] Sheth K.S. and Pozrikidis C. (1995) 'Effects of inertia on the deformation of liquid drops in simple shear flow', *Computers & Fluids*, vol. 24, pp. 101–119.

[130] Li J., Renardy Y.Y., and Renardy M. (2000) 'Numerical simulation of breakup of a viscous drop in simple shear flow through a volume-of-fluid method', *Physics of Fluids*, vol. 12, pp. 269–282.

[131] Renardy Y. (2007) 'The effects of confinement and inertia on the production of droplets', *Rheologica Acta*, vol. 46, pp. 521–529.

[132] Renardy Y.Y. and Cristini V. (2001) 'Scalings for fragments produced from drop breakup in shear flow with inertia', *Physics of Fluids*, vol. 13, pp. 2161–2164.

[133] Lee J. and Pozrikidis C. (2006) 'Effect of surfactants on the deformation of drops and bubbles in navier–stokes flow', *Computers & Fluids*, vol. 35, pp. 43–60.

[134] Wagner A., Wilson L., and Cates M. (2003) 'Role of inertia in two-dimensional deformation and breakdown of a droplet', *Physical Review E*, vol. 68, p. 045301.

[135] Rumscheidt F.D. and Mason S. (1961) 'Particle motions in sheared suspensions xii. deformation and burst of fluid drops in shear and hyperbolic flow', *Journal of Colloid and Interface Science*, vol. 16, pp. 238–261.

[136] Kennedy M., Pozrikidis C., and Skalak R. (1994) 'Motion and deformation of liquid drops, and the rheology of dilute emulsions in simple shear flow', *Computers & Fluids*, vol. 23, pp. 251–278.

[137] Stone H.A. (1994) 'Dynamics of drop deformation and breakup in viscous fluids', *Annual Review of Fluid Mechanics*, vol. 26, pp. 65–102.

[138] Li X., Charles R., and Pozrikidis C. (1996) 'Simple shear flow of suspensions of liquid drops', *Journal of Fluid Mechanics*, vol. 320, pp. 395–416.

[139] Li X., Zhou H., and Pozrikidis C. (1995) 'A numerical study of the shearing motion of emulsions and foams', *Journal of Fluid Mechanics*, vol. 286, pp. 379–404.

[140] Nath B., Biswas G., Dalal A., and Sahu K.C. (2018) 'Cross-stream migration of drops suspended in poiseuille flow in the presence of an electric field', *Physical Review E*, vol. 97, p. 063106.

[141] Feng J.Q. (1999) 'Electrohydrodynamic behaviour of a drop subjected to a steady uniform electric field at finite electric reynolds number', *Proceedings of the Royal Society of London A: Mathematical, Physical and Engineering Sciences*, vol. 455, pp. 2245–2269.

[142] Collins R.T., Jones J.J., Harris M.T., and Basaran O.A. (2008) 'Electrohydrodynamic tip streaming and emission of charged drops from liquid cones', *Nature Physics*, vol. 4, p. 149.

[143] Ozen O., Aubry N., Papageorgiou D., and Petropoulos P. (2006) 'Monodisperse drop formation in square microchannels', *Physical Review Letters*, vol. 96, p. 144501.

[144] Saville D. (1997) 'Electrohydrodynamics: the taylor-melcher leaky dielectric model', *Annual Review of Fluid Mechanics*, vol. 29, pp. 27–64.

[145] Tomar G., Gerlach D., Biswas G., Alleborn N., Sharma A., Durst F., Welch S., and Delgado A. (2007) 'Two-phase electrohydrodynamic simulations using a volume-of-fluid approach', *Journal of Computational Physics*, vol. 227, pp. 1267 – 1285.

[146] Nath B., Biswas G., Dalal A., and Sahu K.C. (2017) 'Migration of a droplet in a cylindrical tube in the creeping flow regime', *Physical Review E*, vol. 95, p. 033110.

[147] Borthakur M.P., Biswas G., and Bandyopadhyay D. (2017) 'Formation of liquid drops at an orifice and dynamics of pinch-off in liquid jets', *Physical Review E*, vol. 96, p. 013115.

[148] Begg C.B. and Schrag D. (2002) 'Attribution of deaths following cancer treatment', *Journal of the National Cancer Institute*, vol. 94, p. 10441045.

[149] Williams S.C. (2013) 'Circulating tumor cells', *Proceedings of the National Academy of Sciences*, vol. 110, pp. 4861–4861.

[150] Paterlini-Brechot P. and Benali N.L. (2007) 'Circulating tumor cells (ctc) detection: clinical impact and future directions', *Cancer Letters*, vol. 253, pp. 180–204.

[151] Krebs M.G., Metcalf R.L., Carter L., Brady G., Blackhall F.H., and Dive C. (2014) 'Molecular analysis of circulating tumour cells [mdash] biology and biomarkers', *Nature Reviews Clinical Oncology*, vol. 11, pp. 129–144.

[152] Yu M., Stott S., Toner M., Maheswaran S., and Haber D.A. (2011) 'Circulating tumor cells: approaches to isolation and characterization', *The Journal of Cell Biology*, vol. 192, pp. 373–382.

[153] Aceto N., Bardia A., Miyamoto D.T., Donaldson M.C., Wittner B.S., Spencer J.A., Yu M., Pely A., Engstrom A., Zhu H., et al. (2014) 'Circulating tumor cell clusters are oligoclonal precursors of breast cancer metastasis', *Cell*, vol. 158, pp. 1110–1122.

[154] Hong B. and Zu Y. (2013) 'Detecting circulating tumor cells: current challenges and new trends', *Theranostics*, vol. 3, p. 377.

[155] Hou J.M., Krebs M., Ward T., Sloane R., Priest L., Hughes A., Clack G., Ranson M., Blackhall F., and Dive C. (2011) 'Circulating tumor cells as a window on metastasis biology in lung cancer', *The American Journal of Pathology*, vol. 178, pp. 989–996.

[156] Hou J.M., Krebs M.G., Lancashire L., Sloane R., Backen A., Swain R.K., Priest L., Greystoke A., Zhou C., Morris K., et al. (2012) 'Clinical significance and molecular characteristics of circulating tumor cells and circulating tumor microemboli in patients with small-cell lung cancer', *Journal of Clinical Oncology*, vol. 30, pp. 525–532.

[157] Yu M., Bardia A., Wittner B.S., Stott S.L., Smas M.E., Ting D.T., Isakoff S.J., Ciciliano J.C., Wells M.N., Shah A.M., et al. (2013) 'Circulating breast tumor cells exhibit dynamic changes in epithelial and mesenchymal composition', *Science*, vol. 339, pp. 580–584.

[158] Molnar B., Ladanyi A., Tanko L., Sréter L., and Tulassay Z. (2001) 'Circulating tumor cell clusters in the peripheral blood of colorectal cancer patients', *Clinical Cancer Research*, vol. 7, pp. 4080–4085.

[159] Cho E.H., Wendel M., Luttgen M., Yoshioka C., Marrinucci D., Lazar D., Schram E., Nieva J., Bazhenova L., Morgan A., et al. (2012) 'Characterization of circulating tumor cell aggregates identified in patients with epithelial tumors', *Physical Biology*, vol. 9, p. 016001.

[160] Fidler I.J. (1973) 'The relationship of embolic homogeneity, number, size and viability to the incidence of experimental metastasis', *European Journal of Cancer (1965)*, vol. 9, pp. 223–227.

[161] Fidler I.J. (1978) 'Tumor heterogeneity and the biology of cancer invasion and metastasis', *Cancer Research*, vol. 38, pp. 2651–2660.

[162] Liotta L.A., Kleinerman J., and Saldel G.M. (1976) 'The significance of hematogenous tumor cell clumps in the metastatic process', *Cancer Research*, vol. 36, pp. 889–894.

[163] Lee G.Y. and Lim C.T. (2007) 'Biomechanics approaches to studying human diseases', *Trends in Biotechnology*, vol. 25, pp. 111–118.

[164] Friedl P., Wolf K., and Lammerding J. (2011) 'Nuclear mechanics during cell migration', *Current Opinion in Cell Biology*, vol. 23, pp. 55–64.

[165] Yamauchi K., Yang M., Jiang P., Yamamoto N., Xu M., Amoh Y., Tsuji K., Bouvet M., Tsuchiya H., Tomita K., et al. (2005) 'Real-time in vivo dual-color imaging of intracapillary cancer cell and nucleus deformation and migration', *Cancer Research*, vol. 65, pp. 4246–4252.

[166] Zheng Y. and Sun Y. (2011) 'Microfluidic devices for mechanical characterisation of single cells in suspension', *Micro & Nano Letters*, vol. 6, pp. 327–331.

[167] Shelby J.P., White J., Ganesan K., Rathod P.K., and Chiu D.T. (2003) 'A microfluidic model for single-cell capillary obstruction by plasmodium falciparum-infected erythrocytes', *Proceedings of the National Academy of Sciences*, vol. 100, pp. 14618–14622.

[168] Abkarian M., Faivre M., and Stone H.A. (2006) 'High-speed microfluidic differential manometer for cellular-scale hydrodynamics', *Proceedings of the National Academy of Sciences*, vol. 103, pp. 538–542.

[169] Gifford S.C., Derganc J., Shevkoplyas S.S., Yoshida T., and Bitensky M.W. (2006) 'A detailed study of time-dependent changes in human red blood cells: from reticulocyte maturation to erythrocyte senescence', *British Journal of Haematology*, vol. 135, pp. 395–404.

[170] Lee W.G., Bang H., Yun H., Lee J., Park J., Kim J.K., Chung S., Cho K., Chung C., Han D.C., et al. (2007) 'On-chip erythrocyte deformability test under optical pressure', *Lab on a Chip*, vol. 7, pp. 516–519.

[171] Herricks T., Antia M., and Rathod P.K. (2009) 'Deformability limits of plasmodium falciparum-infected red blood cells', *Cellular Microbiology*, vol. 11, pp. 1340–1353.

[172] Rosenbluth M.J., Lam W.A., and Fletcher D.A. (2008) 'Analyzing cell mechanics in hematologic diseases with microfluidic biophysical flow cytometry', *Lab on a Chip*, vol. 8, pp. 1062–1070.

[173] Gabriele S., Benoliel A.M., Bongrand P., and Théodoly O. (2009) 'Microfluidic investigation reveals distinct roles for actin cytoskeleton and myosin ii activity in capillary leukocyte trafficking', *Biophysical Journal*, vol. 96, pp. 4308–4318.

[174] Gabriele S., Versaevel M., Preira P., and Théodoly O. (2010) 'A simple microfluidic method to select, isolate, and manipulate single-cells in mechanical and biochemical assays', *Lab on a Chip*, vol. 10, pp. 1459–1467.

[175] Raj A., Dixit M., Doble M., and Sen A. (2017) 'A combined experimental and theoretical approach towards mechanophenotyping of biological cells using a constricted microchannel', *Lab on a Chip*, vol. 17, pp. 3704–3716.

[176] Hou H.W., Li Q., Lee G., Kumar A., Ong C., and Lim C.T. (2009) 'Deformability study of breast cancer cells using microfluidics', *Biomedical Microdevices*, vol. 11, pp. 557–564.

[177] Au S.H., Storey B.D., Moore J.C., Tang Q., Chen Y.L., Javaid S., Sarioglu A.F., Sullivan R., Madden M.W., OKeefe R., et al. (2016) 'Clusters of circu-

lating tumor cells traverse capillary-sized vessels', *Proceedings of the National Academy of Sciences*, vol. 113, pp. 4947–4952.

[178] Leong F.Y., Li Q., Lim C.T., and Chiam K.H. (2011) 'Modeling cell entry into a micro-channel', *Biomechanics and Modeling in Mechanobiology*, vol. 10, pp. 755–766.

[179] Elshimali Y.I. and Grody W.W. (2006) 'The clinical significance of circulating tumor cells in the peripheral blood', *Diagnostic Molecular Pathology*, vol. 15, pp. 187–194.

[180] Park S., Ang R.R., Duffy S.P., Bazov J., Chi K.N., Black P.C., and Ma H. (2014) 'Morphological differences between circulating tumor cells from prostate cancer patients and cultured prostate cancer cells', *PLOS One*, vol. 9, p. e85264.

[181] Li P., Mao Z., Peng Z., Zhou L., Chen Y., Huang P.H., Truica C.I., Drabick J.J., El-Deiry W.S., Dao M., et al. (2015) 'Acoustic separation of circulating tumor cells', *Proceedings of the National Academy of Sciences*, vol. 112, pp. 4970–4975.

[182] Weiss L. (1987) 'The hemodynamic destruction of circulating cancer cells', *Biorheology*, vol. 24, pp. 105–115.

[183] Sato H., Takino T., Okada Y., Cao J., Shinagawa A., Yamamoto E., and Seiki M. (1994) 'A matrix metalloproteinase expressed on the surface of invasive tumour cells', *Nature*, vol. 370, p. 61.

[184] Roomi M., Monterrey J., Kalinovsky T., Rath M., and Niedzwiecki A. (2010) 'In vitro modulation of mmp-2 and mmp-9 in human cervical and ovarian cancer cell lines by cytokines, inducers and inhibitors', *Oncology Reports*, vol. 23, pp. 605–614.

Appendix

Derivation of electric body force term

The Maxwell's equations can be written as,

$$\nabla \cdot \mathbf{E} = \frac{q_v}{\epsilon_0}, \tag{A.1}$$

$$\nabla \cdot \mathbf{B} = 0, \tag{A.2}$$

$$\nabla \times \mathbf{E} = -\frac{\partial \mathbf{B}}{\partial t}, \tag{A.3}$$

$$\nabla \times \mathbf{B} = \mu_0 \mathbf{J} + \mu_0 \epsilon_0 \frac{\partial E}{\partial t}, \tag{A.4}$$

where, $\mathbf{E}$ represents the electric field, q_v is the volumetric charge density, $\mathbf{B}$ denotes the magnetic flux density and $\mathbf{J}$ denotes the density of free current.

In the presence of both electric field and magnetic field, the net force on a charge Q moving with velocity $\mathbf{v}$ is given by,

$$\mathbf{F} = Q[\mathbf{E} + (\mathbf{v} \times \mathbf{B})]. \tag{A.5}$$

The total electromagnetic force on the charges inside a volume V is,

$$\mathbf{F}_t = \int_V [\mathbf{E} + (\mathbf{v} \times \mathbf{B})] q_v d\forall, \tag{A.6}$$

$$\mathbf{F}_t = \int_V [q_v \mathbf{E} + (\mathbf{J} \times \mathbf{B})] d\forall, \tag{A.7}$$

where, the current density is given as, $\mathbf{J} = q_v \mathbf{v}$. Thus, the force per unit volume is given by,

$$\mathbf{f}_e = q_v \mathbf{E} + (\mathbf{J} \times \mathbf{B}). \tag{A.8}$$

Substituting Eq. A.1 in Eq. A.8, we get

$$\mathbf{f}_e = \epsilon_0 (\nabla \cdot \mathbf{E}) \mathbf{E} + (\mathbf{J} \times \mathbf{B}). \tag{A.9}$$

Substituting Eq. A.4 in Eq. A.9, we get

$$\mathbf{f}_e = \epsilon_0 (\nabla \cdot \mathbf{E}) \mathbf{E} + \left[\frac{\nabla \times \mathbf{B}}{\mu_0} - \epsilon_0 \frac{\partial \mathbf{E}}{\partial t} \right] \times \mathbf{B}. \tag{A.10}$$

Now,

$$\frac{\partial}{\partial t}(\mathbf{E}\times\mathbf{B}) = \frac{\partial \mathbf{E}}{\partial t}\times\mathbf{B} + \mathbf{E}\times\frac{\partial \mathbf{B}}{\partial t}. \tag{A.11}$$

Substituting Eq. A.3 in Eq. A.11,

$$\frac{\partial}{\partial t}(\mathbf{E}\times\mathbf{B}) = \frac{\partial \mathbf{E}}{\partial t}\times\mathbf{B} - \mathbf{E}\times(\nabla\times\mathbf{E}). \tag{A.12}$$

Thus,

$$\frac{\partial \mathbf{E}}{\partial t}\times\mathbf{B} = \frac{\partial}{\partial t}(\mathbf{E}\times\mathbf{B}) + \mathbf{E}\times(\nabla\times\mathbf{E}). \tag{A.13}$$

Substituting Eq. A.13 in Eq. A.10,

$$\mathbf{f}_e = \epsilon_0(\nabla\cdot\mathbf{E})\mathbf{E} + \frac{\nabla\times\mathbf{B}}{\mu_0}\times\mathbf{B} - \epsilon_0\frac{\partial \mathbf{E}}{\partial t}\times\mathbf{B}. \tag{A.14}$$

Substituting Eq. A.13 in Eq. A.14,

$$\mathbf{f}_e = \epsilon_0(\nabla\cdot\mathbf{E})\mathbf{E} + \frac{\nabla\times\mathbf{B}}{\mu_0}\times\mathbf{B} - \epsilon_0\left[\frac{\partial}{\partial t}(\mathbf{E}\times\mathbf{B}) + \mathbf{E}\times(\nabla\times\mathbf{E})\right], \tag{A.15}$$

$$\mathbf{f}_e = \epsilon_0\left[(\nabla\cdot\mathbf{E})\mathbf{E} - \mathbf{E}\times(\nabla\times\mathbf{E})\right] - \frac{1}{\mu_0}\left[\mathbf{B}\times(\nabla\times\mathbf{B})\right] - \epsilon_0\frac{\partial}{\partial t}(\mathbf{E}\times\mathbf{B}). \tag{A.16}$$

Since, $\nabla\cdot\mathbf{B} = 0$, so we insert $(\nabla\cdot\mathbf{B})\mathbf{B}$ in Eq. A.16 to simplify.
We know,

$$\nabla(E^2) = 2(\mathbf{E}\cdot\nabla)\mathbf{E} + 2\mathbf{E}\times(\nabla\times\mathbf{E}), \tag{A.17}$$

$$\mathbf{E}\times(\nabla\times\mathbf{E}) = \frac{1}{2}\nabla(E^2) - (\mathbf{E}\cdot\nabla)\mathbf{E}. \tag{A.18}$$

Similarly,

$$\mathbf{B}\times(\nabla\times\mathbf{B}) = \frac{1}{2}\nabla(B^2) - (\mathbf{B}\cdot\nabla)\mathbf{B}. \tag{A.19}$$

Thus,

$$\mathbf{f}_e = \epsilon_0\left[(\nabla\cdot\mathbf{E})\mathbf{E} + (\mathbf{E}\cdot\nabla)\mathbf{E} - \frac{1}{2}\nabla(E^2)\right] + \frac{1}{\mu_0}\left[(\nabla\cdot\mathbf{B})\mathbf{B} + (\mathbf{B}\cdot\nabla)\mathbf{B} - \frac{1}{2}\nabla(B^2)\right] - \epsilon_0\frac{\partial}{\partial t}(\mathbf{E}\times\mathbf{B}). \tag{A.20}$$

$$\mathbf{f}_e = \epsilon_0\left[(\nabla\cdot\mathbf{E})\mathbf{E} + (\mathbf{E}\cdot\nabla)\mathbf{E}\right] + \frac{1}{\mu_0}\left[(\nabla\cdot\mathbf{B})\mathbf{B} + (\mathbf{B}\cdot\nabla)\mathbf{B}\right] - \frac{1}{2}\nabla\left(\epsilon_0 E^2 + \frac{1}{\mu_0}B^2\right) - \epsilon_0\frac{\partial}{\partial t}(\mathbf{E}\times\mathbf{B}). \tag{A.21}$$

The above Eq. A.21 can be simplified by introducing the Maxwell stress tensor $\mathbf{M}$ and Poynting vector $\mathbf{S}$.

$$\mathbf{f}_e = \nabla \cdot \mathbf{M} - \epsilon_0 \mu_0 \frac{\partial \mathbf{S}}{\partial t}, \tag{A.22}$$

where, $\mathbf{M}$=$\epsilon_0 \left[\mathbf{E} \otimes \mathbf{E} - \frac{1}{2}E^2\mathbf{I}\right] + \frac{1}{\mu_0}\left[\mathbf{B} \otimes \mathbf{B} - \frac{1}{2}B^2\mathbf{I}\right]$ and $\mathbf{S} = \frac{1}{\mu_0}(\mathbf{E} \times \mathbf{B})$. In the absence of magnetic field, the terms containing $\mathbf{B}$ can be neglected. Hence, the final form of the electric force terms reduces to,

$$\mathbf{f}_e = \nabla \cdot \mathbf{M} = \nabla \cdot \left[\epsilon_0 \left(\mathbf{E} \otimes \mathbf{E} - \frac{1}{2}E^2\mathbf{I}\right)\right]. \tag{A.23}$$

List of publications

Journal publications

1. **B. Nath**, G. Biswas, A. Dalal, and K. C. Sahu, Migration of a droplet in a cylindrical tube in the creeping flow regime, ***Physical Review E*** 95, 033110, 2017.

2. **B. Nath**, G. Biswas, A. Dalal, and K. C. Sahu, Cross stream migration of drops suspended in Poiseuille flow in the presence of an electric field, ***Physical Review E*** 97, 063106, 2018.

3. **B. Nath**, A. Raza, V. Sethi, A. Dalal, S.S. Ghosh and G. Biswas, Understanding flow dynamics, viability and metastatic potency of cervical cancer (HeLa) cells through constricted microchannel, ***Scientific Reports*** 8, 17537, 2018.

4. **B. Nath**, G. Biswas and A. Dalal, Influence of electric field on deformation of a drop in shear flow, ***Physics of Fluids*** 31, 042102, 2019.

Conference publications

1. **B. Nath**, M. P. Borthakur, G. Biswas and A. Dalal, Dynamics of droplet deformation in microchannels with symmetric and asymmetric constrictions, *International Mechanical Engineering Congress and Exposition(ASME - IMECE)*, Tampa, Florida, 3rd - 9th November, 2017.

2. **B. Nath**, M. P. Borthakur, G. Biswas and A. Dalal, Deformation of a droplet in constricted microfluidic channels at low Reynolds number, *The Asian Symposium on Computational Heat Transfer and Fluid Flow (ASCHT)*, IIT Madras, 10th - 13th December, 2017.

3. **B. Nath**, M. P. Borthakur, G. Biswas and A. Dalal, Influence of electric field in the lateral migration of a drop inside a microchannel, *International Conference on Recent Innovations and Developments in Mechanical Engineering (IC-RIDME)* , NIT Meghalaya, Shillong, 8th - 10th November, 2018.